



INNOVATIVE DEVELOPMENTS
in
**GaN-BASED
TECHNOLOGY**

PROFESSOR DR. ZAINURIAH
HASSAN FASc
Universiti Sains Malaysia

FELLOWS' LECTURE



In Pursuit Of Excellence In Science

Innovative Development in GaN-Based Technology

© Academy of Sciences Malaysia 2017

All Rights Reserved.

No part of this publication may be reproduced, stored in a retrieval system, or transmitted in any form or by any means, electronic, mechanical, photocopying, recording or otherwise without prior permission in writing from the Academy of Sciences Malaysia.

Academy of Sciences Malaysia
Level 20, West Wing, MATRADE Tower
Jalan Sultan Haji Ahmad Shah off Jalan Tuanku Abdul Halim
50480 Kuala Lumpur, Malaysia

e-ISBN 978-983-2915-41-6

BIODATA



Professor Dr Zainuriah Hassan FASc

Institute of Nano Optoelectronics Research and Technology (INOR)

Universiti Sains Malaysia

Professor Dr Zainuriah Hassan is an expert in the area of wide band gap semiconductors and devices. She received the B.Sc (Magna Cum Laude) degree and the Masters degree in Physics from Western Michigan University, USA in 1983 and 1985, respectively, and the Ph.D degree in Experimental Condensed Matter Physics from Ohio University, USA in 1998. She was a Research Associate at Ohio University from 1997 to 1998, and a Visiting Research Scholar under the Fulbright Program at Department of Electrical and Computer Engineering, University of Minnesota, USA in 2004/2005.

At present, Professor Dr. Zainuriah Hassan is attached to the Institute of Nano Optoelectronics Research and Technology (INOR), at Universiti Sains Malaysia, and formerly the Director of the Centre for Research Initiatives in Natural Sciences (2013-2015), Dean (2010-2012), Deputy Dean - Academic and Student Development (2009-2010), and Chair of the Engineering Physics Program (2007-2009) at School of Physics, Universiti Sains Malaysia.

Her focus of research is on all aspects related to materials growth, characterization, and fabrication of optoelectronic and electronic devices such as LEDs and sensors based on III-nitrides (GaN, InN, AlN, and related nitride alloys) and also other wide band gap semiconductors such as ZnO, CdS, TiO₂, CdO and other metal oxides. She is also working on organic materials for light emitting device applications. She has published more than 670 papers in international and national journals and proceedings, and supervised more than 70 PhD and MSc students.

Professor Dr. Zainuriah Hassan has received several national and international awards and scholarships, and served as reviewer, editor, jury, and member of various evaluation panels. She also served on various committees, providing services for the community and country, and was a member of the Ibn Al-Haytham International Working Group for the International Year of Light IYL 2015 (under UNESCO). She is currently a Fellow of Academy of Sciences Malaysia, and a member of the Materials Research Society, Optical Society of America, IEEE, Fulbright Association, Malaysian Solid State Science and Technology Society, Malaysian Institute of Physics, and National Council of Professor.

PREFACE

The III-nitrides semiconductors, specifically the GaN-based materials, including the binary GaN and related alloys with InN and AlN, such as the ternary AlGaN and InGaN as well as the quaternary InAlGaN, have been intensively investigated in recent years because of the potential applications for optoelectronic devices operating in short wavelength spectral range and in high power and high temperature electronic devices. The GaN-based materials offer a wide range of direct band gap, spanning from 0.7 eV for InN, to 6.2 eV for AlN with 3.4 eV for GaN. This energy range is suitable for band-to-band light generation with colors ranging from infrared to ultraviolet wavelengths.

GaN-based materials are also ideal for the fabrication of high responsive and visible blind UV detectors because of the unique properties, that encompass wide and direct band gap, high absorption coefficients, and sharp cutoff of the wavelength detection. The high breakdown voltage and high saturation velocity also enable the use of GaN-based materials for high speed device operation and high power applications, such as power amplifiers for wireless base stations, low noise amplifiers, and high power switches. Sensing devices are another important application of the GaN-based materials, especially in harsh environments owing to the high thermal and chemical stability of these materials.

The ability of the band gap to be tuned from the infrared to ultraviolet emission wavelength region has also created a greater breakthrough in the GaN-based technology by employing the nitrides materials for light emitting diodes applications, either in the form of pn-homojunction or heterojunction. Phosphor converted light emitting diodes will be another significant subject in the advancement of GaN-based technology for white light emission, in which the blue or

ultraviolet emission from the light emitting diodes can be converted to white emission via a phosphor material.

This monograph presents an overview of innovative developments in GaN-based technology. It covers the pioneer work on amorphous and microcrystalline GaN films grown on various substrates using the electron cyclotron resonance plasma-assisted metal-organic chemical vapor deposition (ECR-MOCVD) technique, as well as epitaxial growth of III-nitrides films using MOCVD and plasma assisted molecular beam epitaxy (PAMBE). PAMBE growth has enabled high quality thin films to be analyzed and characterized for the study on fundamental properties of these materials. Recent research activities which focused on the growth of nanostructures, such as GaN nanowires and InGaN quantum dots are also covered.

Due to the increasing demand for using nanostructured III-nitrides films that offer high surface area to volume ratio as well as the emergence of issues pertaining to additional stress build-up and defect density at the interface of the III-nitrides films grown on foreign substrates owing to a lattice mismatch issue, different novel etching techniques (metal-assisted UV electroless etching, photoelectrochemical etching, and laser-induced etching) have been employed to produce porous structures in the binary, ternary, and quaternary III-nitrides films. Properties and device applications of all of these materials are presented. A brief discussion is given on the various optoelectronic and electronic devices that have been fabricated and characterized, which include photodetectors, solar cell, sensors, capacitor, and light emitting diodes. Light emitting heterojunction structures incorporating other wide band gap semiconductors such as ZnO grown on GaN using novel techniques are also covered. Both experimental and theoretical works have been implemented to deliver a better understanding towards the changes in performance of the devices with respect to processing parameters.

ACKNOWLEDGEMENT

Research funding from IRPA RMK-8 Strategic Research Grant, RU Top Down, RUI, FRGS, ERGS, ScienceFund, Fulbright, AUN/SEEDNet, ONR/BMDO, NSF/ECS, NASA/JPL, CIES, IIE, Universiti Sains Malaysia, University of Minnesota, and Ohio University are gratefully acknowledged. Not forgetting also my sincere appreciation to my previous and current students, Dr. Yam Fong Kwong, Dr. Ng Sha Shiong, Dr. Chuah Lee Siang, Dr. Norzaini Zainal, Dr. Naser Mahmoud Ahmed, Dr. Jalal Jabbar Hassan, Dr. Asmiet Ramizy, Dr. Ghasem Alahyarizadeh, Dr. Asaad Shakir Hussein, Dr. Hind I AbdulGafour, Dr. Maryam Amirhoseiny, Dr. Alaa Jabbar Ghazai, Dr. Azita Zandi Goharrizi, Dr. Ahmad Hadi Ali, Dr. Saleh Hasson Abud Al-Amery, Dr. Beh Khi Poay, Dr. Qahtan Nofan Abdullah, Dr. Mohd Zaki Mohd Yusoff, Ainorkhilah Mahmood, Rosfariza Radzali, Lee Yan Cheung, Khairul Azwan Abdullah, Sabah M. Mohammad, Husnen R. Abd, and all other PhD and MSc students under my supervision. My heartiest gratitude is presented to my post-doctoral fellows, Dr. Lim Way Foong and Dr. Quah Hock Jin as well as my research officer, Mr. Chin Che Woei for their continuous support and contribution for the completion of this monograph. Last but not least, I would also like to extend my appreciation to all staff from Institute of Nano Optoelectronics Research and Technology (INOR) and School of Physics, Universiti Sains Malaysia for their cooperation in this research work.

Innovative Developments in GaN-based Technology

1. Introduction

Since years, the III-nitrides semiconductors, spanning from the binary GaN to the ternary (AlGa_N, InGa_N) and quaternary (InAlGa_N) alloys, have left remarkable footprints in the applications of light emitting diodes (LEDs) and power electronics, owing to the direct wide band gap, hardness as well as high thermal and chemical stability provided by the GaN-based materials. These characteristics have inevitably shed some lights over the other semiconductors materials, such as silicon (Si) and silicon carbide (SiC), and thus pushing the GaN-based materials to the forefront of technology for optoelectronic and electronic applications. The ability of tuning the wide band gap of GaN-based materials from 0.7 eV (InN) to 3.4 eV (GaN), and to 6.2 eV (AlN) to obtain the desired infrared to ultraviolet (UV) wavelength region [1] has become a stepping stone to achieving a greater breakthrough in the semiconductor technology by forming heterostructures for use in the fabrication of GaN-based devices for LEDs. Literatures have also divulged that the wide band gap of GaN-based materials has been the reason contributing to the acquisition of high breakdown field, high theoretical electron drift velocity, high saturation current density, and low intrinsic carrier concentration in the GaN-based devices [2].

Nonetheless, further development of the GaN-based devices has become stagnant due to a lack of high quality substrate for GaN epitaxial growth and a difficulty in obtaining high n-type and p-type doping in the GaN films. Keeping pace with an inspired study in the growth of good quality of epitaxial films by Yoshida in 1983 [3] and the first p-type GaN by Amano [4] in 1988, crystal-growth techniques have been widely practiced, aiming to grow high quality GaN-based materials. The first GaN-based field effect transistor (FET) was successfully reported by Khan

[5] in 1993 while the first GaN-based laser diode was reported by Nakamura [6]. In recent years, other growth techniques, including hydride vapor phase epitaxy (HVPE), metal organic vapor phase epitaxy (MOVPE), and molecular beam epitaxy (MBE) have been progressively employed to improve quality of the epitaxial films.

Following the development of III-nitrides semiconductors, particular interest has been devoted to growing amorphous GaN (a-GaN) in addition to the GaN epitaxy. It was reported that the growth of a-GaN surpasses that of the crystalline GaN in terms of offering a lower processing cost, a lower growth temperature, and a better suitability for deposition on various substrates. Furthermore, it has been suggested that the strong ionicity of the Ga-N bond and the lattice mismatch between the GaN layer and underlying substrate could be relieved by replacing the GaN epitaxy with a-GaN [7]. The first reactive sputtered a-GaN film was reported by Hariu [8] in 1978, followed by other experimental studies regarding reactive sputtered a-GaN, MBE grown a-GaN, ion assisted deposited a-GaN, and hydrogenated a-GaN. The experimental studies of a-GaN were also succeeded by theoretical studies, which have been performed by Stumm and Drabold [9] in 1997 and by Yu and Drabold [10] in 1998.

2. Amorphous and Microcrystalline III-Nitrides

Amorphous GaN (a-GaN) has attracted considerable interest to be used as an electronic material for its predictable band gap energy of 2.8 eV with no mid-gap states [9]. Kobayashi and his co-workers [11] as well as Stumm *et al.* [9] have also disclosed in previous studies that a-GaN and microcrystalline GaN both have promise as novel electronic materials, owing to the special attribute of these materials to be deposited inexpensively over large area at low temperatures [9, 11]. The advantages offered by a-GaN and microcrystalline GaN are

foreseeable to contribute a new impetus to the field of optoelectronic and electronic devices as well as widening the range of possible substrates that could be used, which would indirectly lead to a cost reduction in the film processing technology [9, 11]. Thus, whereas epitaxial GaN films have been the choice for short wavelength emitters and detectors, the development of low-temperature grown a-GaN and microcrystalline GaN could open up opportunities for large-area devices, such as LED arrays, UV detector arrays, and high temperature transistors at a relatively low cost [12].

Electron cyclotron resonance (ECR) plasma-assisted metal-organic chemical vapor deposition (MOCVD) has been used to deposit GaN thin films over a range of temperatures from 50°C to 650°C (Fig. 2.1) on silicon, sapphire, and quartz substrates using triethylgallium and molecular nitrogen or ammonia as the reagents [12].

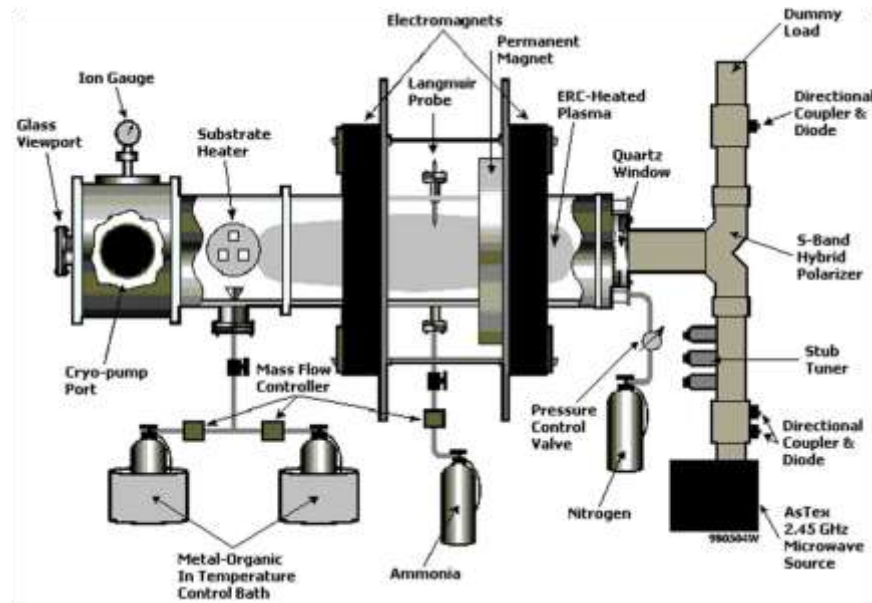


Fig. 2.1 ECR plasma-assisted MOCVD system (Spire Corporation, USA) [12].

Findings from the X-ray diffraction have revealed that a growth temperature at 200°C has led to the formation of a-Ga while higher temperatures (600°C) has brought to a transition

from amorphous to crystalline phase in the GaN film [12]. The formation of a-GaN/Si(111) isotype heterojunction in this work was thereafter characterized in term of current-voltage (I-V) characteristic ((Fig. 2.2 (i)) at room temperature. It was observed that rectification behavior has been demonstrated for the isotype heterojunction. Therefore, further investigation was carried out by analyzing Schottky behaviors of the heterojunction via forward bias I-V measurement using nickel (Ni) ((Fig. 2.2 (ii)(a)) and chromium (Cr) ((Fig. 2.2 (ii)(b)) as the Schottky contacts ((Fig. 2.2 (ii)). The calculated Schottky barrier height values were 0.62 and 0.64 eV, respectively for the Ni/a-GaN and Cr/a-GaN Schottky barriers. These results have inevitably contributed certain innovation for further exploration and development of low temperature grown GaN films for use in electronic and optoelectronic applications [12].

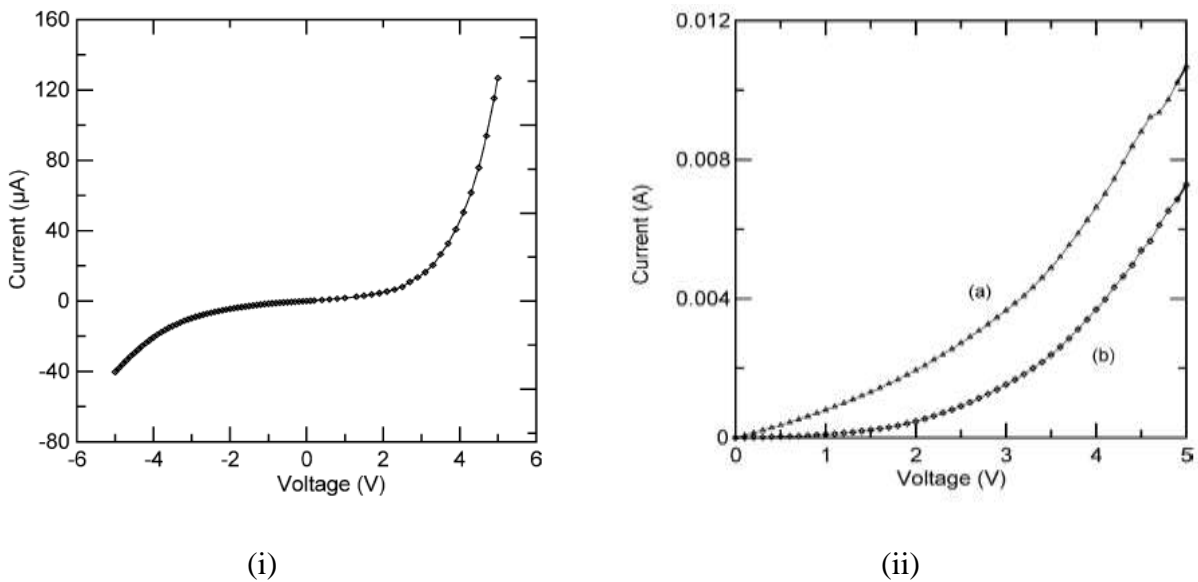


Fig. 2.2 (i) I-V characteristics for a-GaN/Si(111) isotype heterojunction grown at 200°C and (ii) Forward bias I-V characteristics of (a) Ni/a-GaN and (b) Cr/a-GaN Schottky barriers [12].

Besides a-GaN/Si(111) isotype heterojunction, the a-GaN film was also grown on p-type Si(111) substrate via ECR plasma-assisted MOCVD technique to form anisotype (n-p) heterojunction. I-V characterization for the a-GaN/p-Si(111) anisotype heterojunction [13]

grown at 400°C was performed in order to study its rectification behavior under solar illumination ((Fig. 2.3 (a)) as well as Schottky behavior for Ni/a-GaN/p-Si ((Fig. 2.3 (b)) [13]. It was deduced from Fig. 2.3 that both rectification characteristic and photovoltaic effect were observed for the a-GaN/p-Si anisotype heterojunction structure. The Schottky barrier height of Ni on a-GaN derived by the I-V method was 0.79 eV. This encouraging result was significant to be used as a reference for future exploration and development of a-GaN as a wide band gap transparent amorphous material for optoelectronic and electronic applications [13].

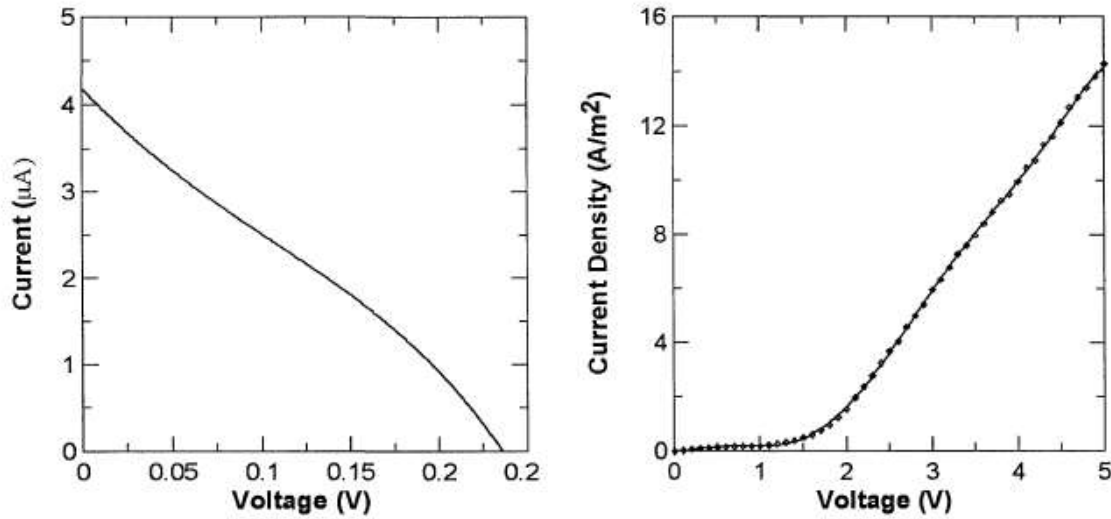


Fig. 2.3 (a) I-V characteristics for a-GaN/p-Si(111) anisotype (n-p) heterojunction grown at 400°C and related (b) forward bias I-V characteristics of Ni/a-GaN Schottky barrier [13].

Polarized infrared (IR) characteristics of GaN films grown on Si substrates using ECR plasma-assisted MOCVD and low pressure (LP) MOCVD at various temperatures (50, 170, 200, and 600°C) and 1000°C, respectively were also studied at room temperature [14-15]. Similar patterns were observed for the IR spectra of the GaN films grown at 200°C and below ((Figs. 2.4 (a) and 2.5 (b)) with no detection of IR reststrahlen band, suggesting the presence of disordered phases or short-range order in the films [16]. This finding confirmed that amorphous GaN films

have been formed, in agreement with the results from Refs. [13] and [17]. It could be observed that both s- (peak A) and p-polarization (peak B) spectra were obtained for GaN film grown at 1000°C, corresponding to transverse-optical (TO) phonon modes of GaN and AlN, respectively. Additional peak C was detected, ascribing to longitudinal-optical (LO) phonon mode of GaN [15]. For the GaN films grown at 600°C, a broad reststrahlen band was detected in both s- and p-polarization spectra) with a pronounced dip C (in p-polarization spectra). Besides that, the disappearance of the peak B in the spectra indicated that the sample was grown without any buffer layer. This work concluded that IR spectroscopic studies could be an effective non-destructive tool to determine the film structure and related optical properties [15], whereby the structure type of the GaN films was sensitive to the growth temperature and could be correlated to the variation of the IR reststrahlen band. It was also deduced that a good crystalline structure of GaN films would have a tendency to grow at temperature higher than 600°C [15].

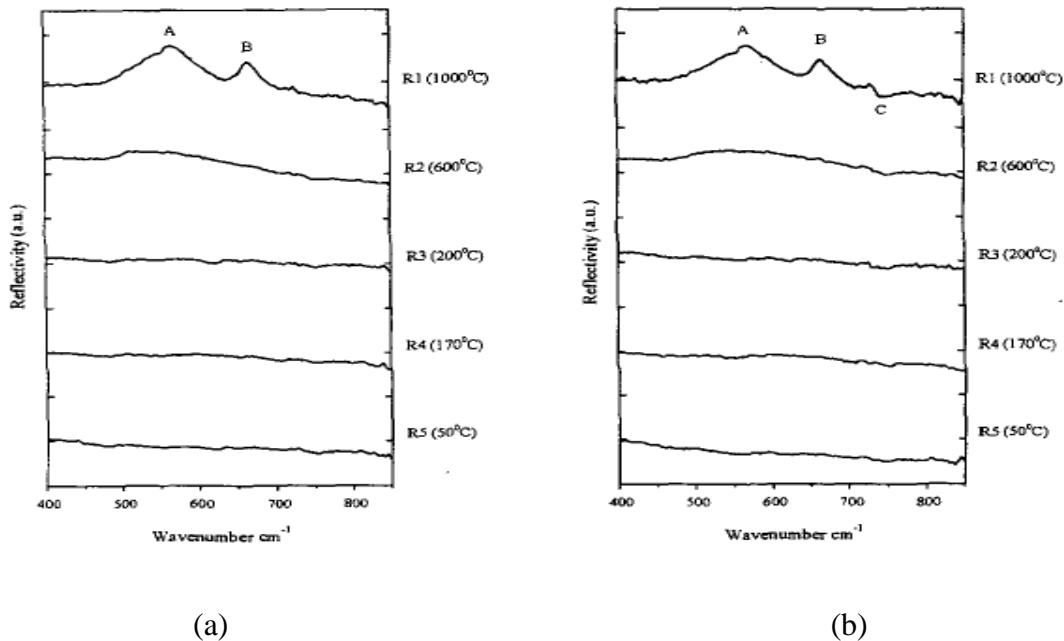


Fig. 2.4 (a) s-polarization and (b) p-polarization IR reflectance spectra of GaN/Si films at various growth temperatures [14-15].

3. Epitaxial III-Nitrides

Epitaxial growth techniques have been specifically developed to enable the growth of high quality semiconductor alloys under controlled conditions. Using these techniques, single-crystal semiconductor thin films can be synthesized on different substrates. Owing to the escalating demand for complex semiconductor devices, several techniques have been successfully developed and refined in order to satisfy the ever evolving needs. The oldest epitaxial growth technique, namely the liquid phase epitaxy, although is still being used in some instances, the poor thickness uniformity and control as well as poor interface formation has slowly switched to using the other technique, which is the vapor phase epitaxy. This vapor phase epitaxy technique has been gaining interest in growing the III-nitrides semiconductors though the formation of surface defects in the epitaxial films is unavoidable. The quality of the epitaxial films can be greatly improved with minimized formation of surface defects through the emergence of molecular beam epitaxy (MBE) and metal-organic chemical vapor deposition (MOCVD) techniques, which offer unsurpassed capabilities in the epitaxial growth of numerous semiconductor structures, in terms of material quality, process control, and reliability.

In general, the MBE epitaxial growth process involves a reaction of multiple thermal beams of atoms or molecules with a crystalline surface under ultra high vacuum (UHV) conditions. The UHV environment will allow collimated beams of highly purified source material to arrive at the substrate without colliding with other atoms or molecules, and thus minimizing contamination. The heated substrate surface will allow the arriving atoms to distribute themselves evenly across the surface, decreasing imperfections in the crystal structure. These conditions generally will give a better control of the growth through kinetics of surface

processes between the impinging beams and the substrate as compared to the other growth methods.

In comparison to the MOCVD growth technique, the MBE technique offers real-time diagnostic tools, such as reflection high-energy electron diffraction (RHEED), which can be used to extract growth information. Nevertheless, the relatively slow growth rates in the MBE process has restricted the use of this growth technique for large scale manufacturing, in which the process time has been a critical parameter for epitaxial growth. In this project, Veeco Gen II plasma-assisted MBE (PAMBE) was used to grow high quality III-nitrides films (Fig. 3.1) for detailed understanding of the growth mechanism lying behind. Though previous studies have been reporting about the research works done on epitaxy of GaN-based materials, majority of the works was primarily focused on device applications. It was hypothesized that the performance of the GaN-based materials was strongly dependent on the materials quality. Therefore, the aspect of growth mechanism ought to be understood in this project before further improvement on the materials quality could be comprehended.



Fig. 3.1 Plasma-assisted molecular beam epitaxy (PAMBE) system.

A representative flow chart showing the growth procedures involved in PAMBE system is presented in Fig. 3.2. A typical growth cycle consists of substrate introduction, outgassing, nitridation, gallium (Ga) cleaning, buffer layer deposition, and III-nitrides epilayer growth. After loading of the substrate to the growth chamber, outgassing or heating was performed to remove any surface contaminants. The nitridation step was only applied to sapphire (Al_2O_3) substrate by exposing the substrate to nitrogen (N) plasma. A thin layer of aluminium nitride (AlN) would be subsequently formed on surface of the Al_2O_3 substrate. For Si substrate, an *in situ* Ga cleaning method was performed to remove surface contaminants, such as the oxygen impurities (O^-), which would tend to form silicon dioxide (SiO_2) on the Si substrate surface. By using the Ga cleaning process, the arriving Ga atoms would combine with the surface riding O^- to form gallium oxide (Ga_2O_3), which was very volatile at the high growth temperature. Hence, the Ga cleaning process was important to assist in minimizing critical accumulation of O^- that would distort the growth morphology of GaN epitaxial films.

The Ga cleaning process was proceeded with the deposition of AlN buffer layer for growth nucleation. The temperatures of both substrate and source would be increased appropriately in order to initiate the growth of the III-nitrides epilayers. During the growth process, parameters, such as materials flux and substrate temperature needed to be manipulated for optimization. Each growth step could be controlled *in situ* by RHEED, carried out using a bombardment of high energy (~ 20 keV) electron beam on the sample surface at a glancing angle, which would be subsequently reflected to a fluorescent screen. The reflection would give an imaging of the diffraction patterns for the determination of flux rate, surface quality, and surface reconstruction. For a semiconductor epilayer, the RHEED pattern would exhibit streaky lines or spots with high contrast and low background intensity, as shown in Fig. 3.3. The acquisition of

streaky lines indicated the presence of a flat and smooth surface on the epilayer while the spotty pattern was an indication of the formation of a rough surface or a three-dimensional (3D) growth behavior on the epilayer.



Fig. 3.2 PAMBE growth procedure of III-nitrides thin film on Si (111) and sapphire.

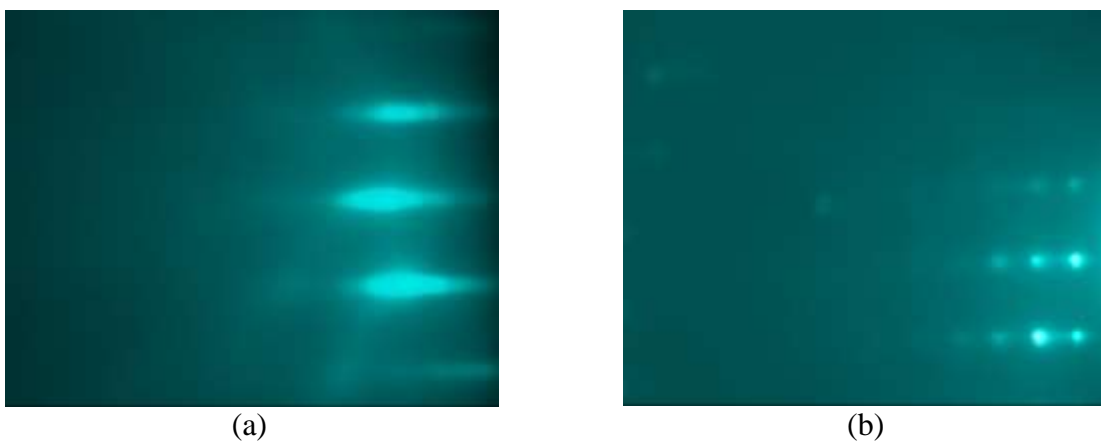


Fig. 3.3 A RHEED pattern with (a) streaky lines and (b) spotty pattern [18].

In fact, the selection of substrate materials used for GaN epitaxial growth is paramount in influencing growth behavior of the epilayers. Generally, close lattice-matched substrates have been the materials of choice, striving to reduce stress generation and dislocations in the epitaxial films. This has become one of the criteria used for the selection of substrate material. Besides, the substrate material must be chemically and mechanically stable at high temperature. Ideally, coefficient of linear expansion of the substrate and GaN should also be closely matched in order to prevent additional stress build-up that can cause film cracking, especially after the deposition process, in which the III-nitride films and substrate will be cooled down from high temperature to room temperature. In addition, the substrate material should be readily available in larger wafer size at a relatively low cost to be feasible for production scale devices. Moreover, in order to increase a device lifetime and allow the device to operate at higher power densities, the substrate material needs to possess high thermal conductivity. Whilst for optoelectronic applications, the substrate should have a large band gap and a high refractive index as to prevent the photons generated in the active layers of the films from being absorbed by the substrate [19]. For most of the applications, an electrically insulating or semi-insulating substrate would be the best choice but certain optoelectronic applications could benefit from an electrically conductive substrate.

Keeping view with the growth of III-nitrides films on different substrates, a lower cost, excellent wafer quality, and more design flexibility offered by the Si substrate with current Si-based electronic circuit system have suggested that Si substrate could be regarded as a viable growth foundation for the epitaxial films [20]. Nonetheless, further development of the heteroepitaxy of GaN on Si has been confronted by the difficulty in obtaining p-type (Mg) doping in the III-nitrides films, especially for the GaN epitaxial film. It has been reckoned that

high carrier concentration of p-type III-nitrides is a key factor, leading to the successful fabrication of high performance optoelectronics devices, such as LEDs and laser diodes (LDs). Therefore, controlling deep levels in the Mg doped GaN is one of the crucial aspects in optimizing the device performance.

To date, it remains challenging for the growth scientists to obtain good quality GaN-based epilayers with high p-type carrier concentration, owing to the occurrence of self-compensation and the presence of deep acceptor level created by the Mg doping atoms in the GaN films. In recent times, heavily Si-doped ($1-2 \times 10^{19} \text{ cm}^{-3}$) [21] and Mg-doped GaN ($4-5 \times 10^{20} \text{ cm}^{-3}$) [21-22] layers have been successfully grown on Si(111) by PAMBE. Fig. 3.4 (a) depicts the high resolution XRD (HRXRD) results obtained for the heavily doped p-type GaN epitaxially grown on Si(111) [21].

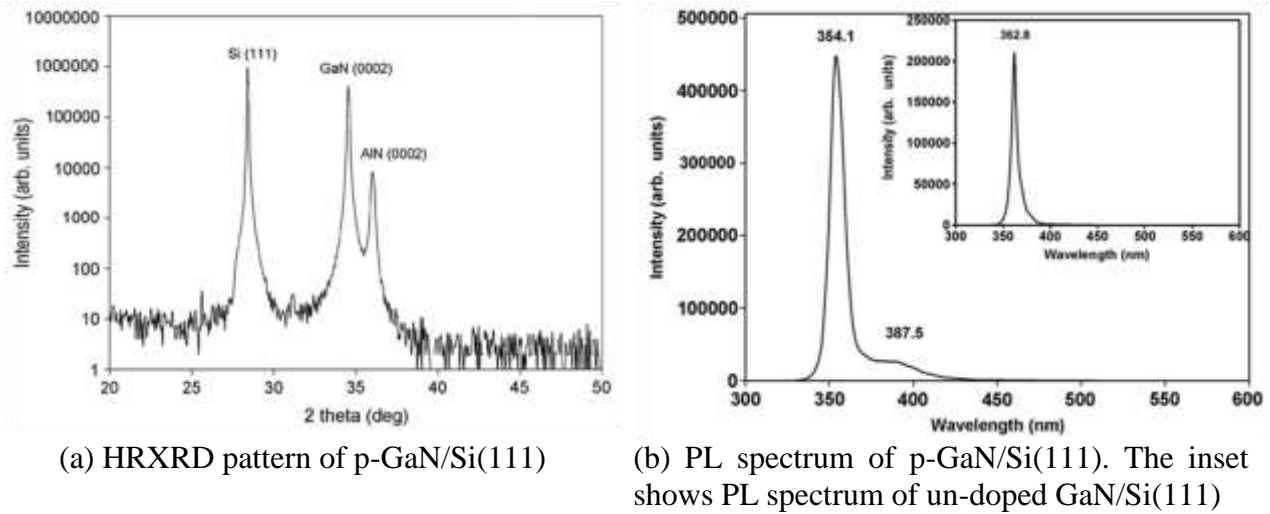


Fig. 3.4 (a) HRXRD and (b) PL spectra of GaN/Si(111) [21].

Photoluminescence (PL) measurement (Fig. 3.4 (b)) showed that a near band edge emission peak was detected at 354.1 nm, significantly blue-shifted from the typical reported value of 364 nm. The blue shift could be attributed to the Burstein–Moss effect. In addition, a broad emission peak observed at 387.5 nm could be due to a transition from conduction band

edge of the GaN to the Mg acceptor level. The absence of yellow emission peak revealed that no defect generation was present in the p-type GaN sample [21].

Besides, surface phonon polariton (SPP) studies of the wurtzite GaN thin film grown on c-plane Al₂O₃ substrate was also carried out. Since the knowledge on the SPP modes is crucial for understanding of the behavior of coupling effect between the photon and surface phonon, there is an absolute need for thorough studies on the surface properties of this material. For the experimental study, p-polarized IR attenuated total reflection (ATR) method shown in Fig. 3.5 (c) was used because the ATR method uses evanescent waves (EWs), which can directly excite the SPP [23]. Fig. 3.5 (a) shows the p-polarized IR ATR spectrum for the GaN thin film grown on c-plane Al₂O₃ substrate measured at room temperature [24]. The ATR spectrum for Al₂O₃ (Fig. 3.5 (b)) was also shown for comparison. It should be noted here that the measurements have been repeated at two different areas on the sample and the average values of these spectra are calculated. From Fig. 3.5 (a), it was found that the ATR spectrum exhibited a prominent absorption peak at $697.5 \pm 0.1 \text{ cm}^{-1}$ having a FWHM of $10.0 \pm 0.2 \text{ cm}^{-1}$, which can be attributed to the SPP mode of the GaN film [24].

Fig. 3.5 (b) shows the p-polarized IR ATR spectrum of bulk Al₂O₃ crystal. It was found that the Al₂O₃ exhibited two prominent absorption peaks at $629.0 \pm 0.2 \text{ cm}^{-1}$ and $743 \pm 3 \text{ cm}^{-1}$ [24]. Again, the latter peak has been assigned to the SPP mode of the Al₂O₃, while the origin for the former peak was still not clear at this time because it was very close to the LO (E_u (LO)₃) mode [25]. Besides that, an additional weak and broad peak which corresponded to the LO (E_u (LO)₄) mode of the sapphire was also observed at $893 \pm 1 \text{ cm}^{-1}$ [25], as shown in Fig. 3.5 (b). Nevertheless, neither these peaks were observed in Fig. 3.5 (a). Therefore, this led to the

conclusion that the features in Fig. 3.5 (a) were dominated by signals reflected from the GaN film [24].

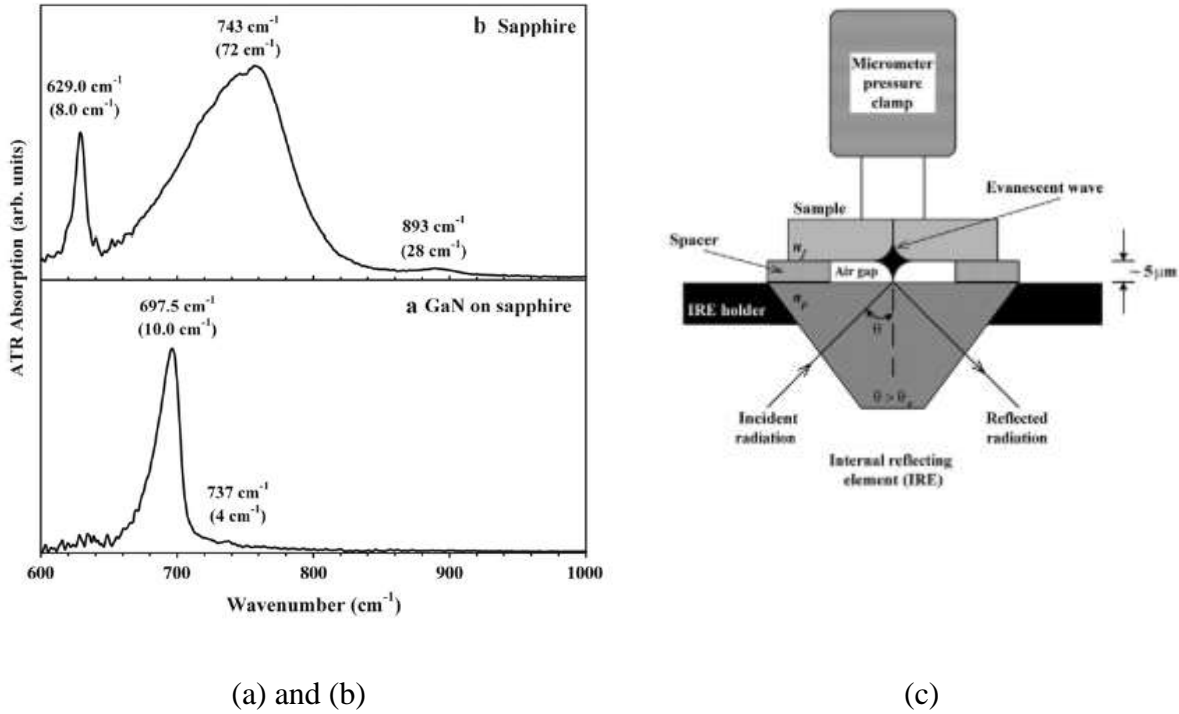


Fig. 3.5 Room temperature p-polarized IR ATR spectra for (a) GaN thin film grown on c-plane Al_2O_3 and (b) Al_2O_3 crystal as well as (d) typical set up for the measurement [24].

Apart from the epitaxial growth of GaN, another leap has been achieved in the development of nitrides-based devices via the successful growth of $\text{In}_x\text{Ga}_{1-x}\text{N}$, which is able to provide a wide band gap, ranging from about 0.7 eV ($x = 1$) to 3.4 eV ($x = 0$) within the blue/UV to infrared wavelength region. Nevertheless, the growth of $\text{In}_x\text{Ga}_{1-x}\text{N}$ was confronted by high equilibrium vapor pressure of N during the growth process. This phenomenon would impose serious problem in the growth of In-based nitrides compounds because of the high vapor pressure of N that would encourage the dissociation of In-N bond, leading to a desorption of In atoms from the growing surface. Therefore, lower growth temperature than that of GaN was preferred for InGaN epitaxial growth. In addition, high In concentration was unfavorable due to the

plausibility of phase separation to take place in the grown InGaN films. Furthermore, the large lattice mismatch between InGaN and GaN would create an in-plane biaxial stress in the InGaN/GaN heterostructures. As a consequence, a large piezoelectric field would be induced in the strained InGaN layer along a polar direction, affecting the long wavelength region of nitrides-based devices [26].

In this project, PAMBE growth of InGaN/GaN/AlN on Si(111) substrate has been also carried out [27]. It could be deduced from the HRXRD diffraction patterns in Fig. 3.6 for the presence of GaN (0002), AlN (0002), GaN (0004), and AlN (0004), respectively at 34.59°, 36.09°, 72.96°, and 76.50° along with a weaker diffraction peak at 32.99°, ascribed to InGaN (0002). The detection of these diffraction peaks signified the formation of heterostructure of III-nitrides epitaxially grown on Si(111).

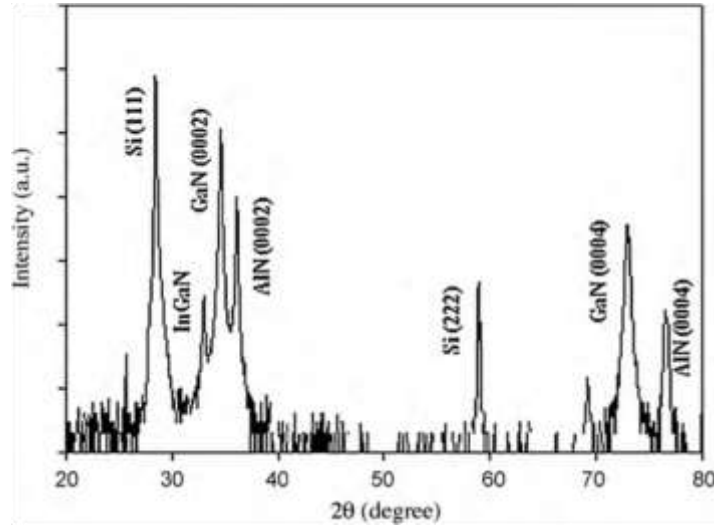


Fig. 3.6 HRXRD spectrum of the InGaN/GaN/AlN/Si(111) sample [27].

Table 3.1 summarizes the HRXRD peak position (2θ) and the corresponding crystal planes as well as the relative intensity detected for the investigated sample. Fig. 3.7 shows PL characteristics of the InGaN film grown on Si(111) using PAMBE. An intense and sharp peak

was detected at 362 nm, corresponding to the band edge emission of GaN. The detection of additional peaks at 403, 472 and 725 nm might be originated from the impurities or native defects (such as Mg, C or N vacancy, Ga vacancy) related recombination. Besides, a broad peak centered at 842 nm (1.47 eV), ascribed to the emission of InGaN was also detected [27].

Table 3.1 The HRXRD peak position (2θ), crystal planes, and relative intensity of InGaN/GaN/AlN/Si(111) [27].

Peak position (2θ) ($^\circ$)	Crystal plane	Relative Intensity (%)
28.457	Si (111)	100.00
32.986	InGaN	0.06
34.593	GaN (0002)	22.26
36.092	AlN (0002)	1.74
58.914	Si (222)	0.02
69.208	In	Too low
72.964	GaN (0004)	0.59
76.500	AlN (0004)	0.03

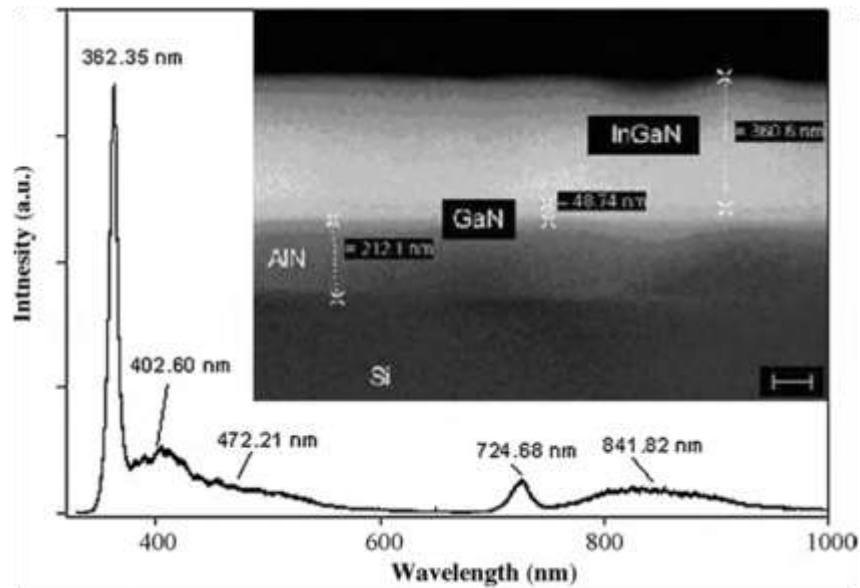


Fig. 3.7 PL spectra of InGaN/GaN/AlN/Si(111) sample. Inset shows cross-section of the sample, with scale bar rated at 100 nm [27].

In addition, high quality AlGaIn ternary alloy has also been grown on Si(111) using

PAMBE [27-35]. The HRXRD results in Fig. 3.8 (a) confirmed that all the structures of AlGa_N with different Al mole fraction were epitaxially grown on Si(111). It could also be seen that the peak of AlGa_N was shifted towards higher diffraction angle with the increase of Al mole fractions, indicating wurtzite structure of the AlGa_N films [35]. HRXRD rocking curve was also carried out to determine crystalline quality of the AlGa_N epilayers (Fig. 3.8 (b)). Results revealed that a relatively larger tensile strain has been perceived by the AlGa_N film containing the smallest Al mole fraction while a smaller compressive strain and larger grain size were detected in the AlGa_N film containing Al mole fraction of 0.30.

Apart from the growth of GaN, InGa_N, and AlGa_N epitaxial films on Si(111) substrates, subsequent effort has been dedicated to growing a pn-junction, which is of a great importance both in modern electronic applications and in understanding of other semiconductor devices. A high quality GaN pn-junction has been successfully grown on Si substrate using PAMBE [36-37]. The RHEED images depicted in Fig. 3.9 showed the formation of a good surface morphology of GaN pn-junction layer [36]. The thickness of GaN pn-junction layer was about 0.705 nm. The absence of cubic phase of GaN in HRXRD spectra (Fig. 3.10 (a)) confirmed the presence of hexagonal phases in the pn-junction layer. According to HRXRD symmetric rocking curve $\omega/2\theta$ scans of (0002) plane at room temperature, the full width at half maximum (FWHM) of GaN pn-junction sample was calculated as 0.34°, indicating a high quality layer of the GaN pn-junction. The absence of yellow band emission in PL spectra (Fig. 3.10 (b)) confirmed that the pn-junction layer was of a good optical quality [36].

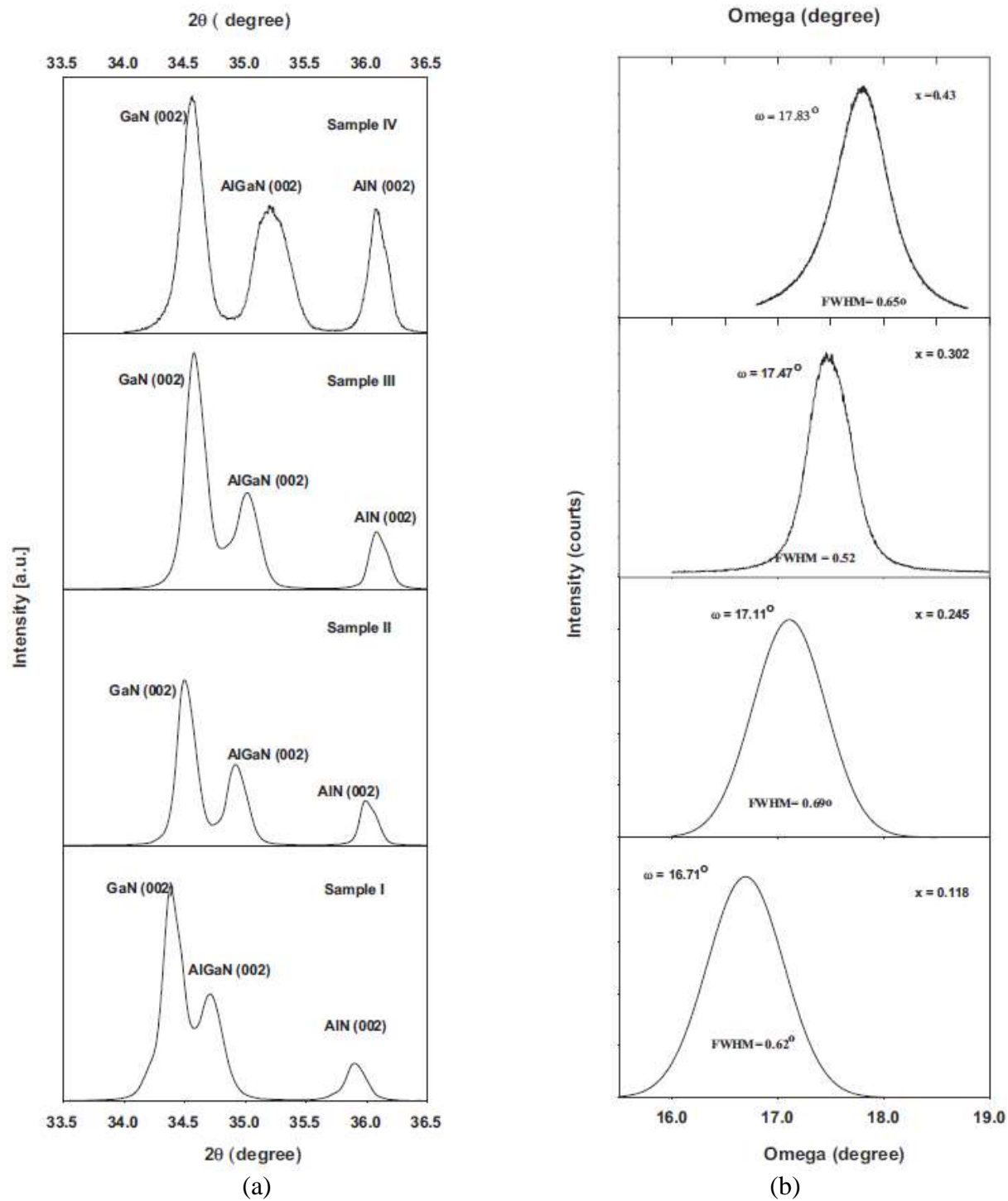


Fig. 3.8 (a) HRXRD spectra and (b) HRXRD rocking curve of AlGaIn with different Al mole fractions [35].

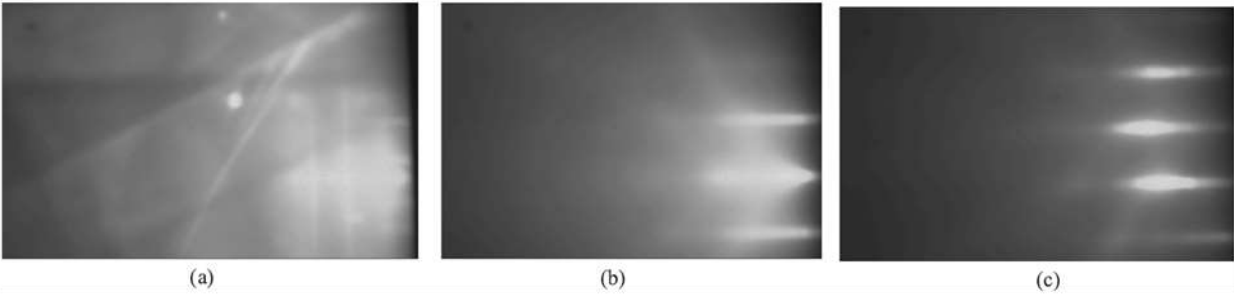


Fig. 3.9 RHEED pattern for the growth process of GaN pn-junction layer on AlN/Si(111). (a) Ga cleaning, (b) AlN, and (c) GaN [36].

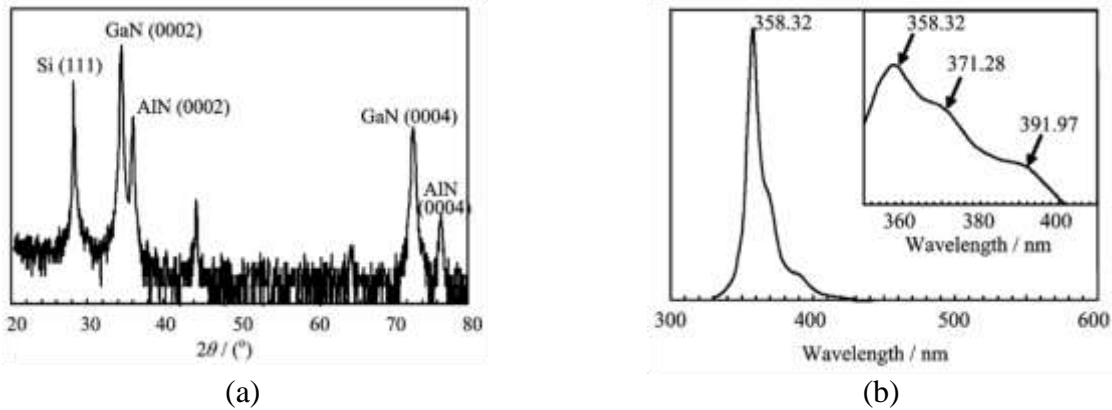


Fig. 3.10 (a) HRXRD spectra (b) PL spectra of GaN pn-junction layer [36].

4. Nanostructured III-Nitrides

Hitherto, nano-sized materials have attracted much attention because of the large surface areas and quantum confinement effects brought by the size of the materials within several nanometer dimensions towards an enhancement in electronic, magnetic, optical, and catalytic properties. Hence, inevitably superior performances have been established by the devices employing the nanostructures in contrast to the conventional devices without the nanostructures. Various synthetic methods of processing techniques, including vapor phase synthesis, solid state route and solution phase methods, have been employed to control the shapes and sizes of the nanostructures.

The research enthusiasm in fabricating nanostructured III-nitrides films was carried on by synthesizing GaN nanowires (NW) via chemical vapour deposition (CVD) route [38-43]. One-dimensional GaN NWs have been successfully synthesized on c-plane Al_2O_3 substrates in a conventional horizontal tube furnace system using high purity GaN powder (99.999% SigmaeAldrich) as the source material in the absence of metal catalyst [38-43]. Fig. 4.1 presents the FESEM images of GaN nanostructures grown on c-plane Al_2O_3 using different flow rates of NH_3 reactive gas at a constant growth temperature ($T = 1000^\circ\text{C}$) [40]. Surface morphology of the GaN nanostructures revealed that three different shapes were obtained as the flow rate was altered. At low flow rate (75 sccm), thin film-like GaN nanostructure was obtained (Figs. 4.1 (a)-(b)). A considerable change of shape and size occurred as the flow rate was changed to medium rate (100 sccm), in which zigzagged shaped GaN NWs with high aspect ratio and in a diameter range of 30–180 nm and several micrometers in length emerged (Figs. 4.1 (c)–(f)) on the substrate. At low magnification, it could be noticeably observed that the sample was composed of a huge number of NWs that crossed each other as well as dispersed uniformly over a large area of the substrate. Finally, further increase of the flow rate up to 125 sccm has resulted in changes again in both the shape and size; microstructures were observed (Figs. 4.1 (g)-(h)) [40]. A metal nanoparticle catalyst was not observed clearly on the tip of the NWs even under the high magnification FESEM images (Figs. 4.1 (c)-(d)). This could be an indication of the consumption and desorption of Ga (high growth temperature), which suggested that the growth of GaN NWs on the Al_2O_3 substrate has been realized via the vapor solid (VS) process [40].

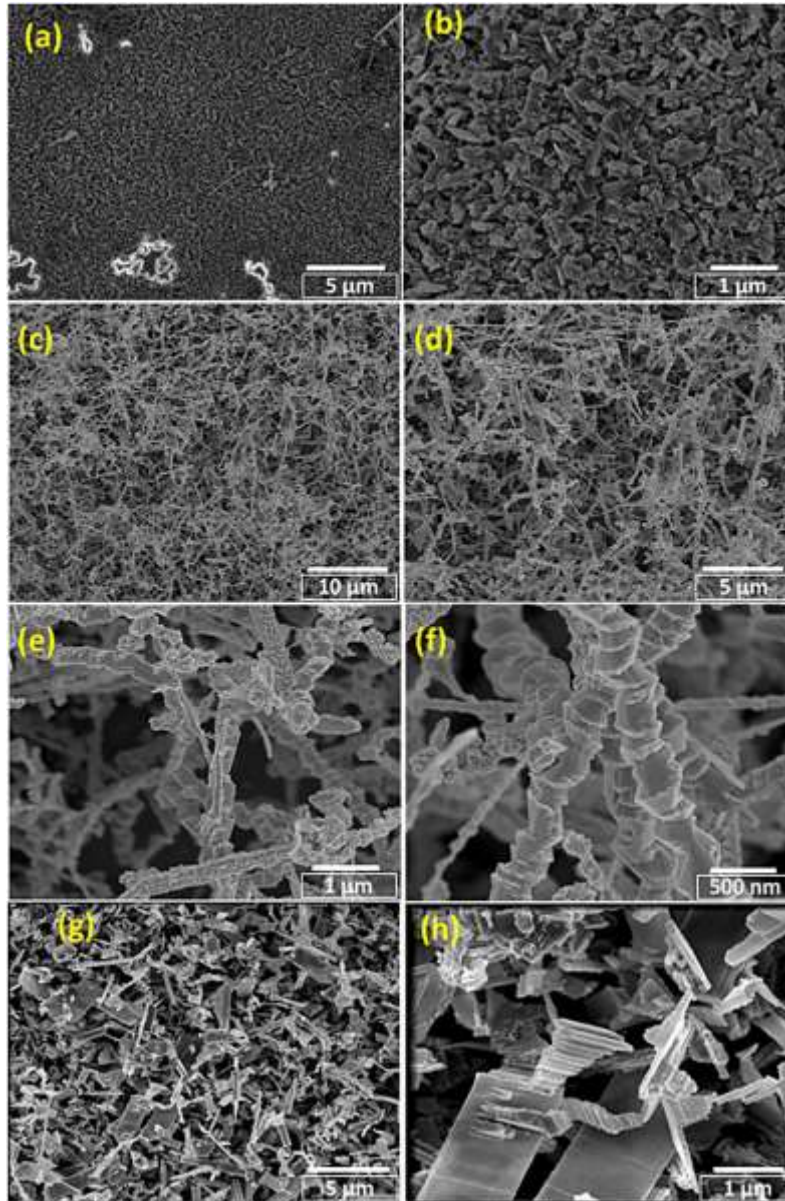


Fig. 4.1 Low- and high- magnification FESEM images of GaN nanostructures grown on c-plane Al_2O_3 substrates using tube furnace under different flow rates of NH_3 gas: (a)-(b) 75 sccm, (c)-(f) 100 sccm, and (g)-(h) 125 sccm [40].

Recently, semiconductor quantum dots (QDs), which are the 3D confined quantum structures, have been extensively investigated for the development of optoelectronic devices. Lasers with QDs embedded in the active layer are predicted to improve the characteristics of lasers, such as a suppression of temperature dependence of the threshold current, a reduced

threshold current density, and a reduced total threshold current. The use of QDs has been widespread in the nitrides-based semiconductors due to the zero-dimensional electronic states in the QDs that would play an essential role in improving threshold current characteristics of the devices. Moreover, the absence of dislocations in the QDs is expected to impart higher efficiency as the carriers confined inside the QDs would not be trapped at non-radiative recombination centers formed by the dislocations [44]. It has been also reported that the performance of InGaN laser could be improved enormously by introducing InGaN QDs into the device active layer, and thereafter yielding a higher brightness, a lower threshold currents, and better temperature stability [45].

High quality self-assembled InGaN QDs have been successfully grown by PAMBE on Si(111) in this work [18]. The growth of InGaN QDs has been investigated *in situ* by RHEED. It was deduced from this study that a low temperature growth of the InGaN QDs has instantaneously led to the formation of 3D islands, as confirmed by the RHEED pattern in Fig. 4.2. Surface morphology of the InGaN QDs grown on Si(111) substrate has been examined using field emission scanning electron microscopy (FESEM) (Fig. 4.3 (a)). It was found that the diameters of the InGaN QDs were in the range of 20–25 nm as compared to Kadir *et al.* [46], in which the mean size of the typical QDs was reported to be about 40 nm in diameter. Ji *et al.* [47] on the other hand revealed the formation of big oval InGaN QDs without any growth interruption. It was reported that a longer width of the oval QDs was around 140 nm while a shorter width of the oval QDs was about 70 nm. These findings suggested that the zero-dimensional quantum effects could be significantly enhanced in the samples grown using RF-PAMBE in this work without the introduction of growth interruption. Fig. 4.3 (b) shows surface topography of the

InGaN QDs inspected using AFM at a scan area of $500 \text{ nm} \times 500 \text{ nm}$. The corresponding rms roughness of the QDs was 2.35 nm .

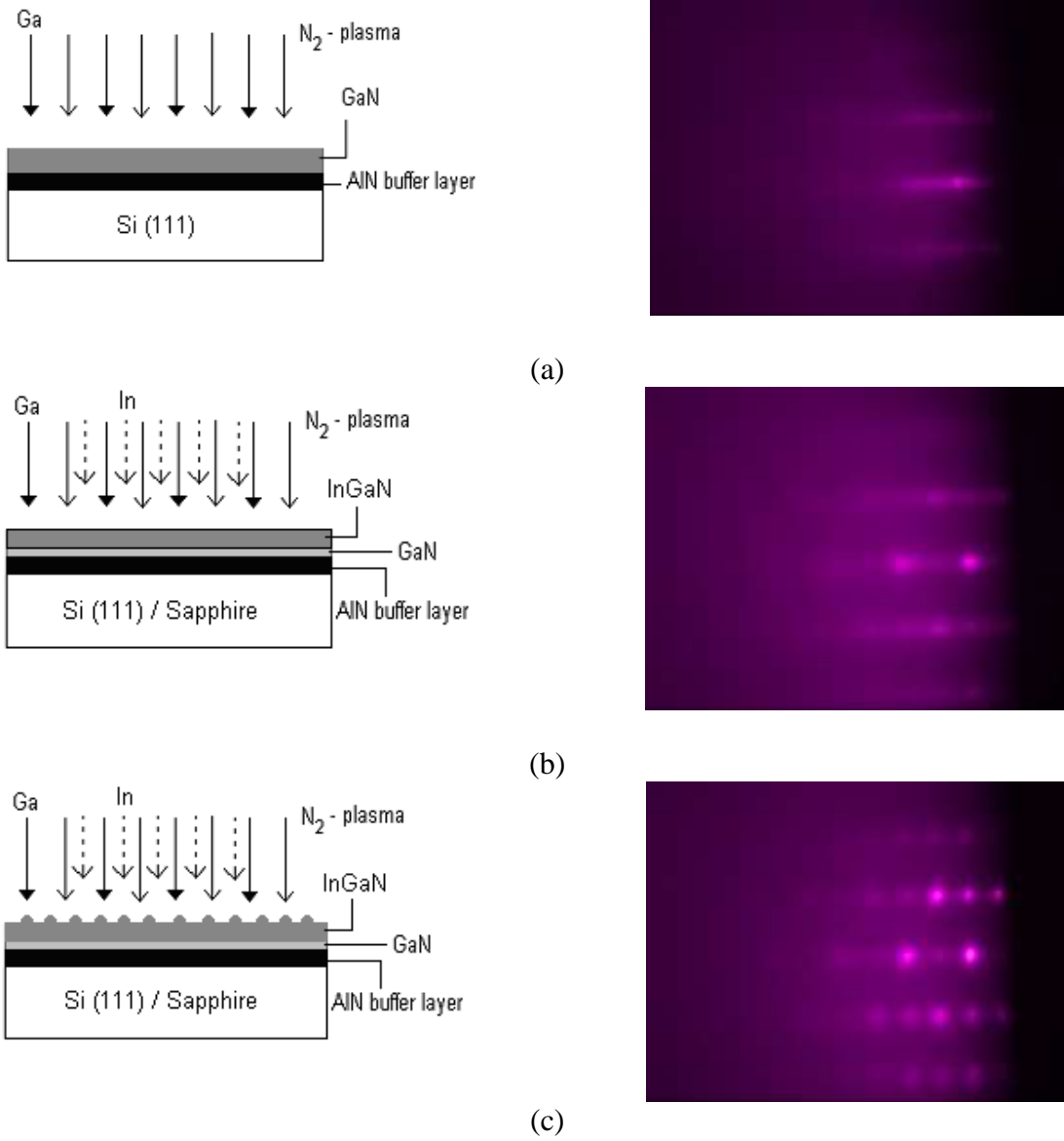


Fig. 4.2 RHEED patterns of (a) GaN wetting layer (b) InGaN epilayer (c) InGaN QDs [18].

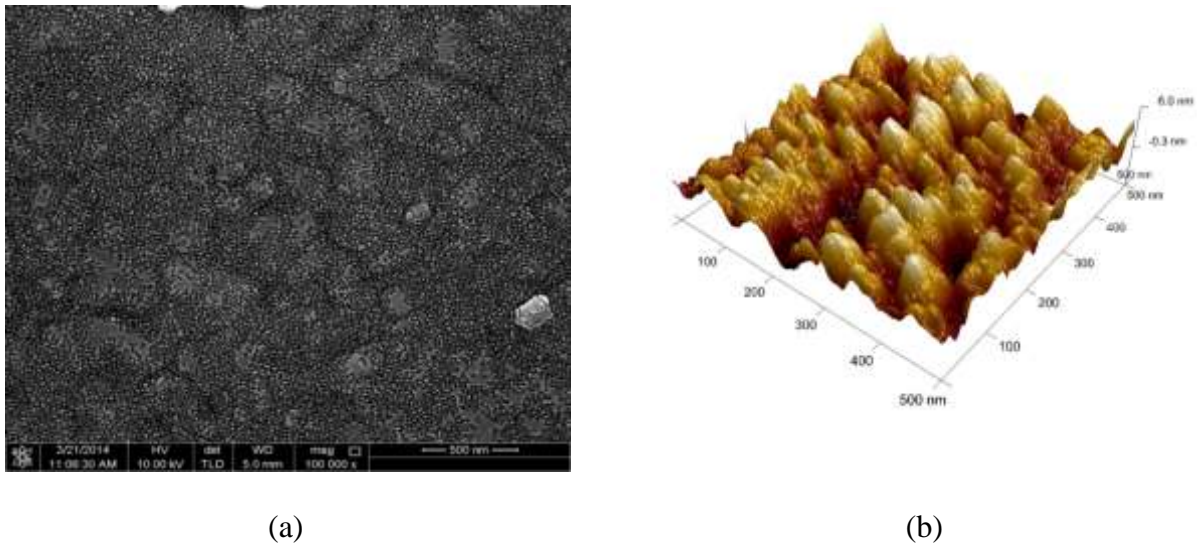


Fig. 4.3 (a) FESEM and (b) AFM images of InGaN QDs grown on Si(111) [18].

Another semiconductor material of interest for potential use in optoelectronic devices, such as high efficiency solar cells, high electron mobility sensors, and transistors, has been associated with the wurtzite structure of indium nitride (InN), exhibiting a band gap range from 0.7 eV to 1.9 eV [48-52]. Owing to the low dissociation temperature of InN, the InN films are usually deposited at low temperatures as to avoid re-evaporation of the N atoms. Amongst the techniques that have been reported for deposition of InN films, reactive sputtering has emerged as one of the most promising techniques from the viewpoint of low temperature film growth.

It has been reported in literatures that the band gap of InN films was strongly dependent on the growth conditions, in which dissimilar growth conditions would lead to the changes in the band gap value. Amongst the factors that might be taken into consideration include Burstein–Moss energy shifts [53], the presence of oxide precipitates [54], and other stoichiometry-related defects [49]. However, it remains vague for the stoichiometry between the In and N in the InN films as the related effects have not been clearly elucidated. Thus far, research outcome obtained from previous study showed that the growth of InN films under thermal equilibrium condition

was impossible to result in N-rich InN films [52]. On the other hand, the use of plasma sources as in the radio-frequency (RF) sputtering technique could create a non-equilibrium growth regime for the growth of N-rich InN films, which has in turn contributed to a large variation in the band gap obtained [55]. This occurrence might be attributed to the changes in material stoichiometry, and thus further investigation was required.

Dissimilar from previous studies, the present study reported about the growth of InN films on porous (PSi(110)) and non-porous Si(110) substrates using reactive RF sputtering technique in order to investigate the corresponding effects brought by the substrate towards optical properties of the InN films [56-58]. Fig. 4.4 shows the PL spectra obtained for InN films deposited on Si(110) and porous Si(110) substrates.

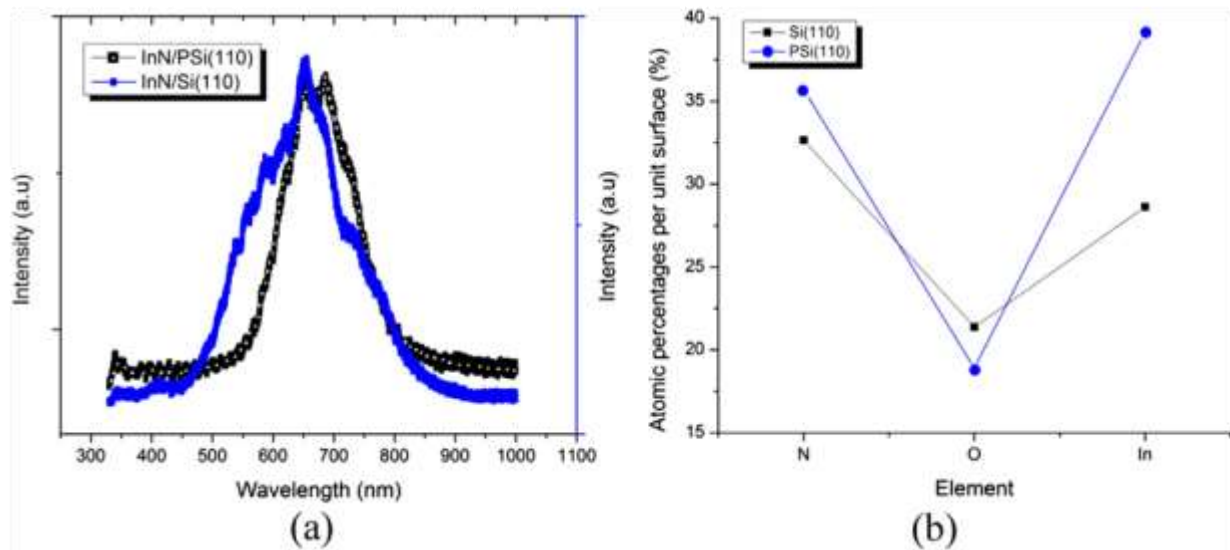


Fig. 4.4 (a) PL spectra and, (b) The In, N, and oxygen atomic percentages per unit surface of InN samples grown on non-porous Si(110) and porous Si(110) (PSi(111)) substrates [57].

A relatively stronger emission peak intensity was observed in the 1.8 eV-1.98 eV energy range for the InN film grown on non-porous Si(110) at room temperature as compared to that for the porous Si(110). However, the InN film grown on the porous Si(110) has demonstrated

higher N content than the one grown on the non-porous substrate. This finding signified that the substrate condition has also influenced the growth of InN film. Besides that, the growth of InN on different substrates such as SiC has also been investigated [59-62].

Nanocrystalline InN films have been prepared by multiple methods, MOCVD [63] and RF sputtering [64]. MOCVD and MBE can be used to grow single crystalline InN. However, high processing cost is involved and the size of the grown epilayers is limited. Generally, RF sputtering can be used in preference to MOCVD and MBE to fabricate noncrystalline or polycrystalline InN [56]. Surface morphology of the nanocrystalline InN thin film deposited on Si(110) could be clearly seen in Fig. 4.5 via the formation of agglomerated nanocrystals on the film surface. Cross-sectional SEM images revealed the formation of 0.38, 0.45, and 0.70 μm thick InN films on the Si(110) substrates in the samples exposed to deposition gas containing 100% N_2 , 75% N_2 , and 50% N_2 , respectively (Fig. 4.6) [56]. This observation indicated that an increase in the Ar content of the gas ambient has assisted in increasing the thickness of the InN film. The occurrence of this might be related to the fact that nitrogen has a higher electron capture ability and a lower sputtering yield than Ar. Therefore, the increase in Ar content would increase density of the plasmas. Consequently, the high density of plasma would be able to sputter more In particles from the target to be reacted with the N_2 from the ambient, leading to the formation of more InN particles on the substrates. Eventually, an increase in the thickness of InN film was obtained [56].

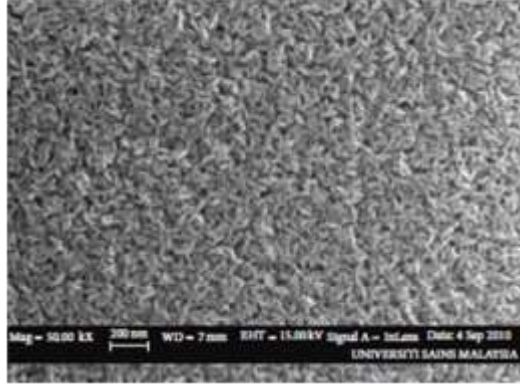


Fig. 4.5 FESEM image of nanocrystalline InN film grown on Si(110) [56].

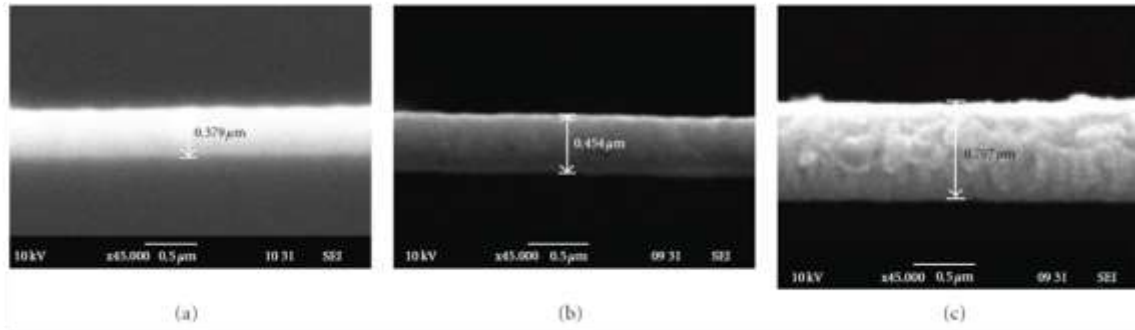


Fig. 4.6 Cross-sectional FESEM images of InN films grown on Si(110) with respect to the deposition gas [(a) 100% N₂, (b) 75% N₂-25% Ar, and (c) 50% N₂-50% Ar] [56].

5. Porous III-Nitrides

Porous semiconductors have been widely studied in the last decade, primarily due to the potential for intentional engineering of properties not readily obtained in the corresponding crystalline precursors as well as the potential applications in optoelectronics, chemical and biochemical sensing. Among the porous semiconductors, porous Si has received enormous attention and has been investigated most intensively. However, the instability of physical properties has prevented large scale application of porous Si. A shift of the porous technology has been thereafter extended to other porous semiconductors, such as the conventional gallium arsenide (GaAs), gallium phosphide (GaP), and indium phosphide (InP) as well as the wide band gap GaN and SiC.

Porous III-nitrides semiconductors, particularly the porous GaN has long been placed in the forefront of technology, owing to superb physical properties provided, which include excellent thermal, mechanical, and chemical stability as well as a potential shift of band gap. Throughout the years, various processing techniques have been established in the fabrication of porous III-nitrides semiconductors. Owing to the excellent chemical stability and high hardness of the III-nitrides semiconductors, chemical or electrochemical etching techniques might not be efficient in forming porous structures on the materials [65]. On the other hand, dry etching technique could be a feasible technique to produce porous III-nitrides semiconductors yet possible occurrence of surface-induced damage on the semiconductor surface as well as a lack of desired selectivity towards morphology, dopant, and composition have restrained continuous employment of dry etching techniques [66].

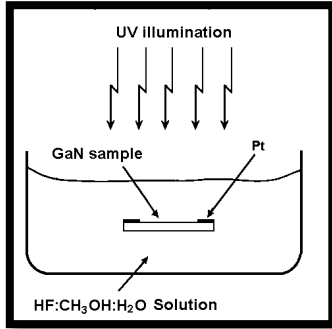
Photoelectrochemical (PEC) etching has been regarded as an improvised technique that incorporates the use of an incident photon with optical energy greater than the band gap of the semiconductors to generate electron-hole pairs for etching of the III-nitrides semiconductors. Furthermore, PEC etching would allow the formation of porous or smooth surfaces by offering anisotropic and dopant-selective etching [67] on the semiconductors. Nonetheless, PEC etching might not be suitable for use in large area porous formation on the III-nitrides semiconductors, attributable to dissimilar etching rates induced on different sites on the etched surfaces [68]. It has been reported that metal-assisted electroless chemical etching technique could be a remedy in fabricating homogeneous porous morphology over the large area of the III-nitrides semiconductors [69-71].

A greater breakthrough was accomplished in the development of pore geometries on porous III-nitrides semiconductors by broadening the porous technology from the binary GaN

[72-73] to ternary InGaN [74-77] and quaternary InAlGaN [78-79]. In this work, three different techniques, namely the metal-assisted ultraviolet (UV) electroless etching, UV-assisted PEC etching, and laser-induced electrochemical etching methods were employed to produce the nanostructured porous III-nitrides (GaN, InGaN, and InAlGaN) semiconductors. Fig. 5.1 shows schematic diagrams of (a) metal-assisted UV electroless etching [80], (b) UV-assisted PEC etching [81-87], and (c) laser-induced etching [72]. In order to evaluate the effects of different etching parameters on structural, optical, and electrical properties of the porous III-nitrides, various parameters, including the electrolyte concentration, anodization duration, and applied voltage were studied for investigation. After the etching process, the samples were removed from the solution and rinsed with distilled water.

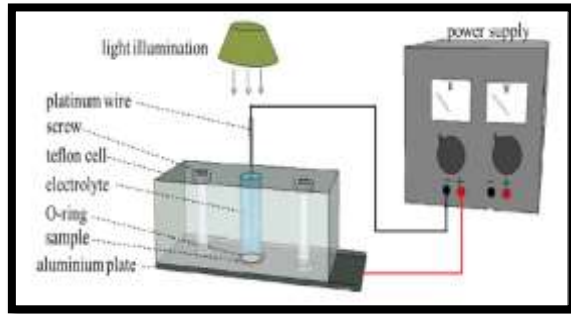
Porous GaN has been successfully fabricated using Pt-assisted UV electroless etching technique using 1:2:2 volume ratios of $\text{CH}_3\text{OH}:\text{HF}:\text{H}_2\text{O}_2$, $\text{CH}_3\text{OH}:\text{HNO}_3:\text{H}_2\text{O}_2$, and $\text{CH}_3\text{OH}:\text{H}_2\text{SO}_4:\text{H}_2\text{O}_2$. FESEM images depicted in Fig. 5.2 reveals the formation of uniformly distributed pores in all the etched GaN samples. Excellent porous network without any ridge morphology was obtained. In comparison, the smallest pore size was obtained for the GaN etched using the HNO_3 -based etchant while the largest pore size was obtained for the GaN etched using the HF-based etchant.

Raman studies ((Fig. 5.3 (a)) have detected the existence of E_2 (TO) and A_1 (LO) phonon modes [88] of hexagonal GaN in all of the investigated non-porous and porous GaN samples. The absence of disorder-activated phonon modes in the recorded Raman spectra confirmed good crystalline quality of the porous structures [89]. Fig. 5.3 (b) depicts PL emission spectra of the porous GaN samples in comparison to the non-porous sample. All of the porous samples have exhibited higher peak intensity than the non-porous sample.



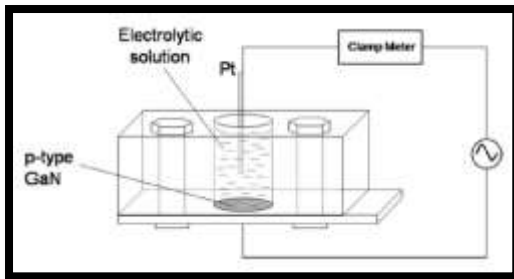
- Platinum (Pt) was coated on both sides of GaN sample.
- The sample was immersed in etch solution.
- The etching process was done under the illumination of a 500 W UV lamp for a certain duration.

(a) Metal-assisted UV electroless etching [80, 83]



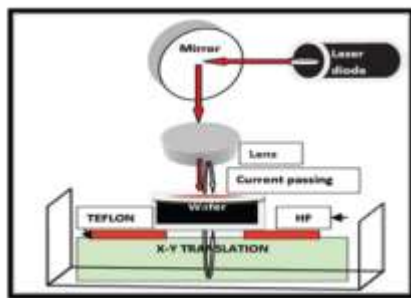
- GaN sample was fixed as a working electrode and Pt wire was used as a counter electrode (cathode).
- GaN sample was immersed in etch solution under UV illumination for a certain duration.
- Positive and negative terminals of DC power supply was connected respectively to the Al plate and Pt wire.

(b)(i) UV-assisted PEC etching (DC external source) [81]



- GaN sample was fixed at the bottom of a Teflon cavity cell contacted with a stainless steel plate.
- One output terminal of a variac AC power regulator was connected to Pt wire that was immersed in the etch solution and the other one was connected to the plate.

(b)(ii) UV-assisted PEC etching (AC external source) [87]



- The GaN wafer was immersed in etch solution placed in a plastic container and was supported on two Teflon plates.
- Laser-induced etching (LIE) was done at room temperature by using continuous wavelength (CW) laser diode beam ($\lambda = 635 \text{ nm}$, 1.95 eV) at 1 mm diameter

(c) Laser-induced etching [72]

Fig. 5.1 Fabrication of porous III-nitrides by different techniques.

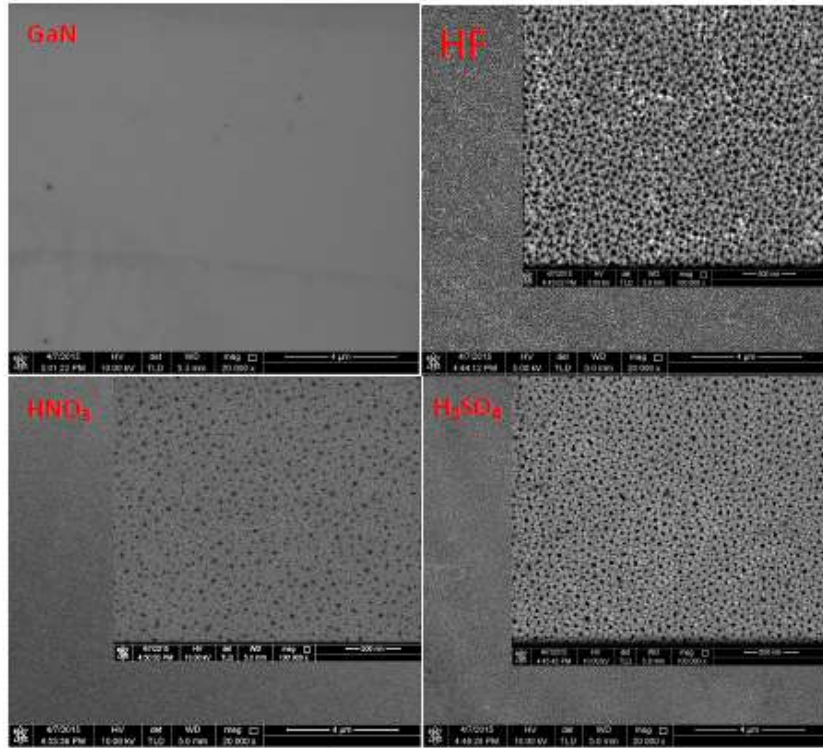


Fig. 5.2 FESEM images of porous GaN samples obtained by etching in different etchant solutions [80].

The improvement in PL emission peak intensity might be caused by the high surface area to volume ratio of the porous structures that has increased the number of participating electrons in the PL process [90]. As a consequence, more light extraction off the sidewalls of porous structures was achieved, and hence resulting in an enhancement in the PL efficiency by several orders of magnitude. In contrast, the porous GaN obtained by etching in HF-based etchant has shown the highest PL intensity. Besides, it was worth noting that sharper and narrower PL emission peaks were perceived by the porous GaN samples relative to that of the non-porous sample, indicating an improvement in crystalline quality of the samples after the formation of porous structures.

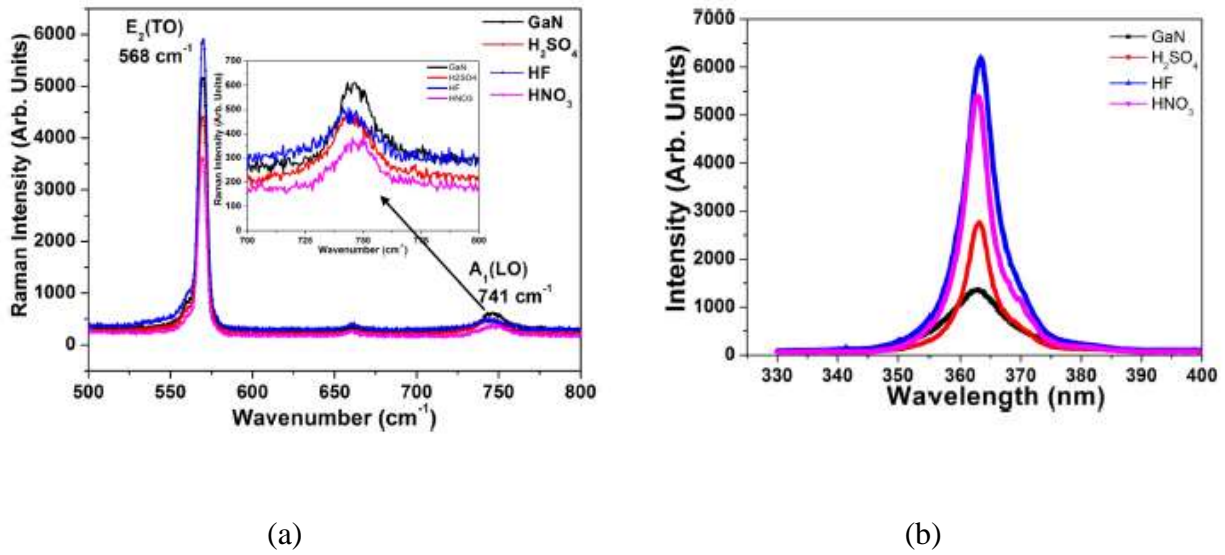


Fig. 5.3 (a) Raman and (b) PL spectra of non-porous and porous GaN samples obtained by etching in different etchant solutions [80].

The porous InGaN ternary alloy was successfully synthesized by UV-assisted PEC etching under various conditions. Fig. 5.4 shows the FESEM images of the pre- and post-etched InGaN thin films. In Fig. 5.4 (a), the as-grown film has sufficiently smooth surface and uniformly over a large region [76]. Inset presents cross section of the thin film, showing 1 μm and 0.1 μm thick for the thickness of InGaN and AlN buffer layer, respectively. Figs. 5.4 (b)–(d) show FESEM images of the porous InGaN surfaces. Coral-like ridges started to form and the surface became rough during the etching duration of 5 min (Fig. 5.4 (b)); irregular shapes of ridges with different sizes were found. Increasing the duration to 10 min (Fig. 5.4 (c)) and 15 min (Fig. 5.4 (d)) has led to an increase in the number of corals-like ridges, which became the greatest at 15 min. This study concluded that the etching duration could affect the shape and size of the pores [76].

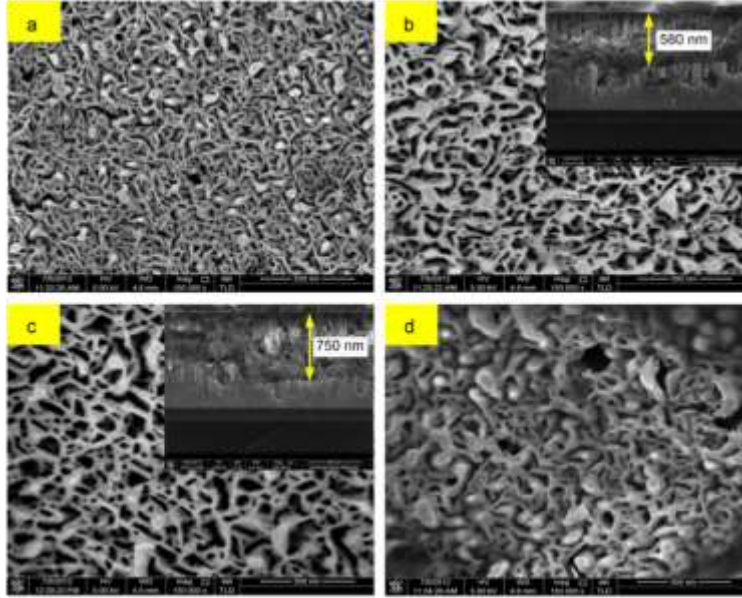


Fig. 5.4 FESEM images of the porous InGaN at a ratio of 1:4 and under various etching durations: (a) 5 min; (b) 10 min; (c) 15 min; and (d) 20 min [76].

Fig. 5.5 shows the PL spectra of the InGaN thin films at pre- and post- etching for 5, 10, 15, and 20 min [77]. In Fig. 5.5 (a), the PL intensity of the etched films increased with longer etching duration, reaching the maximum value at 15min, and then decreased at 20 min. Blue shifts were observed in the spectra of the post-etched films (compared to the as-grown). The high porosity-induced PL intensity could be explained by the extraction of strong PL via light scattering from the side walls of the sample crystallites [91]. Compared with the as-grown films, porous films have higher surface area per unit volume; thus, porous InGaN would provide much exposure to the illumination of PL excitation light for the InGaN molecules. This phenomenon might result in a higher number of electrons in excitation and recombination in porous films compared with the case involving a small surface area of as-grown films [90]. The energy gap was increased from 3.08 eV (403 nm) for the pre-etched thin film to 3.18 eV (390 nm) for the post-etched thin film at 15 min.

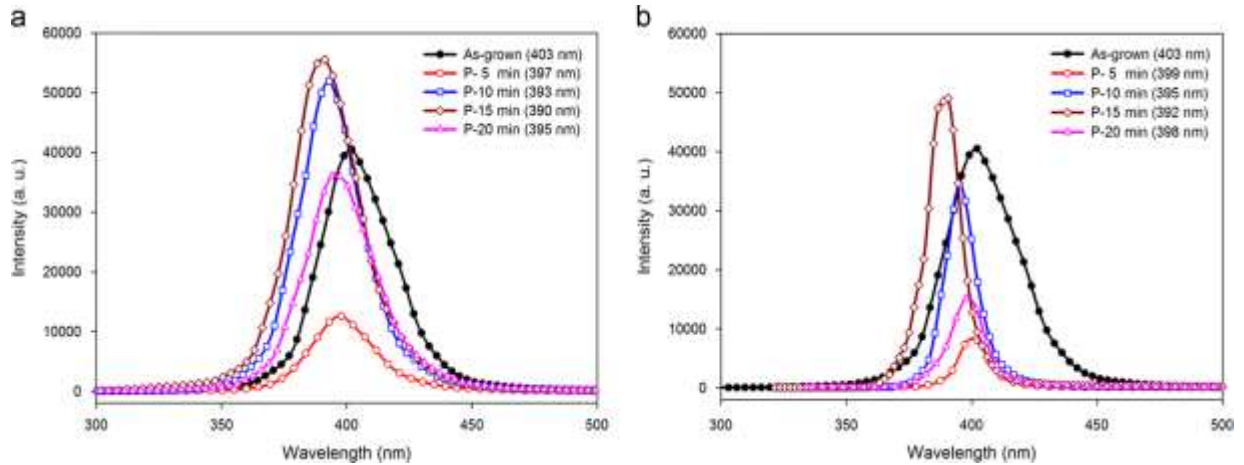


Fig. 5.5 Comparison of PL spectra of porous InGaN and as-grown film [77].

In essence, beneficial effects brought by porous GaN and porous InGaN in the aspects of an enhancement in PL intensity, an improvement in internal quantum efficiency and light extraction efficiency, as well as a relaxation of compressive stress with decreased dislocation density have provoked considerable interest on formation of pore geometry in the quaternary InAlGaN layer. Moreover, the aforementioned benefits of porous formation revealed significance of the porous III-nitrides semiconductors as templates for growth of subsequent overgrown layers.

Thus far, Radzali *et al.* has fabricated porous InAlGaN layer using photo-electrochemical (PEC) etching in a diluted potassium hydroxide (KOH) solution under illumination of Xenon lamp [92]. In comparison to non-porous InAlGaN layer, a relaxation of compressive stress was attained in the porous layers etched under different etching durations. Though the pore density was relatively low, an improvement in the PL intensity and a relaxation of compressive stress have been demonstrated by the porous InAlGaN sample relative to the non-porous sample when the etching was performed in various etching current densities (20, 40, 80, and 160 mA/cm²) [92]. According to the study, an acquisition of the highest PL intensity and the largest band gap of

3.24 eV have brought to an improvement in optical behaviors of the InAlGaN sample etched at 80 mA/cm². As the work reported for porous quaternary InAlGaN alloy is meager, it is of interest in present work to investigate the influence of different KOH concentrations towards structural, physical, and optical properties of the porous InAlGaN layers using UV-assisted PEC etching technique under a constant etching current density of 80 mA/cm² [92].

Fig. 5.6 shows the top view images of the non-porous and porous InAlGaN samples subjected to different etching durations. The nonporous InAlGaN sample had a smooth and flat surface morphology. After 1 min of etching, small pores began to form on the surface. The pore density increased as the etching duration increased to 5 min. After 10 min of etching, pore formation became more pronounced. At this stage, a rough surface with a coral-like porous structure and increased pore density was visible. On the other hand, after 15 min of etching, deeper pore walls (visible as darker areas) were more prominent. Further etching up to 20 min, most of the InAlGaN layer was etched away, revealing more Si areas. By this time point, the etching activity was more devoted to removing the InAlGaN layer than to generating the porous structure [92].

Fig. 5.7 shows the 2 θ -scan HRXRD patterns for the non-porous and porous InAlGaN samples at different etching durations [92]. For the non-porous sample, a single InAlGaN (0002) peak was visible at 34.59° as well as InAlGaN (0004) peak was present at 72.96°. In addition, the (0002) and (0004) peaks that originated from the AlN layer were visible at 36.06° and 76.48°, respectively. The Si(111) substrate peak was located at 28.44°. It is interesting to note that the InAlGaN related peak was present in all porous samples, which showed that the InAlGaN layer has not been entirely etched away. However, the relative intensity of the InAlGaN (0002) peak decreased with etching duration due to the removal of some of the InAlGaN crystals (inset of Fig.

5.7) [92]. This result was in line with the FESEM images in Fig. 5.6, which showed that more of the InAlGaN layer was etched away as the etching time was increased from 15 to 20 min. In addition, the diffraction peak position of InAlGaN (0002) for the porous samples was shifted to a higher angle compared to that of the non-porous sample, indicating a change in composition of group III elements in the InAlGaN layer as a consequence of etching [92].

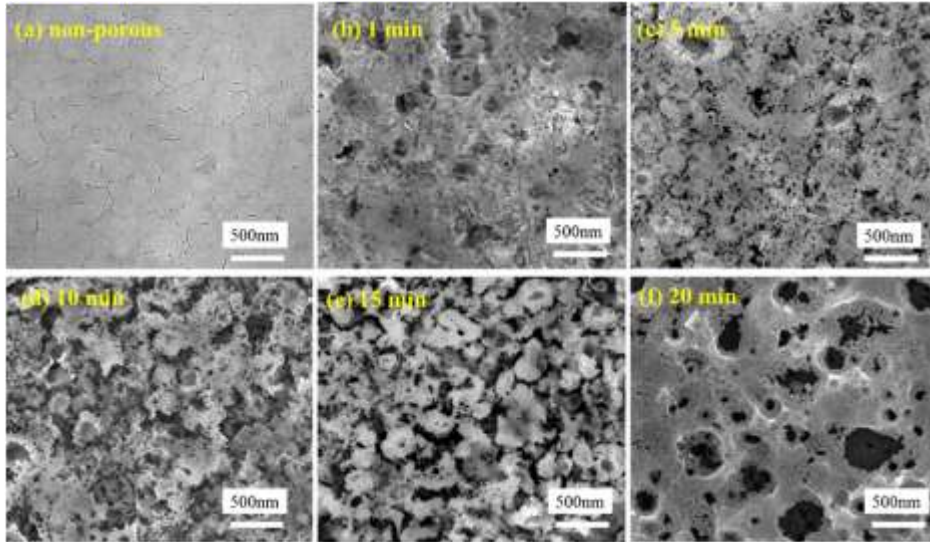


Fig. 5.6 FESEM images of the non-porous and porous InAlGaN samples etched for different etching durations [92].

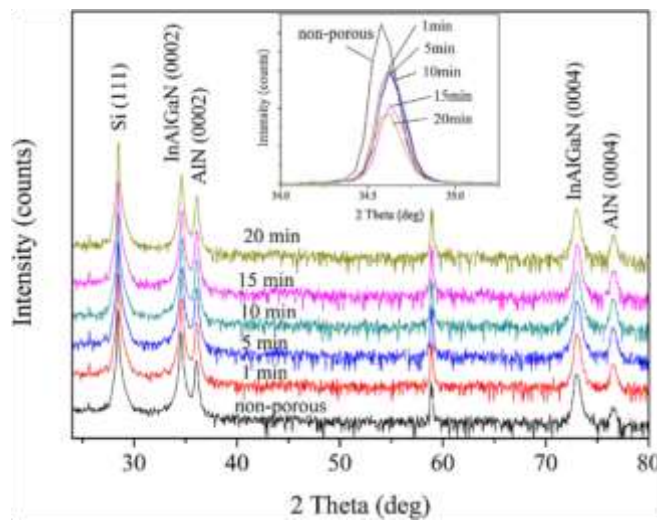


Fig. 5.7 2θ scan HRXRD patterns of non-porous and porous samples; the inset shows the magnified InAlGaN (0002) peaks [92].

A novel AC (sinewave a.c. (50 Hz)) UV-assisted electrochemical etching, termed as ACPEC has been studied to grow a high quality porous GaN [86] with excellent structural and optical properties. FESEM micrographs shown in Fig. 5.8 indicated the formation of hexagonal-like and nano building structures with different sizes in the porous GaN obtained by ACPEC technique. The average pore size determined for the porous GaN obtained by etching for 45 min and 90 min was about 35-40 nm and 55-60 nm, respectively. Fig. 5.9 (a) depicts the PL spectra obtained for the porous GaN in comparison to the non-porous GaN. Results showed that the porous layer exhibited a substantial enhancement in the PL intensity with a red-shifted band-edge, which might be related to a relaxation of compressive stress after porosification. The shift of E_2 (high) Raman mode to a lower frequency ((Fig. 5.9 (b)) further confirmed the occurrence of stress relaxation in the porous GaN films [86].

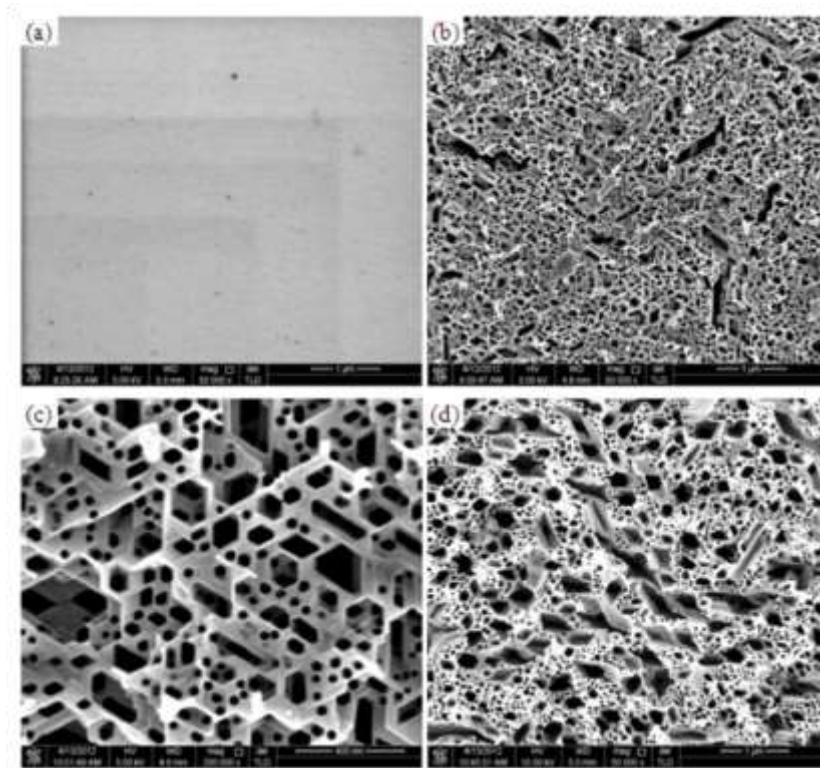
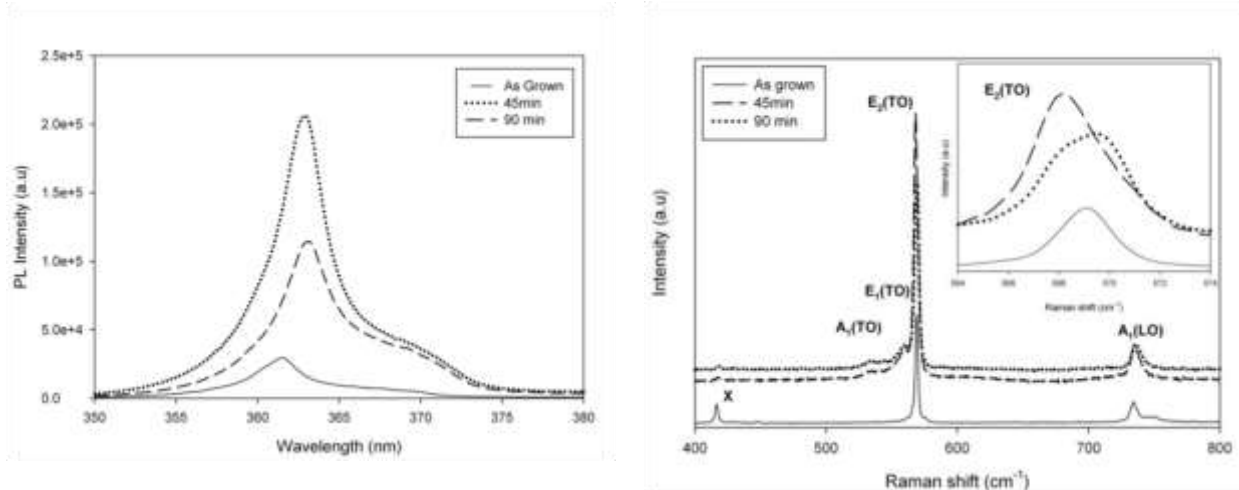


Fig. 5.8 FESEM images of the (a) as-grown and porous GaN films obtained by ACPEC etching at (b) 45 min, (c) 45 min (high magnification), and (d) 90 min [86].



(a)

(b)

Fig. 5.9 (a) The near band edge PL spectra and (b) Raman spectra of the samples etched under different durations measured at room temperature [86]. Inset shows the shift of E₂ (high) Raman mode of the porous films.

In recent study, the novel ACPEC etching technique has been successfully used to fabricate porous structures in p-type GaN. The reason of selecting AC as the external source to fabricate porous p-type GaN was owing to the ability of AC current to travel in a sinusoidal form that changes from a positive to a negative half cycle. This could be advantageous to solve the downward band bending issue at the p-type GaN/electrolyte interface, in which simultaneous oxidative decomposition of the GaN surface and cathodic reduction of solution species could take place. A constant AC current of 40, 60, 80 and 100 mA was supplied to the investigated films during ACPEC etching process for 90 min under UV illumination by regulating the variac voltage to obtain the desired AC current value (40–100 mA), in which the current reading was monitored using a clamp meter [87].

Surface morphologies of the porous p-type GaN films are presented in Figs. 5.10 (b)-(e) in comparison to the non-porous film ((Fig. 5.10 (a)). PL measurement in a wavelength ranging from 330 nm to 700 nm was performed on the investigated films at room temperature and the

acquired spectra are shown in Fig. 5.11. PL spectra were detected in shorter wavelength region while no additional yellow band associated with defect generation was detected. An insignificant improvement in PL intensity was perceived by the porous p-GaN film obtained by PEC etching at 40 mA. A considerable enhancement in the PL intensity was however obtained by the films etched at 60 mA and 80 mA. This might be due to an increase in light scattering off the pore networks in both the films as a result of the formation of a higher density of pores and/or pores with larger dimension in the films comparing to the film obtained by PEC etching at lower AC current of 40 mA. Moreover, a comparison between both the films also signified that the removal of dark pores with larger dimension initially present in the 60 mA etched porous film ((Fig. 5.10 (c)) after PEC etching at 80 mA has contributed to a decrease in the PL intensity. In addition, the stains originating from residues that partially covered the underneath porous GaN layer obtained by etching at 80 mA ((Fig. 5.10 (d)) could also play a part in this detrimental effect [93] This detrimental effect could be explained based on destructive interference effect, wherein a portion of light propagating through the pores was having difficulty in transmitting through the stains [93]. By further increasing the AC current to 100 mA, the formation of microcracks on surface of the porous p-GaN film would have degraded the optical properties of this film, wherein the lowest PL intensity was attained.

Laser processing has the advantages of not bringing severe damage or contamination, as well as of special selectivity with high resolution and high efficiency; however, there were few reports on the laser processing of III-nitrides crystals. High quality nanostructured GaN layers have been successfully fabricated by electrochemical and laser-induced etching processes based on n-type GaN thin films grown on the Si(111) substrate via PAMBE [72]. The sample was then placed in an electrolyte solution with ethanol 99.999%: HF 40%, all in a ratio of 5:1 applied with

a current density of $75\text{mA}/\text{cm}^2$ for the electrochemical etching process. In the laser-induced etching, a power density of $38\text{ W}/\text{cm}^2$ from a laser diode ($\lambda = 635\text{ nm}$, 1.90 eV) was applied. All the etching duration was 45 min at room temperature. The effects of varying current density on morphology of the GaN layer was observed. Electrochemical etching has resulted in the formation of pores over structures with different sizes. The etched surface became hexagonal, and pores over structures were confined to smaller size. In addition, the pore walls were very thin with some short thin tips at the top, as shown in Fig. 5.12 (b) [72].

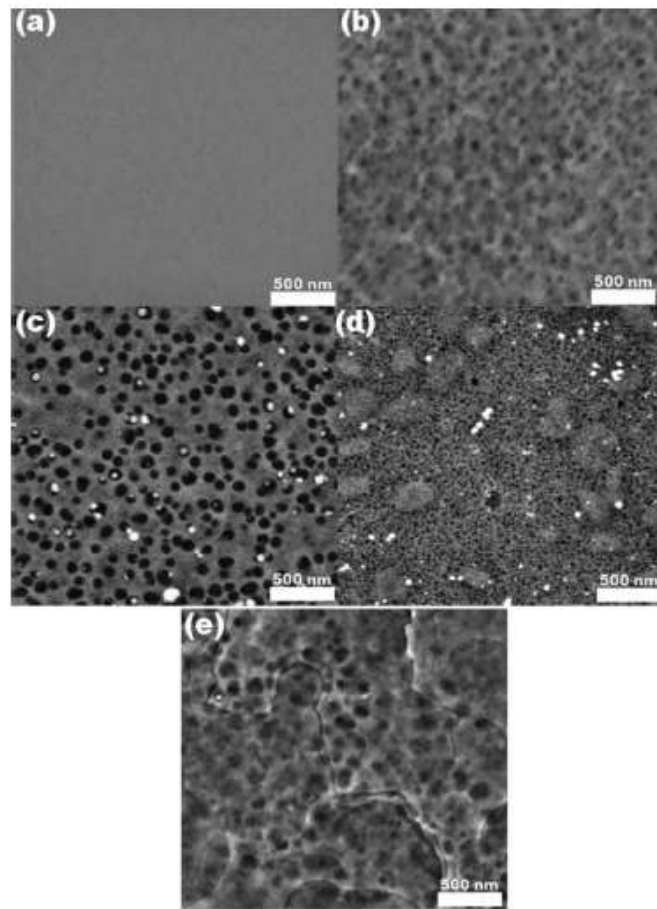


Fig. 5.10 FESEM images of (a) non-porous and porous p-GaN samples obtained by etching in (b) 40 mA, (c) 60 mA, (d) 80 mA, and (e) 100 mA [87].

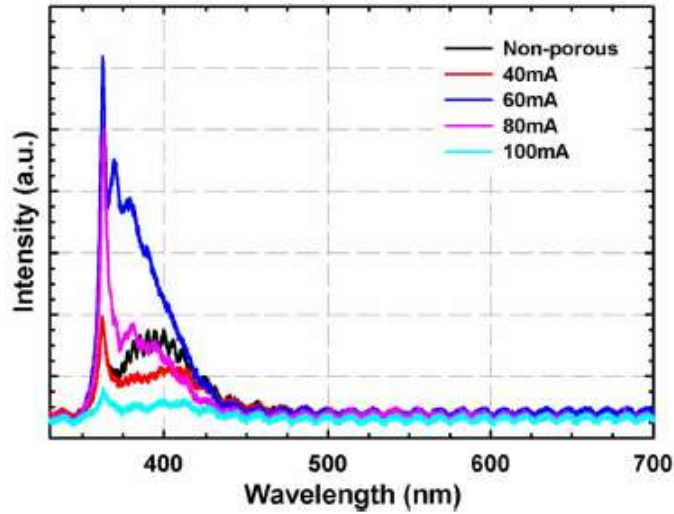


Fig. 5.11 PL spectra determined for non-porous and porous p-GaN samples [87].

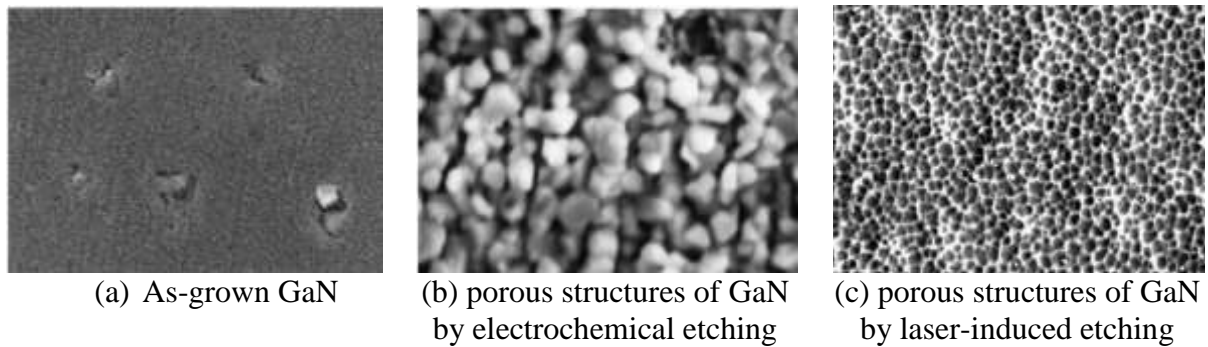


Fig. 5.12 FESEM images of the porous structures of GaN prepared by electrochemical etching and laser-induced etching [72].

When the etch rate of electrochemical etching was too large, the grain boundaries were etched significantly slower than the centre of the crystals. This has led to the attainment of a hexagonal-like and rough morphology. On the other hand, deep and extremely tiny pores were observed in the samples subjected to laser-induced etching (Fig. 5.12 (c)) [72]. This acquisition was believed to be caused by a variation in the penetration depth of the laser beam. Fig. 5.13 depicts the PL spectra obtained for the investigated samples. A blue shift luminescence was obtained in the etched samples relative to the as-grown sample. It was observed that the band

edge emission wavelength was shifted from 362.0 to 335.0 nm for the electrochemically etched sample, and to 346.5 nm for the laser-induced etched sample. The blue shift luminescence could be attributed to charge carrier quantum confinement, which meant that the particles have been confined into a lower dimension and the probability of recombination of electrons and holes would become higher [94]. Effective mass theory has been employed to estimate from the PL data that the average diameter of the GaN crystallites was about 7–10 nm.

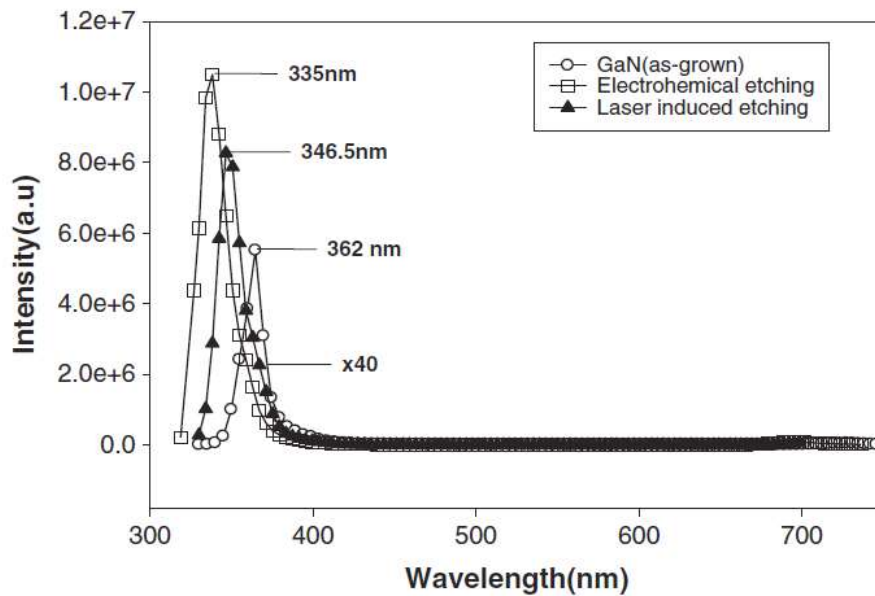


Fig. 5.13 PL spectra of as grown and nanostructured GaN [72].

6. Optoelectronic and Electronic Devices

In recent years, UV photodetection has drawn a great deal of attention. A greater demand for UV instrumentation has been achieved both in civil and military industries for applications, such as engine control, solar UV monitoring, source calibration, UV astronomy, flame sensors, detection of missile plumes, and secure space-to-space communications. The wide band gap semiconductors have been the materials of choice for use in the fabrication of high responsivity and visible-blind UV detectors, owing to the high saturation electron drift velocity, high stability,

and direct band gap offered. Among various kinds of photodetectors, a keen interest was developed in the form of metal-semiconductor-metal (MSM) structure due to its fabrication simplicity, low dark currents, small capacitance, large active area for photodetection, fast response, large bandwidth, low noise, and suitability for monolithic integration of optical receiver. Basically, the structure of a MSM photodetector was consisted of two interdigitated nickel (Ni) Schottky contact (electrode) with four fingers at each electrode, as shown in the schematic diagram presented in Fig. 6.1.

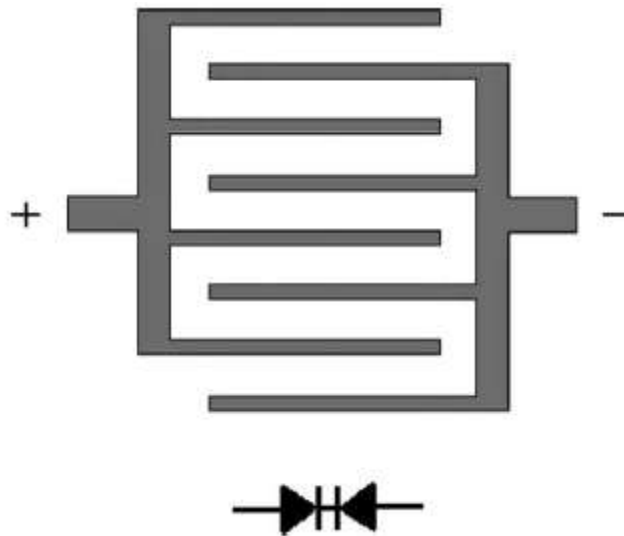


Fig. 6.1 Schematic diagram showing structure of a MSM photodiode [95].

In order to produce an UV photodetector with a high signal-to-noise ratio, it is crucial to achieve a low dark current condition in the fabrication process [96]. In this work, amorphous and microcrystalline GaN films grown on Si(100) at 200°C and 600°C, respectively via the ECR plasma-assisted MOCVD have been studied for the fabrication of MSM UV photodiode [95, 97]. Fig. 6.2 shows a comparison between the I-V characteristics of the amorphous GaN photodiode and microcrystalline GaN photodiode [95] measured under (a) dark and (b) illumination

conditions (photocurrent). A minute fluctuation in the dark current, nearly constant with the applied bias was obtained for the amorphous GaN photodiode. The corresponding magnitude was about 0.18 mA at 10 V, which was much smaller than that measured for the microcrystalline GaN photodiode, which showed a magnitude of about 18 mA at 10 V. This behaviour was most probably due to the resistive nature of amorphous GaN under dark condition as a result of a limited carrier mobility and the existence of localized states in the band gap usually found in amorphous semiconductors due to imperfect bonding configurations [98]. The current conduction under dark condition of the amorphous GaN photodiode might therefore be caused by thermally assisted hopping process between the localized states located near to the conduction band mobility edge, which would usually occurred in low conductivity amorphous semiconductors under moderate temperatures [99].

Under illumination, conductivity of the amorphous GaN photodiode increased drastically (white light photoresponse). Under white light illumination, the change in the resistivity would allow electrical conduction to occur at a normal behaviour, which was caused by significant de-trapping of the localized states as a consequence of strong interaction of the visible and IR components with the deep traps present in the band gap. However, the saturation current started to break down (reverse breakdown) after exceeding 4.3 V for the bias voltage ((inset of Fig. 6.2 (i)). The attainment of low reverse breakdown voltage, explaining the sharp increase of photocurrent for the amorphous GaN photodiode after 4.3 V might be due to high density of localized states present near the conduction band mobility edge, which might have significantly enhanced the photocurrent via a tunneling process [100].

On the other hand, a lack of saturation was observed in the dark current and photocurrent characteristics for the microcrystalline GaN photodiode. It could be observed from the I-V

curves shown in Fig. 6.2 (ii) for a gradual increase in the dark current with respect to the applied reverse bias but no saturation effect was demonstrated. The absence of saturation phenomenon could be explained in terms of the barrier lowering effect or the dependence of barrier height on the electric field strength in the barrier caused by the existence of an interfacial layer between the metal and the semiconductor [97].

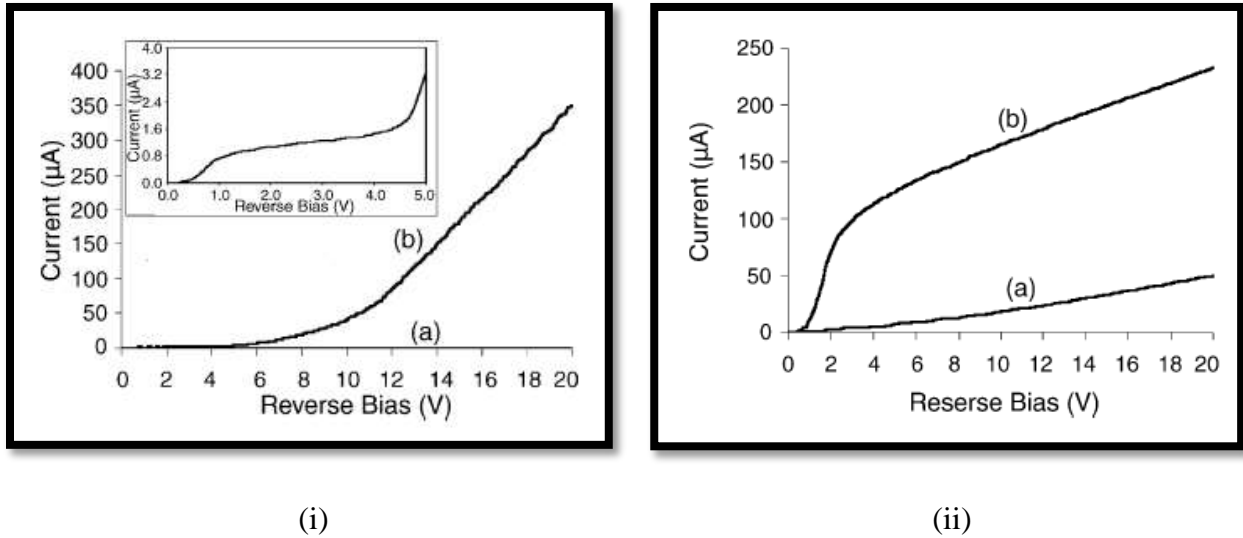


Fig. 6.2 I-V characteristics of MSM photodiodes under (a) dark and (b) illumination conditions for (i) amorphous GaN film and (ii) microcrystalline GaN film grown on Si(100) at 200°C and 600°C [97].

Further analysis was carried out by analyzing the I–V characteristic shown by the dark current condition (Fig. 6.2 (ii)(a)). Fig. 6.3 (a) presents the plot of $\ln[I \exp (eV/kT)]$ versus V with the slope of e/nkT and y-intercept at $\ln I_0$, where I is the actual current, I_0 is the saturation current, V is the bias voltage, n is the ideality factor, and T is the temperature. The ideality factor was determined as 1.005, which was nearer to unity or small departure from unity, indicating good quality of the Schottky contact in the MSM structure as well as the presence of a thin interfacial layer between the Ni and microcrystalline GaN. In this case, the existence of interfacial layer could not be ruled out, except that the microcrystalline GaN was cleaved in an

UHV condition. The plot of $1/C^2$ versus V in Fig. 6.3 (b) denotes a relationship between the capacitance, C and bias voltage, V according to the equation of $C^{-2} = (2/A^2qN_D\epsilon_S)(\phi_b - \xi - V - kT/q)$, by assuming that the interfacial layer was absent; the diode was nearly ideal; the semiconductor has a uniform donor concentration. The values of barrier height (ϕ_b) for Ni/microcrystalline GaN and donor density (N_D) of the semiconductor could be determined respectively from the slope ($2/A^2qN_D\epsilon_S$) and x-axis interception ($V_I = \phi_b - (kT/q) - \xi$) of the plot [95].

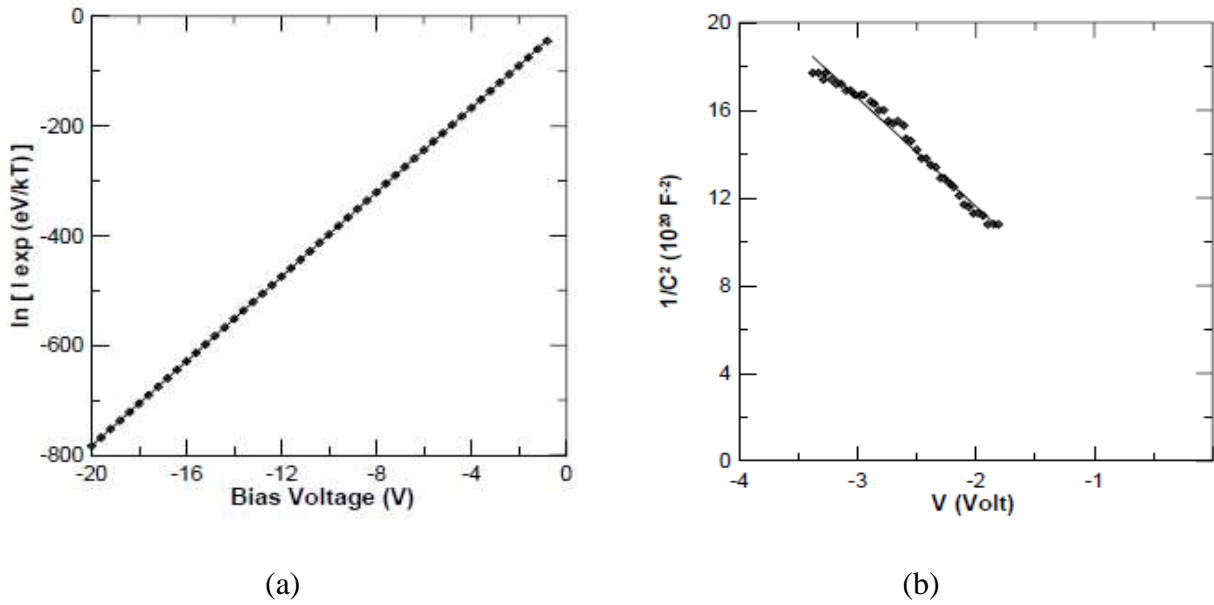


Fig. 6.3 (a) The plot of $\ln[I \exp(eV/kT)]$ vs. bias voltage (V) and (b) The plot of $1/C^2$ vs. V for microcrystalline GaN/Si(100) MSM photodiode [95].

The calculated N_D was $1.479 \times 10^{13} \text{ cm}^{-3}$ and Φ_b was 0.734 eV. This finding signified that a lower Schottky barrier height was obtained for the Ni/microcrystalline GaN grown on Si(100) as compared to the reported values in the literatures for GaN films grown on Al_2O_3 substrates [101-102]. The variation in barrier height values might be due to the formation of Ga_4Ni_3 , the different thickness of interfacial layer that might have formed, a variation in surface roughness of the different layers, and defects formation in the microcrystalline GaN films as well as the presence of several transport mechanism [103-104].

Literature reported that the high thermal stability of GaN would prompt an improvement in electrical characteristics of the UV photodetector with respect to temperature. A similar study was carried out in this work via AlGaN heterostructures-based MSM UV photodetector, in which thermal annealing was deemed to be a useful method to reduce the dark current in the photodetector [34, 97]. Good I-V characteristics (dark and photo current), spectral responsivity, and photoconductivity behavior [34] were demonstrated by the photodetector, as shown in Fig. 6.4.

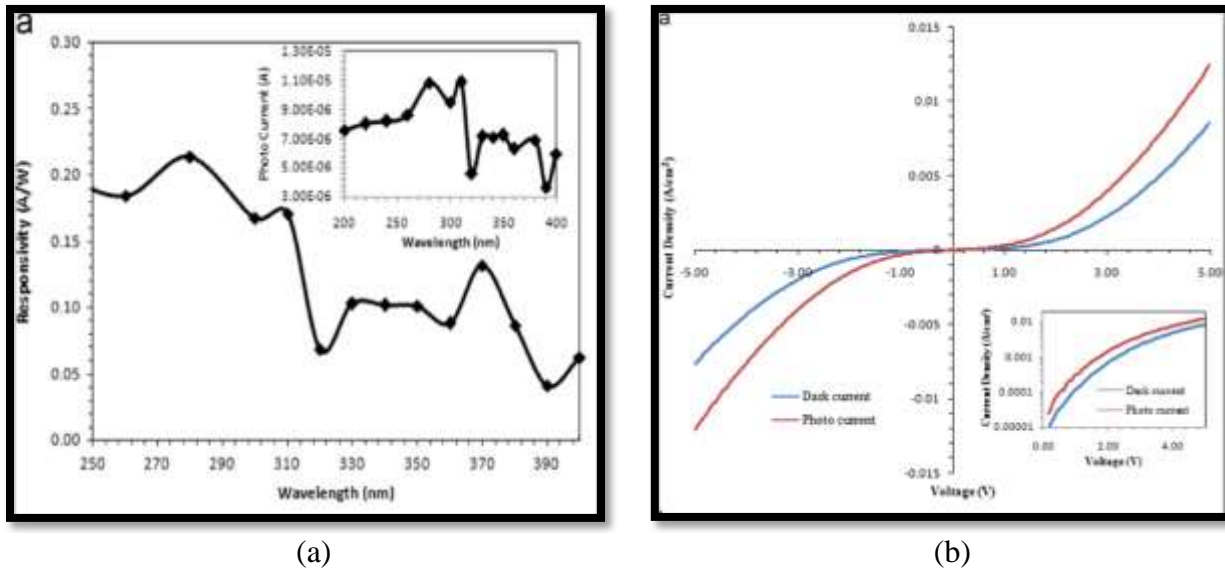


Fig. 6.4 (a) The spectra responsivity and photo conductivity (inset) (b) I-V characteristics of AlGaN MSM UV photodetector [34].

In another study, porous InGaN structure produced via UV-assisted PEC etching was used to fabricate the MSM photodetector for investigation [77, 105]. The photoelectric behavior of the fabricated photodetectors was investigated using chopped light of wavelength 390 nm with an intensity of 0.43 mW/cm^2 at a bias voltage of 0.5 V. The time-dependence photocurrent characteristic of the detector is shown in Fig. 6.5 (a).

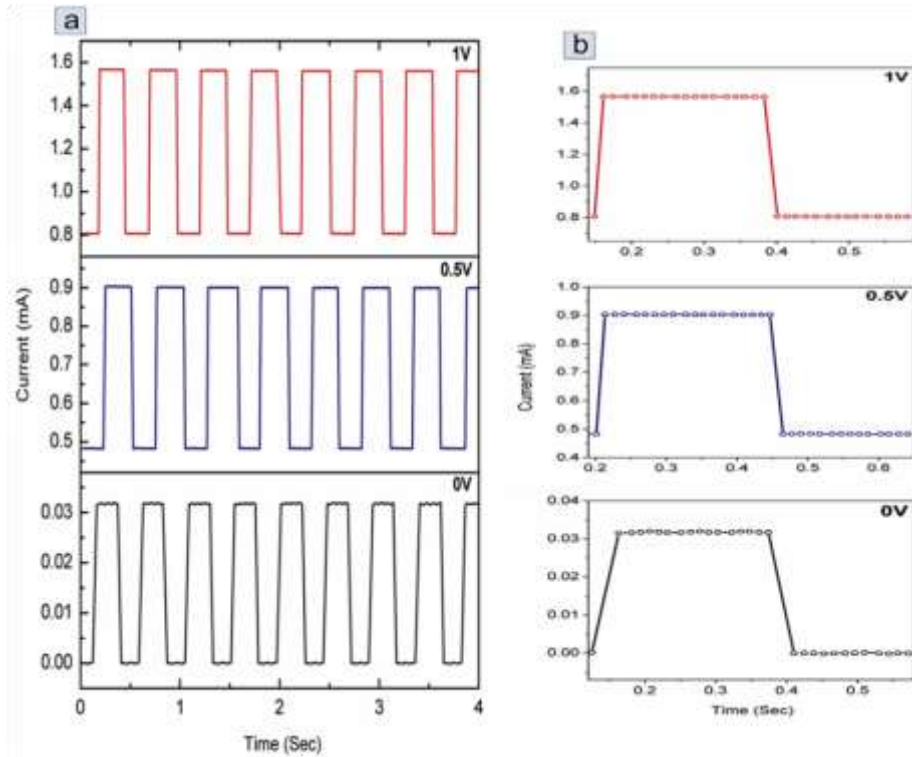


Fig. 6.5 Photoreponse of the fabricated device at various applied biases [77].

Good repeatability was observed for the photodetector. In addition, a photovoltaic behavior was observed at 0 V, in which the photons of the incident light were sufficient to generate an electric field, which has in turn produced a photocurrent. The saturation current was determined to be 0.032 mA under a light intensity of 10 mWcm^{-2} . As the bias voltage was increased to 0.5 V and 1 V, the electric field produced a photocurrent that was added to the bias current. Therefore, an increase in the saturation current from 0.9 mA to 1.57 mA with the increase of bias voltage from 0.5 V to 1 V. Fig. 6.5 (b) shows one complete cycle of the photoreponse, in which the rise time was noted to be shorter than the recovery time regardless of the bias voltage. Under a bias voltage of 0.5 V for instance, the rise time was faster (12 ms) than the recovery time (13 ms). In summary, the fabricated porous InGaN-based MSM

photodetector has demonstrated a photovoltaic behavior with a responsivity that would increase with the increase of applied voltage [77].

Solar cell manufacturing was also attempted in the present work by using a quaternary n-type $\text{Al}_{0.08}\text{In}_{0.08}\text{Ga}_{0.84}\text{N}$ surface layer coated on a p-type Si [106]. Outcome of this work turned out to be feasible, in which the system has successfully yielded a solar cell efficiency of 9.74 % as compared to other anti-reflection coating (ARC) systems. This observation was attributed to a reduction in optical losses and recombination losses on the surfaces, and thus resulting in an enhancement in the efficiency. Moreover, the unique piezoelectric effect brought by III-nitrides could have assisted in reducing the recombination rate, as well as in generating a well and barrier structure, which would therefore improve the optical confinement state [106].

Furthermore, GaN-based metal-oxide-semiconductor (MOS) devices have been also fabricated and characterized [96]. The GaN films were initially grown on Si(100) substrates by ECR plasma-assisted MOCVD before subjected to oxide layer deposition using a spin-on SiO_2 glass. After the SiO_2 film deposition, post-annealing was carried out at 200°C for 1h. A layer of Al metal contact was then deposited on the SiO_2 film serving as a dielectric layer, as well as on the back side of Si substrate to serve as an ohmic contact via vacuum evaporation. The fabricated MOS structure was characterized using capacitance–voltage (C–V) with computer aided measurement system (Keithly Instrument with ICS Software). It was conveniently revealed from the C–V curves in Fig. 6.6 that a lower threshold voltage (V_{th}) (1.72 V) and flat band voltage (V_{fb}) (0.65 V) have been perceived by the sample annealed at higher temperature (600°C) in contrast to the sample annealed at 200°C (4.95 V for V_{th} and 4.01 V for V_{fb}) [96].

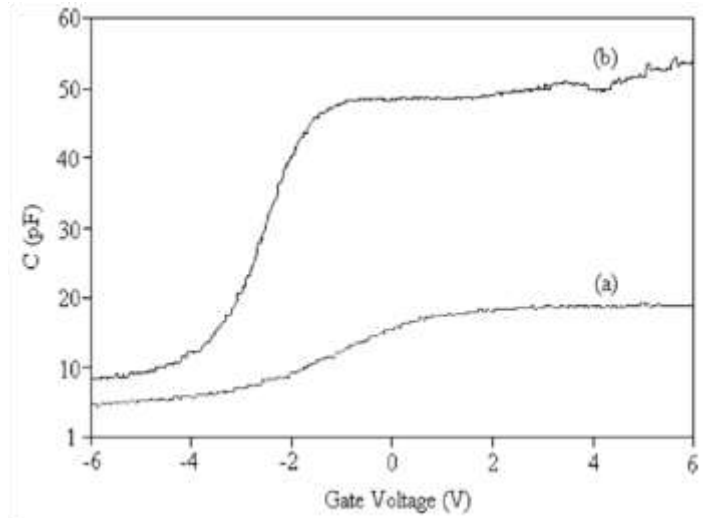


Fig. 6.6 Capacitance–voltage (C-V) characteristics of the fabricated GaN-based MOS structures annealed at (a) 200°C and (b) 600°C [96].

Recently, hydrogen has been gaining attention as the most promising clean, renewable, and common fuel to replace carbon-based fuels in the future as to overcome some of the critical problems related to a depletion of fossil fuel resources, air pollution, and global warming [107-108]. Although hydrogen is less dangerous as compared to other combustible gases, its invisibility, odorless, and tasteless characteristics might impose certain risks to human beings, owing to the high heat of combustion and low ignition temperature within the wide flammable range of 4%-75%. Besides, the smallest hydrogen molecule has high diffusion coefficient in air, and thus any leakage in all stages of usage, such as storage and fuel cell in transportation may bring explosion. Moreover, hydrogen will cause corrosion at elevated temperature [109]. The hydrogen atoms will penetrate into the metals and subsequently exasperate the metals internally, which will affect the properties of metals in terms of strength, durability, and fracture toughness.

In order to prevent the risk of a fatal accident due to hydrogen leakage as well as to get rid of corrosion issues, it is necessary to develop a safety monitoring system for detecting the hydrogen level using affordable and compact hydrogen sensors that can withstand high

temperature. Among the wide band gap semiconductors, GaN-based materials have been recognized as the viable materials used for gas sensor devices that operate in harsh environmental conditions, such as high-temperature and chemically corrosive ambient. In addition, the small Fermi level pinning characteristics of III-nitrides are also important features that may lead to high gas sensor sensitivity [110]. Besides that, III-nitrides metal-semiconductor-based (MS) sensors are more economic as compared to other materials due to the simple processing steps involved. For these reasons, III-nitrides semiconductor materials have attracted much attention in the field of gas sensing application.

Fig. 6.7 (a) shows a simple set up of gas sensing system in the laboratory. In the present work, the III-nitrides-based gas sensor was tested in a homemade gas chamber channeled with different concentrations of hydrogen at room temperature. Pt/GaN on sapphire was successfully fabricated and the results showed that the GaN-based material system appeared to be very promising for use in hydrogen gas detection. The structure of GaN hydrogen sensor is clearly shown in Fig. 6.7 (b) [111].

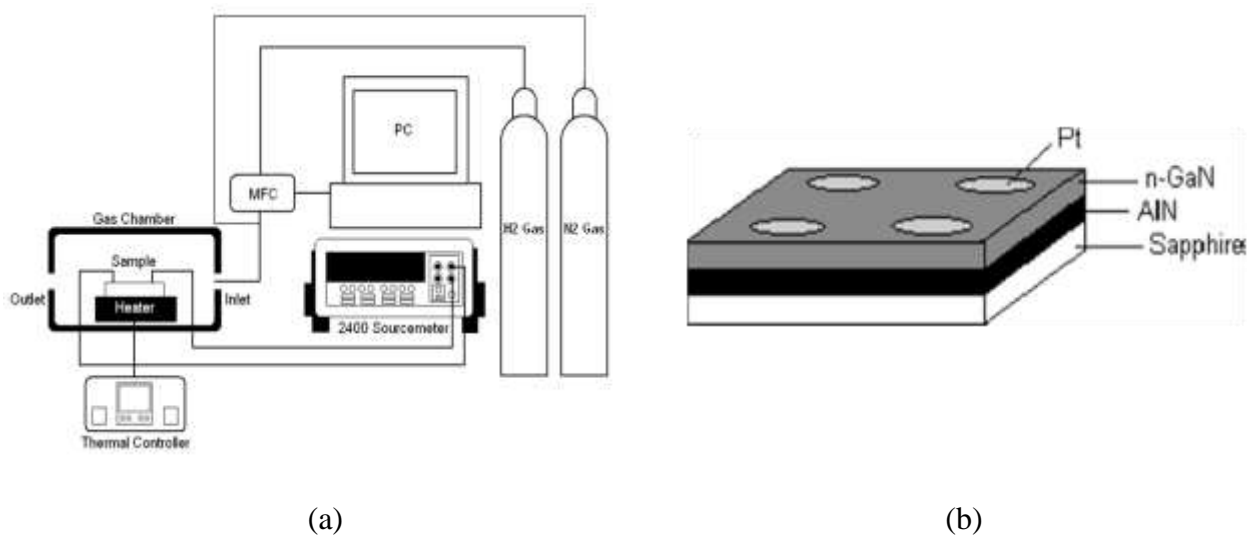


Fig. 6.7 (a) Simple set up of gas sensing system and (b) structure of the Pt/n-GaN gas sensor [111].

Nanostructured wide bandgap semiconductors for gas sensing have brought numerous advantageous properties, including the ability to operate at high temperatures (or, alternatively, to have low leakage current at room temperature), radiation and environmental stability, and mechanical robustness. In addition, electrical, optical, and chemical properties of the nanostructures can be tuned by changing the size of the particles. Particularly, the high surface to volume ratios of nanostructures would generally enhance the sensor response as well as increasing catalytic activity or adsorption over the surface of the nanostructures. To date, hydrogen sensors fabricated using nanostructured GaN have been investigated [38-40].

The GaN NWs-based hydrogen sensor was operated at different temperatures and constant applied voltage (1 V) during the gas sensing measurements. Fig. 6.8 presents the sensor response with respect to hydrogen concentration. It was worth noting that the sensor response was increased from 17 to 65 % at 7 ppm and from 127 to 150 % at 100 ppm when the working temperature was increased to 75°C. The GaN NWs-based gas sensor has exhibited good sensing performance for the ability to detect ultra low (ppm) concentration of H₂ gas at low operation temperature, as well as fast response/recovery speed, suggesting the potential use of III-nitrides materials for gas sensing applications [40].

High quality hydrogen sensors based on porous GaN [112] and porous InAlGaN [82] were successfully fabricated. The porous GaN samples were synthesized by electrochemical etching technique. To fabricate the gas sensor, Pt Schottky contact with thickness of 200 nm was deposited onto the GaN film using RF sputtering system. A metal mask consisting of an array of holes with a diameter of about 0.9 mm was used for this purpose. SEM image of the fabricated gas sensor with Pt contact is shown in Fig. 6.9 [112].

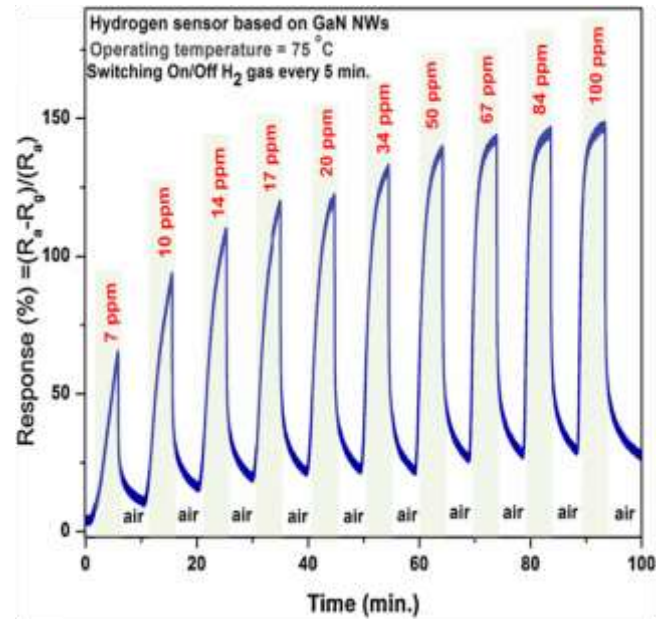


Fig. 6.8 Changes in the response of GaN NWs gas sensor upon exposure to ultra low concentrations (7–100 ppm) of H₂ gas at 75°C. The NWs based sensor was annealed under 100 sccm flow rate of NH₃ gas [40].

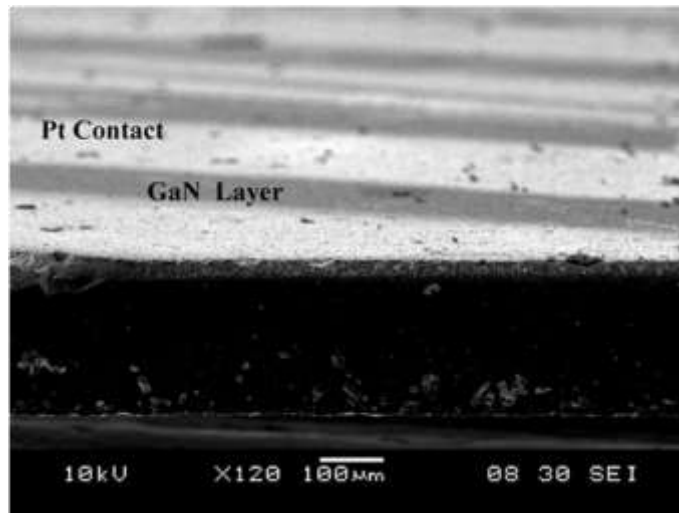


Fig. 6.9 FESEM image of the fabricated gas sensor with Pt contact [112].

Fig. 6.10 illustrates the on–off responses of the sensor measured at room temperature at a constant voltage of 1V. The response and recovery time measured for the sensor are about 3 and 2.5 min, respectively. The sensor showed a good sensitivity as a function of time with the

minimum flow rate of 1 sccm for the test gas (H_2), indicating a good sensor performance. The maximum sensitivity was attained in more than 10 and 20 min (shut off-time) after cutting off the hydrogen gas and this might accrue due to the trapping of hydrogen atoms from the defects at the Pt/porous GaN (Pt/PGaN) interface and these atoms would then diffuse through the Pt thin film, moving towards the Pt/PGaN contact interface. As a result, polarization took place, forming a dipole layer near the interface.

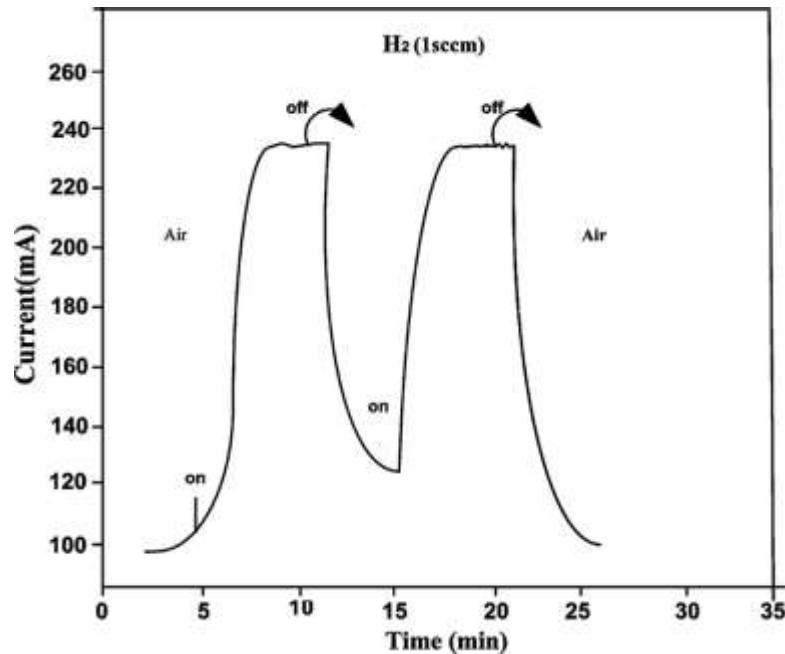


Fig. 6.10 Room temperature on-off responses of hydrogen gas sensors measured at constant voltage of 1V [112].

The hydrogen gas sensing ability has been also demonstrated by the porous InAlGa_N films produced using UV-assisted PEC etching technique [82]. Fig. 6.11 shows the I-V characteristic of the non-porous and porous InAlGa_N samples subjected to different etching durations for the detection of 0.1% H_2 in N_2 gas at room temperature. All the samples exhibited Schottky characteristics. In general, an increase in the current of all samples was observed in the initial stage of introducing 0.1% H_2 in N_2 gas to the chamber. As the etching duration was

increased from 1 to 5 min and subsequently to 10 min, changes in the current was observed. This result indicated that the porous structures have played an important role in enhancing the sensor response, in which the porous samples with high pore density were more sensitive to the hydrogen detection. This phenomenon was related to the increase in surface area to volume ratio for the porous structures, which might allow more interaction between the sample surface and the hydrogen gas [82].

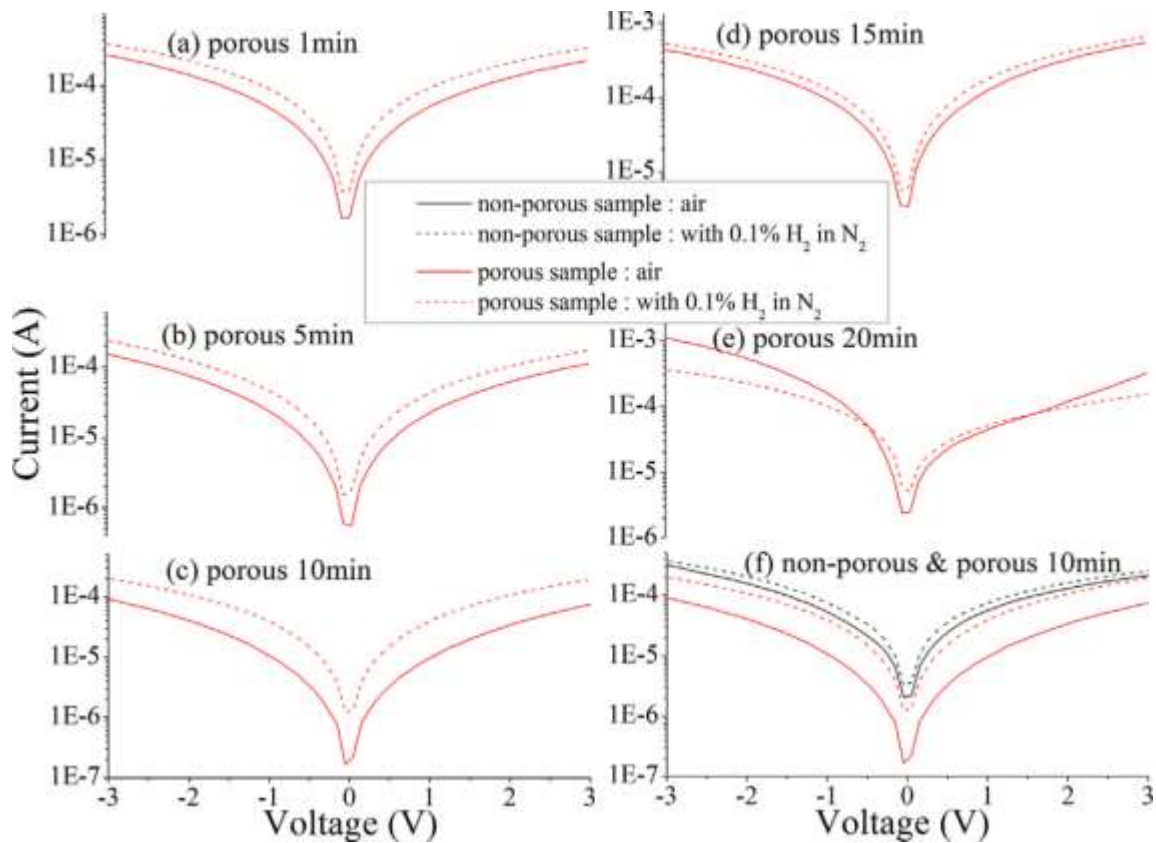


Fig. 6.11 I–V characteristics of porous InAlGaN gas sensors at different etching durations: (a) 1 min, (b) 5 min, (c) 10 min, (d) 15 min, (e) 20 min when operated in ambient air and with 0.1% H_2 in N_2 gas at room temperature. (f) shows the I–V characteristics of the non-porous and 10 min etched porous InAlGaN gas sensors [82].

Apart from the hydrogen gas sensors fabricated using III-nitrides materials, other wide band gap semiconductors, such as zinc oxide (ZnO) could be also synthesized on the III-nitrides

films to form heterostructures for use in gas sensing application. In this work, high quality ZnO hexagonal tube-like nanostructures grown on p-type GaN heterojunction have been synthesized for sensing applications through a low-cost catalyst-free process by thermal evaporation at 800°C. Fig. 6.12 (a) reveals that the “blanket thickness” for as-grown GaN substrate before the deposition of ZnO was 0.6 μm while Fig. 6.12 (b) denotes that the “blanket thickness” for ZnO nanostructures grown on the p-type GaN substrate was thicker (around 1.5 μm) with approximately 1 μm thick for the length of the tube, as shown in Fig. 6.12 (c).

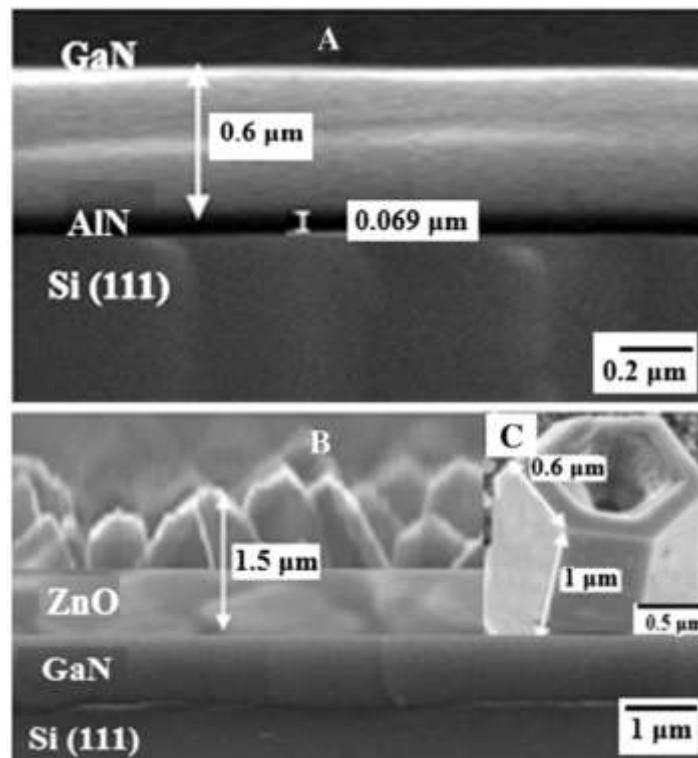


Fig. 6.12 FESEM cross-section images (A) for p-GaN substrate before deposited, and (B) for ZnO hexagonal tube-like nanostructures grown on a p-GaN substrate [113].

The dynamic response of the sensor based on ZnO hexagonal tube-like nanostructures on p-GaN subjected to different H₂ flow rates at room temperature is shown in Fig. 6.13. It was expected from this study that the proposed process could also be readily utilized in the

development of other types of one-dimensional semiconductor nano materials-based chemical and optoelectronic sensors.

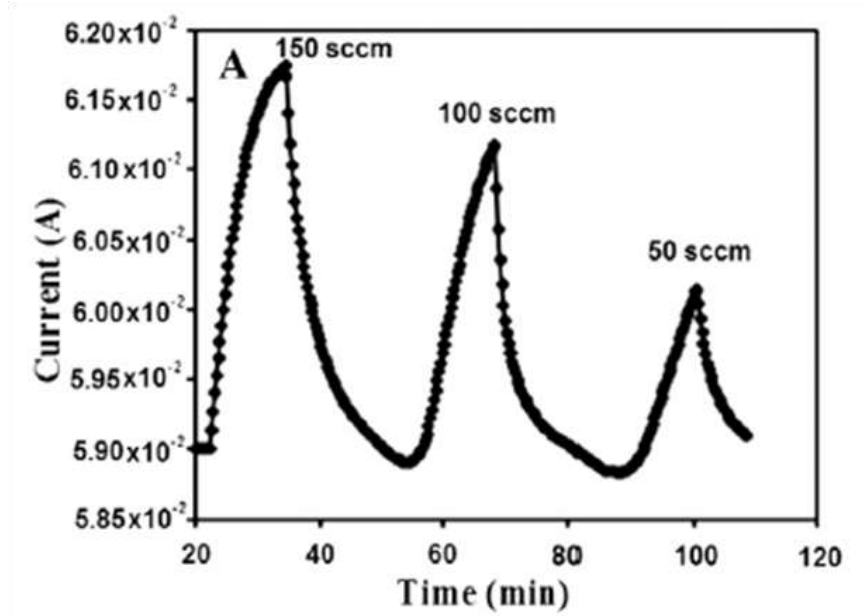


Fig. 6.13 The on–off currents of ZnO gas sensors operating at room temperature for a constant voltage of 1 V exposed to different hydrogen flow rates [113].

On top of the hydrogen gas sensing studies, additional study was also carried out on AlGaIn-based MSM structure with Ni Schottky contacts to investigate the sensing behaviors of hydrostatic pressure [114]. The MSM structure was consisted of two interdigitated Schottky contacts (electrodes). The finger width was $230 \mu\text{m}$ and the finger spacing was $400 \mu\text{m}$. The length of each electrode was about 3.3 mm and was consisted of 4 fingers. Ni was used as the Schottky contact metal and was deposited by thermal evaporation through a metal mask onto the AlGaIn films. For pressure sensing measurement of the MSM device, hydrostatic pressure was applied through a liquid pressure apparatus from the Polish Academy of Sciences. The hydrostatic pressure was determined from the resistance change of a semiconductor (InSb) pressure gauge located adjacent to the MSM sample in the cell. The I-V characteristics of the

$\text{Al}_{0.24}\text{Ga}_{0.76}\text{N}$ MSM structure are shown in Fig. 6.14 (a) for zero pressure and for 3.73 kbar of hydrostatic pressure. The current at fixed bias was found to decrease as a function of applied pressure, as evidenced in Fig. 6.14 (b). The observed change in current was reproducible through several runs within the linear range.

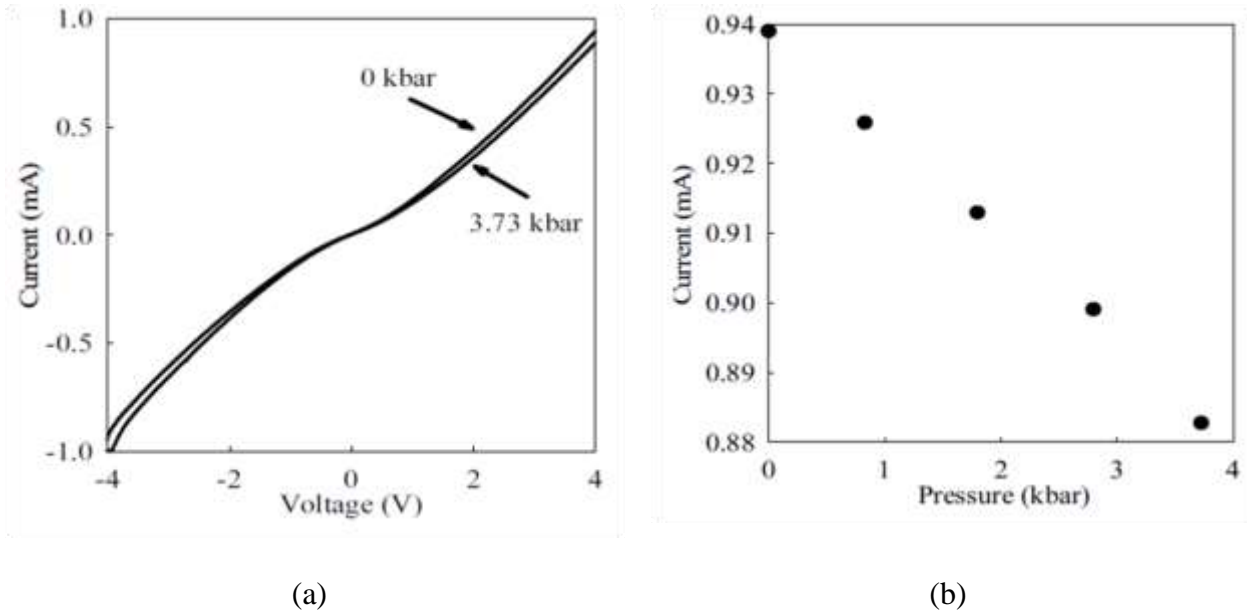


Fig. 6.14 (a) I-V characteristics measured under zero and 3.73 kbar pressure and (b) pressure dependence of current for the AlGaIn MSM structure [114].

Keeping pace with the advancement in GaN-based technology nowadays for power electronics and other optoelectronics applications, LEDs have been progressively penetrating the lighting technology to substitute the conventional energy inefficient incandescent lamps by offering low energy consumption, high luminosity, and long lifetime. In the fabrication of a functional LED giving emission of different colors, which can be red, green, blue, and white, the band gap energy of the semiconductor materials has significant contribution in determining the colour emission (wavelength). Since 1990s, GaN-based materials have been commonly utilized in the manufacturing of bright LEDs. In recent times, the GaN market has been mostly driven by the blue laser diode production and related applications, such as high-density data storage. The

market has been strongly boosted by blue ray players and game stations, which are currently in a strong demand. Fig. 6.15 shows a strong blue emission produced by GaN pn-homojunction structures in this work.

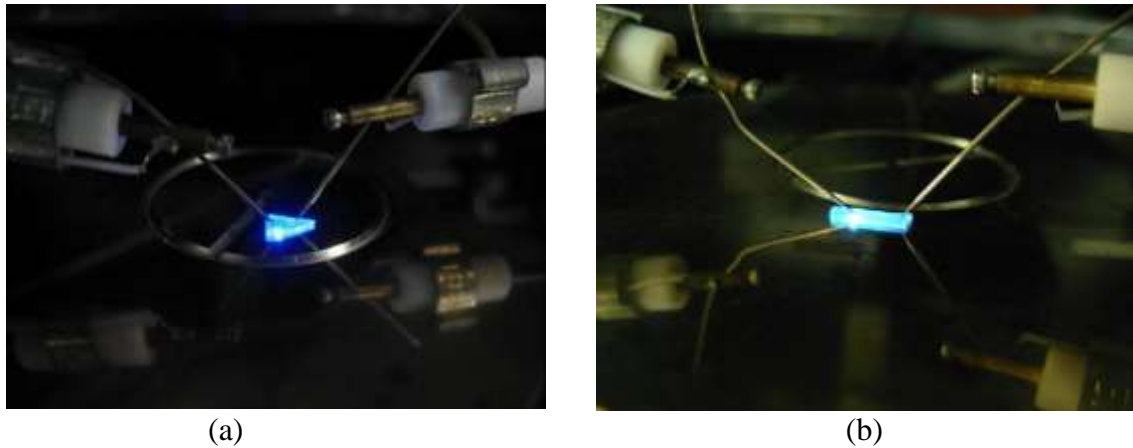


Fig. 6.15 Strong blue emission produced by GaN pn-homojunction structures processed by (a) dry etching using reactive ion etching (RIE)-inductively coupled plasma (ICP), and (b) RIE-ICP followed by wet chemical etching.

A collaboration project was also carried out to fabricate a LED structure from the InGaN multi-quantum well (MQW) grown using MOCVD system [115]. HRXRD rocking curves revealed that the $n\text{-Al}_{0.06}\text{Ga}_{0.94}\text{N}/n\text{-GaN}$ strained-layer superlattices (SLS) under-layer has facilitated in improving crystalline quality of the LED structures by reducing the threading dislocation density (TDD). Reciprocal space mapping (RSM) confirmed the strain state of the GaN epitaxial layers. Triple axis (TA) XRD omega-2Theta (ω - 2θ) scan in Fig. 6.16 reveals the presence of higher order fringes, indicating the formation of a sharp layer interface between the main and MQW layers. PL measurement of the sample with $n\text{-Al}_{0.06}\text{Ga}_{0.94}\text{N}/n\text{-GaN}$ SLS under-layer showed the acquisition of band-to-band photon energy of 2.97 eV with a narrower FWHM as compared to the sample with $n\text{-Al}_{0.03}\text{Ga}_{0.97}\text{N}$ under-layer (Fig. 6.17).

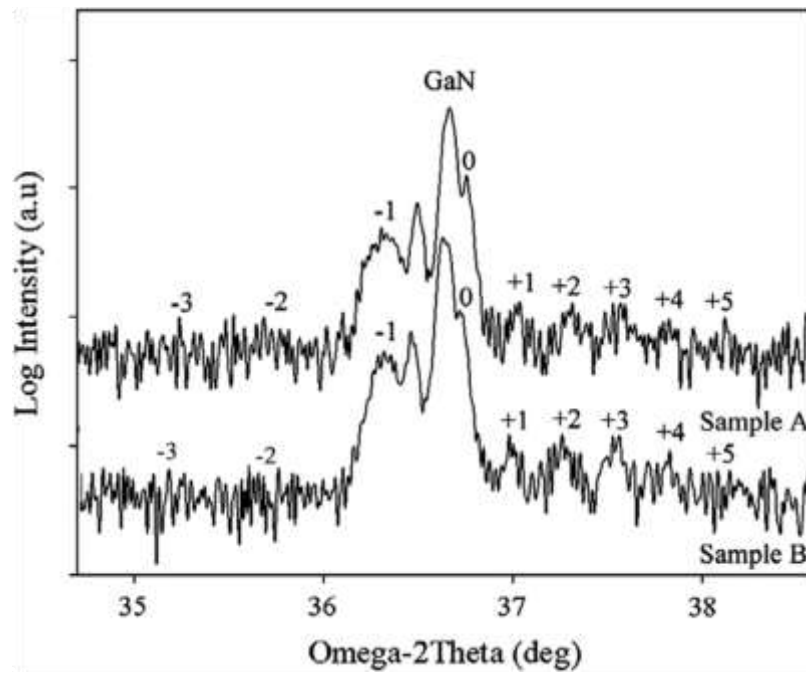


Fig. 6.16 Triple axis XRC ω - 2θ spectrum of $\text{In}_{0.11}\text{Ga}_{0.89}\text{N}/\text{In}_{0.02}\text{Ga}_{0.98}\text{N}$ MQW LED structure of Sample A and B with $n\text{-Al}_{0.06}\text{Ga}_{0.94}\text{N}/n\text{-GaN}$ SLS and $n\text{-Al}_{0.03}\text{Ga}_{0.97}\text{N}$ under-layer, respectively [115].

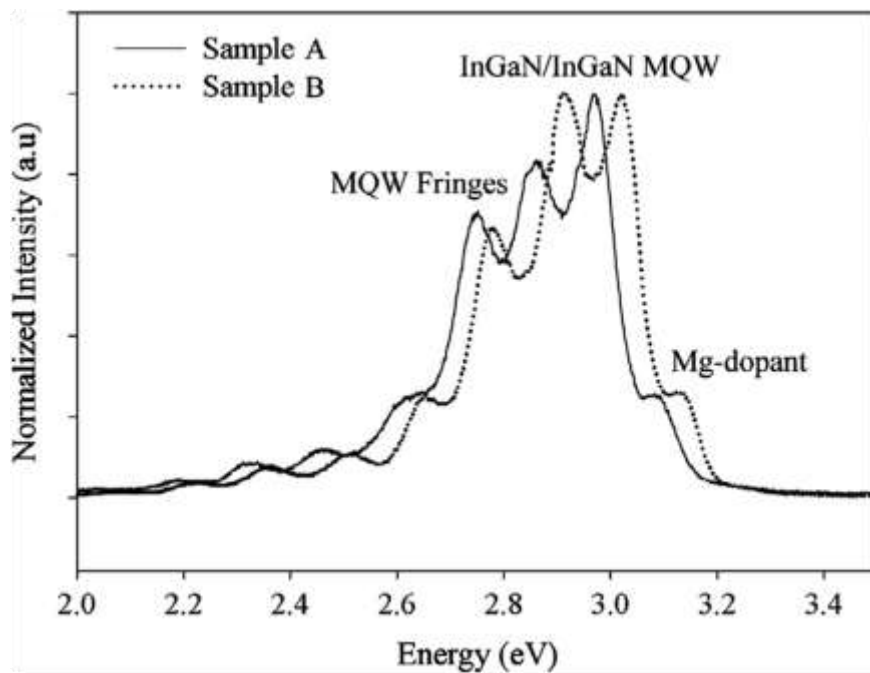


Fig. 6.17 PL characteristics of $\text{In}_{0.11}\text{Ga}_{0.89}\text{N}/\text{In}_{0.02}\text{Ga}_{0.98}\text{N}$ MQW LED structure [115].

The development and fabrication of flip-chip GaN based LEDs has prompted the search for high reflectivity metallizations, in addition to stable, ohmic, and low resistivity contact to GaN. Few researchers had reported the use of silver (Ag) or metal/silver as the metal contact to n-GaN but rarely used as the metal contacts to p-GaN [116]. Literatures reported that silver has good electrical resistivity ($1.59 \times 10^{-6} \Omega\text{cm}$) and thermal conductivity ($1 \text{ cal/cm-s-}^\circ\text{C}$) [117]. Moreover, silver can form electrically superior contacts to p-GaN than Ni/Au, and has higher reflectivity than Al [118]. Therefore in this work, an investigation on thermal stability and morphological investigation of Ni/Ag bi-layer contacts on p-GaN with annealing temperatures ranging from 300°C to 800°C was carried out. Cryogenic cooling after heat treatment was also performed to determine the effects of this treatment on the electrical properties of the contacts [119].

Table 6.1 The comparison of Ni/Ag specific contact resistivities at different annealing temperatures and times between annealed (A) and annealed-and-cryogenically treated (A+C) samples [119].

Annealing Temperature ($^\circ\text{C}$)	Specific Contact Resistivities ($\Omega\text{-cm}^2$)					
	Annealing Times/ (cumulated annealing times)					
	10 min		15 min/(25 min)		25 min/(50 min)	
	A	A+C	A	A+C	A	A+C
300	-	-	-	-	7,042	1,450
400	-	-	-	-	5,857	2,475
500	1,254	16,272	4,047	13,185	7,030	12,009
600	0,825	0,773	2,470	0,703	3,411	3,222
700	0,489	0,395	0,354	0,099	0,401	0,251
800	1,389	1,962	2,332	1,193	12,028	0,763

The initial study revealed that all as-deposited (reference sample), 300°C and 400°C annealed or annealed- and-cryogenically treated samples demonstrated Schottky behaviour.

However, under extended annealing time, i.e. 50 min, 300°C (*A* and *A+C*) and 400°C (*A* and *A+C*) samples showed ohmic characteristics and *A+C* treated samples exhibited a better specific contact resistivity (SCR) value than *A* samples for both 300°C and 400°C. From Table 6.1, 700 °C was the optimum annealing temperature for Ni/Ag contact resistivities in this study. All the samples regardless of *A* or *A+C* under annealing durations of 10 or 25 min showed a similar trend, with a high value of SCR at 500°C annealing temperature, then gradually decreased and reached its lowest value at 700°C. The SCR increased tremendously after this optimum temperature. The improvement of SCR from 500°C to 700°C could be related to the increase of the contact areas between the metal scheme and the GaN, since the heat treatment might result in the roughening of the interface due to interfacial reactions.

Besides that, study on transparent conducting oxides (TCOs) as electrodes for optoelectronic devices has also been carried out to enhance the performance of LED [120-121]. Indium tin oxides (ITO) are widely used in optoelectronic applications as transparent conductive electrodes (TCE) for light emitting and light detecting devices such as LED and solar cells. This could be attributed to its unique properties of highly transparent over the visible spectrum (> 80 %), very low resistivity ($\sim 10^{-4}$ Ωcm), high carrier concentration ($\sim 10^{21}$ cm⁻³) with mobility around 10-30 cm²/Vs, wide optical band gap (~ 3.6 -3.9 eV) and high work functions (~ 4.20 eV) [122-124]. ITO thin films can be prepared by electron beam evaporation [125], thermal evaporation [126], pulsed laser deposition [127], DC sputtering [128] and RF sputtering [129]. Among the reported techniques, sputtering technique is the commonly practiced method to deposit the ITO thin films due to the high deposition rates, easy to control, and ability to deposit on a large area of substrates with good thin film quality.

In this work, the TCO characteristics were studied by employing ITO and ITO/metal thin layer as the electrodes for optoelectronics device applications [121]. ITO, ITO/Ag and ITO/Ni were deposited on Si and glass substrates by thermal evaporator and RF magnetron sputtering at room temperature. Post deposition annealing was performed on the samples in air at moderate temperature of 500°C and 600°C. The structural, optical, and electrical properties of the ITO and ITO/metal were then characterized [121].

Recently, high brightness ZnO nanorod/p-GaN UV LED was successfully fabricated in this work [130]. The high-quality, vertically aligned ZnO nanorods were directly grown on a p-type GaN substrate without the presence of interface layer via microwave-assisted chemical bath deposition (MA-CBD), in which a polyvinyl alcohol (PVA)-Zn(OH)₂ nanocomposite was used as the seed layer. CBD is a low temperature and low cost growth method of ZnO nanorods on a GaN substrate. However, this would leave an interface layer between the grown nanorods and the substrate, which might affect the light emission and extraction behaviors of the device. Fig. 6.19 depicts a LED structure fabricated using the MA-CBD grown ZnO nanorods on p-GaN. Prior to the growth of ZnO nanorods on the p-GaN substrate, 5- and 200-nm- thick layers of Ni and ITO were deposited, respectively, by RF-sputtering on the p-GaN substrate, followed by an annealing at 350°C for 1h in a nitrogen ambient. After the growth of ZnO nanorods arrays, poly methyl methacrylate (PMMA), thin layer of SiO₂ (deposited by RF sputtering), and polyvinyl alcohol (PVA) were used as the filling materials to ensure that all the spaces between the nanorods have been entirely filled. This step was essential to prevent a possible occurrence of short circuit between the top contacts (n-type ITO) and the substrate.

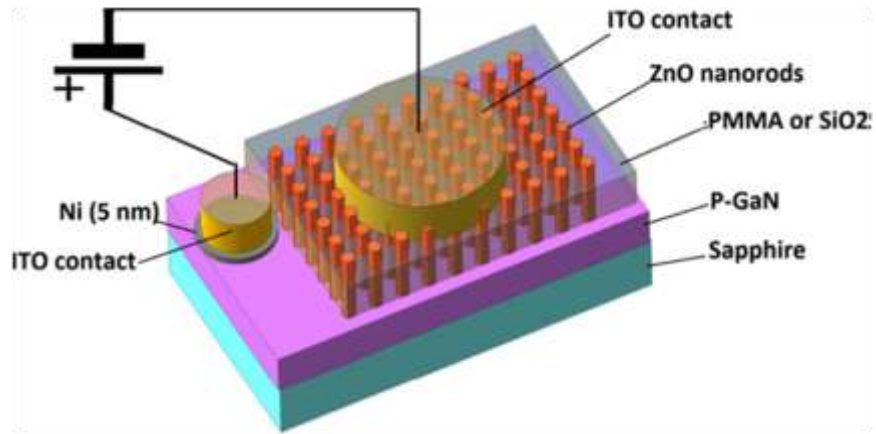
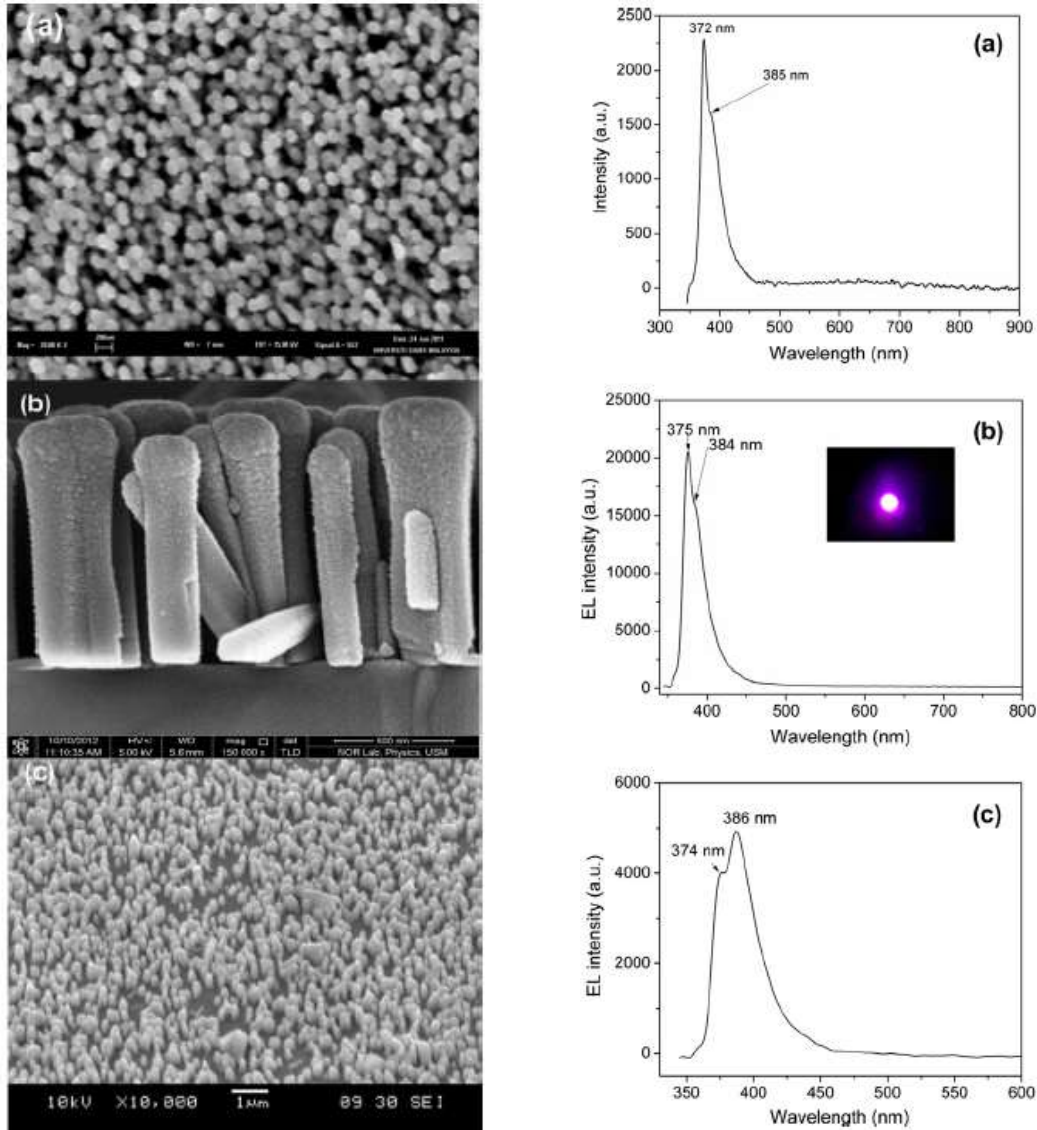


Fig. 6.19 Schematic illustration of fabricated n-type ZnO nanorods/p-type GaN thin film LED [130].

Fig. 6.20 presents the FESEM images and electroluminescence (EL) characteristics of the ZnO nanorod/p-GaN LEDs [130]. It was revealed from the figure for the formation of vertically aligned hexagonal structures in the ZnO nanorods ((Fig. 6.20 (i)). In addition, it could be observed that a high density of the ZnO nanorods was grown on the GaN substrate, suggesting a good homogeneity of the seed layer. The EL spectra were measured in forward and reverse bias at a normal incidence angle to the top surface of the LEDs. When the bias voltage was increased to 45 V with an injection current of 125 mA (Fig. 6.20 (ii) (b)), the EL peak intensity at 372 nm was rapidly increased with a minute red shift to 375 nm. This phenomenon might be due to the high kinetic energy of the electrons and holes that have recombined at the two sides of the heterojunction, leading to a heating of the junction. Besides, it was noted that the EL properties has exhibited EL emission under both forward and reverse bias but was mainly resided in the UV region [130].



(i) FESEM images of a) as-grown ZnO nanorods on p-GaN, (b) cross-section view of sample after RF sputtering of SiO₂ thin film, and (c) 45° view of device after oxygen plasma etching of spin-coated PMMA layer. (ii) EL spectra for LED under: (a) forward bias of 38 V and 105 mA, (b) forward bias of 45 V and 125 mA, and (c) reverse bias of 38 V and 105 mA.

Fig. 6.20 (i) FESEM images of ZnO nanorod on p-GaN (ii) EL spectra of LED [130].

In addition, a novel and low cost "NORLED" (Nano-Rod LED) device, which emits in the UV region was fabricated using ultra long ZnO nanorods that were grown on the p-GaN substrate by a direct heat substrate-modified chemical bath deposition (DHS-MCBD) growth

process. Thus far, it remains challenging to fabricate ultralong ZnO nanorods arrays in order to obtain a high aspect ratio by the conventional chemical bath deposition (CBD) or hydrothermal method. This problematic issue might be due to the decrease in the concentration of solution (source of ions) present in the bath during the growth process with an increase in duration of reaction and because of the thermal energy indirectly supplied to the substrate during heating of the solution [131]. Furthermore, it is not an easy task to increase the substrate temperature while not increasing the solution temperature. The solution would tend to boil at temperature more than 100°C, leading to an inhomogeneous growth and undesirable contamination on the substrate [131].

The emergence of DHS-MCBD in this work has been deemed to be able to address the aforementioned issues. The ZnO nanorods/p-GaN heterostructures could serve as a nano-sized junction device by improving the carrier injection efficiency at the heterojunction structure. In particular, this system provides a simple and low-cost method for the fabrication of a nano-size junction electronic device. The excellent UV and blue n-ZnO nanorods/p-GaN LED performance under reverse bias was fabricated with high intensity of electroluminescence (EL). The corresponding EL spectra obtained for the heterojunction NORLED (n-ZnO/p-GaN/sapphire) measured under reverse bias, ranging from 3 mA (-4.2 V) to 28 mA (-28.5 V) is shown in Fig. 6.21. It could be worth noting that the spectrum was composed of near UV emission centered at ~ 389 nm (3.18 eV) with a broadband centered at ~ 366 nm.

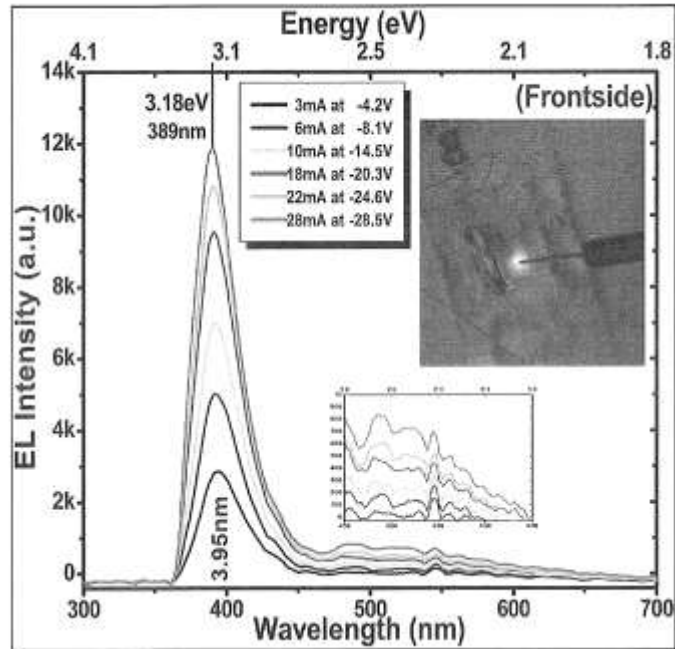


Fig. 6.21 EL spectra of heterojunction NORLED under reverse bias measured from frontside of n-ZnO/p-GaN/sapphire substrate LED [131].

In this work, dissimilar from previous studies, low temperature synthesis method, namely, microwave-induced combustion synthesis method (M.W) was used to prepare high purity, homogeneous, small particle sized phosphor powder for use to convert emission from GaN-based LEDs to white light. Fig. 6.22 depicts a schematic cross-section illustration and white light emission from the phosphor converted InGaN-based LED chip (445 nm).

Surface morphology of the obtained phosphor powder was observed by FESEM. As illustrated in Fig. 6.23 (a), highly agglomerated particles with coarsening surface area and cracks and pores formed by the escaping gases during the combustion reaction were obtained. This indicated that the sintering process had been locally completed. Furthermore, agglomerated particles are generally useful to the efficiency of LED- based lighting devices, which would prevent permeation blue light LED which affects on white light [132]. Fig. 6.23 (b) illustrates

the EL spectra of WLED fabricated using the phosphor converted InGaN-based LED chip (445 nm). A decrease in the blue LED peak intensity was observed while that of the yellow emission band increased.

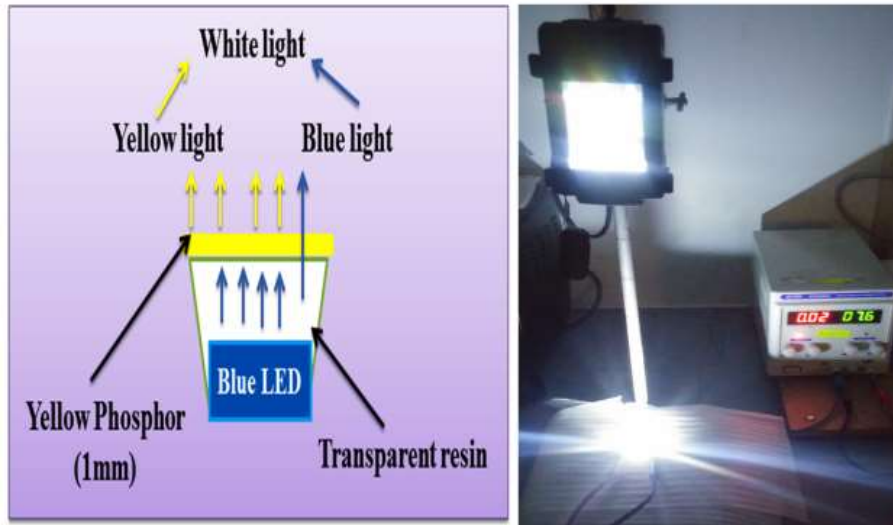
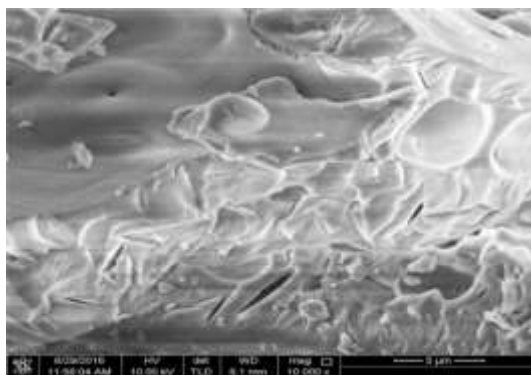
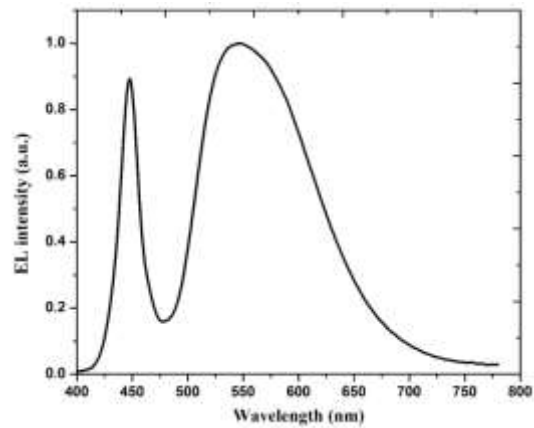


Fig. 6.22 Schematic cross-section illustration and image of the WLED device.



(a)



(b)

Fig. 6.23 (a) FESEM micrograph of YAG: Ce⁺³ phosphor powder sintering at 1050°C for 5 h and (b) EL spectra of phosphor converted InGaN-based WLED (445 nm).

This finding showed that more absorption of blue light has taken place and thus enhancing the yellow light output as well as reducing light scattering caused by the dense microstructure of the ceramic sample [133]. Nonetheless, the blue light emitted from the LED chip was not completely absorbed by the phosphor. This could be attributed to the non-uniform coverage of phosphor on the LED chip during manufacturing and low down conversion efficiency of the prepared phosphor. It is well-known that the down conversion efficiency strongly depends on the phosphor composition and phosphor grain size [134].

7. Theoretical Work

Alongside the experimental work, theoretical work has also been carried out. Simulation work proved that LED performance would reduce as the number of InGaN quantum well layer was increased [135]. The study was based on the integrated radiative recombination rate per sec per μm width (attributed as the emission efficiency) as a function of the number of InGaN quantum wells. Hence, the single quantum well (SQW) has exhibited a better performance than those of multi-quantum wells. Similar simulation results were reported by Chang *et al.* [136], Chang *et al.* [137] and Kuo *et al.* [138], where the performance of LEDs decreased with the increase of the number of quantum wells. In addition, energy band diagrams of simulated SQW and five quantum wells (5QWs) structures were also compared in the study. It was noted that the barrier heights (at p-GaN/active region interface at the valence band and active region/n-GaN interface at the conduction band) for 5QWs structure were relatively higher particularly at the active region/n-GaN interface as compared to that for single quantum well structure [135]. These would thus result in a difficulty in the transport of electrons and holes into the active region.

Fig. 7.1 depicts the performance characteristics of InGaN MQW laser structures [139-140]. The schematic diagram of deep violet $\text{In}_{0.082}\text{Ga}_{0.918}\text{N}/\text{GaN}$ double quantum well laser diode (DQW LD) structures under this study are shown in Fig. 7.1. The effects of Al composition and thickness of AlGaN electron blocking layer (EBL) on optical and electrical properties of deep violet $\text{In}_{0.082}\text{Ga}_{0.918}\text{N}/\text{GaN}$ DQW LDs have been investigated. In addition, a comparative study has been conducted on the performance characteristics of the LD structures with an AlGaN EBL and a quaternary AlInGaN EBL with an output emission wavelength at 390 nm.

Fig. 7.2 portrays optical intensity of the deep violet InGaN DQW LDs with different EBL structures, including the AlGaN EBL, quaternary AlInGaN EBL. It could be seen that the optical intensity was increased in the InGaN DQWLDs with quaternary AlInGaN EBL. The use of the quaternary AlInGaN EBL has enhanced radiative recombination in the well, as well as increasing output power and optical confinement factor (OCF) because of a greater carrier accumulation in the active region. The increase in the OCF and optical output power has thus resulted in an increase in the optical intensity. The simulation results showed that the use of quaternary AlInGaN EBL has also effectively improved the LD performance characteristics [144]. Fig. 7.2 (b) presents the electron current density of InGaN DQW LDs with AlGaN EBL and quaternary AlInGaN EBL. As shown in the figure, the electrons have contributed to the occurrence of radiative recombination in the wells and consequently lowering the over flow from the wells to the barriers and to the p-side layers.

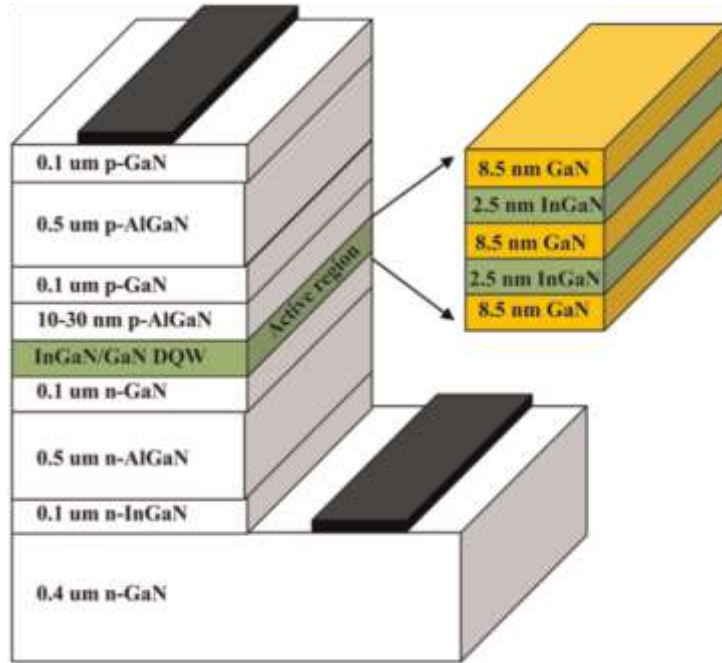


Fig. 7.1 Schematic diagram of laser structures of deep violet InGaN DQWLDs with AlGaN EBL [139].

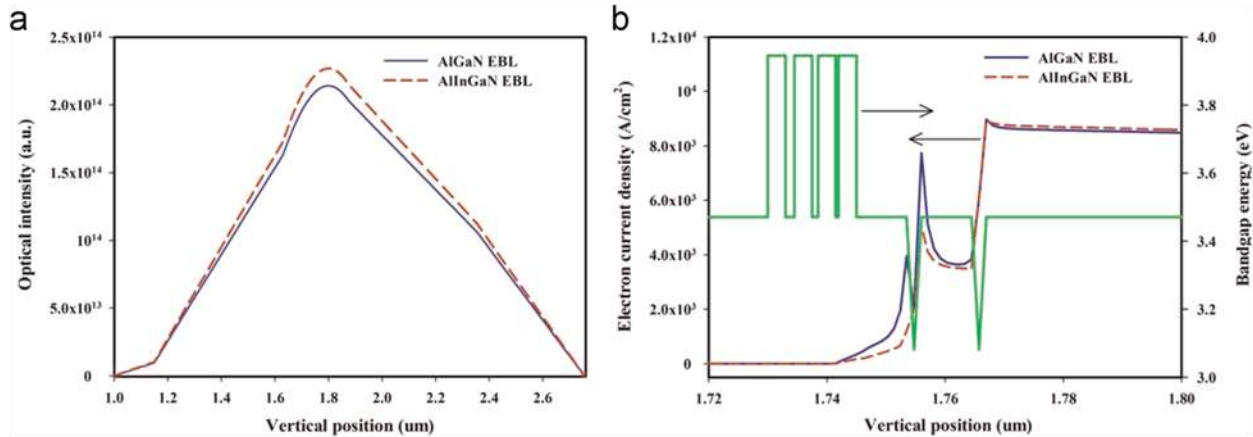


Fig. 7.2 (a) Optical intensity and (b) Electron current densities of deep violet $\text{In}_{0.082}\text{Ga}_{0.918}\text{N}/\text{GaN}$ DQW LDs with different EBL structures [139].

Besides that, the effects of inserting AlGaN EBL in the GaN-based VCSEL structures on the laser performance has been investigated using Integrated System Engineering Technical

Computer Aided Design (ISE TCAD) program software [141]. The performance characteristics of GaN-based quantum-well VCSEL were improved after the addition of AlGaN EBL. The effects of Al mole fraction (x) of the $\text{Al}_x\text{Ga}_{1-x}\text{N}$ EBL on the GaN-based VCSEL performance, ranging from $x = 0.15$ to $x = 0.25$ was also studied. As the mole fraction was increased from $x = 0.15$ to $x = 0.17$, the threshold current was reduced. This was due to the increase in carrier confinement due to an increase in the accumulation of carriers closer to the active region, accompanying the addition of $\text{Al}_x\text{Ga}_{1-x}\text{N}$ EBL. At mole fraction above $x = 0.17$, the threshold current was increased, attributable to a saturation of the carriers inside the active region, which has caused an increase in the leakage current. It could be also due to the obstruction created by the EBL towards the flow of holes into the active region. As the GaN-based VCSEL has demonstrated the optimum performance with $\text{Al}_{0.17}\text{Ga}_{0.83}\text{N}$ EBL, hence, the effects of $\text{Al}_{0.17}\text{Ga}_{0.83}\text{N}$ EBL thickness on the GaN-based quantum well VCSEL performance were also investigated. According to the simulation results, the GaN-based VCSEL established the optimum performance when the EBL thickness was 25 nm, as conveniently deduced in Fig. 7.3.

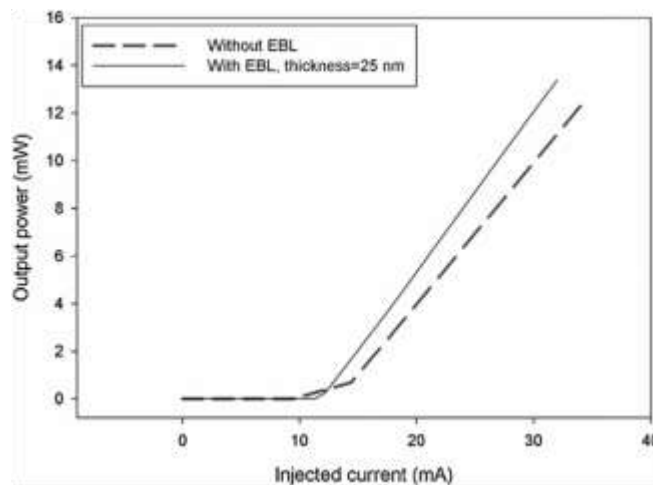


Fig. 7.3 Output power-injected current for InGaN-based intracavity-contacted oxide-confined VCSEL without EBL and VCSEL using 25 nm $\text{Al}_{0.17}\text{Ga}_{0.83}\text{N}$ EBL [141].

8. Summary

Intensive material studies and simulation work have been carried out on III-nitrides semiconductors (GaN and related alloys). Amorphous, microcrystalline, nanocrystalline, and epitaxial III-nitrides have been investigated for a wide variety of applications. Novel growth technology, processing techniques, treatments and optimization of device fabrication parameters have been carried out to enhance material quality and device performance. High quality III-nitrides thin films were successfully grown by plasma-assisted molecular beam epitaxy (PAMBE) on Si substrates. Light emitting diodes (LEDs), photodetectors (light sensors), metal-oxide-semiconductor (MOS) capacitors, pressure sensors, and gas sensors based on these materials have been fabricated and characterized. Alongside the experimental work, theoretical work has also been carried out to investigate the performance characteristics of GaN-based LEDs, multi-quantum well (MQW) laser structures, and vertical cavity surface emitting laser (VCSEL). Besides that, study on novel metallization schemes and transparent conducting oxides as electrodes for optoelectronic devices has also been carried out to enhance the performance of LEDs. Nanostructured porous GaN, ternary, and quaternary III-nitrides (InGaN and InAlGaN) with different mole fractions have been fabricated by three different techniques, namely, metal-assisted UV electroless etching, laser-induced etching, and DC as well as novel AC-assisted photo-electrochemical etching. Sensors fabricated from these films have shown significant improvement in device performance.

Low temperature microwave-assisted chemical bath deposition (MA-CBD) growth technique has been employed to grow ZnO/GaN heterojunction LED. Also, a novel and low cost "NORLED" (Nano-Rod LED) device, which emits in the UV region was fabricated using ultra long ZnO nanorods grown on the p-GaN substrate by a direct heat substrate-modified chemical bath deposition (DHS-MCBD) growth process. The DHS-MCBD method has turned out to be

promising for fabricating pn heterojunction nanorod devices. The UV emission is also expected to provide high energy to excite phosphor in order to produce white LEDs for solid state lighting (SSL) applications. SSL-LED industry is one of the most promising and upcoming market in the electronics industry. The lower power consumption fits well with the “green” energy which has been become the in-thing of today’s environmental matters. Future work will be focused on GaN-on-GaN technology and high brightness hybrid LEDs. New materials are crucial to driving down the price tag and driving up market acceptance. The prospects for III-nitrides are enormous, and these materials are expected to dominate the optoelectronics and electronics market in the years to come.

9. References

- [1] Wu, J., Walukiewicz, W., Yu, K. M., Ager, J. W., Haller, E. E., Lu, H., Schaff, W. J., Saito, Y., Nanishi, Y., Appl. Phys. Lett. 80, 3967 (2002)
- [2] Hai, L., Peter, S., Alexei, V., Jesse, T., Ahmed, E., J. Appl. Phys. 99, 114510 (2006)
- [3] Yoshida, S., Misawa, S., Gonda, S., Appl. Phys. Lett. 42, 427 (1983)
- [4] Amano, H. N., Sawaki, N., Akasaki, I., Toyoda, Y., Appl. Phys. Lett. 48,353 (1986)
- [5] Khan, M. A., Kuzhia, J. N., Bhattarai, A. R., Olsen, D. T., Appl. Phys. Lett. 62, 1786 (1993)
- [6] Nakamura, S., Senoh, M., Nagahama, S., Iwasa, N, Yamada, T., Matsushita, T., Kiyoku, H., Sugimoto, Y., Japanese J. Appl. Phys. 35, L74 (1995)
- [7] Metson, J. B., Ruck, B. J., Budde, F., Trodahl, H. J., Bittar, A., Prince, K. E., Appl. Surf. Sci. 244, 264 (2005)
- [8] Hariu, T., Usuba, T., Adachi, H., Shibata, Y., Appl. Phys. Lett. 32, 252 (1978)
- [9] Stumm, P., Drabold, D. A., Phys. Rev. Lett. 79, 677 (1997)
- [10] Yu, M., Drabold, D. A., Solid State Comm. 108, 413 (1998)
- [11] Kobayashi, S., Nonomura, S., Ohmori, T., Abe, K., Hirata, S., Uno, T., Gotoh, T., Nitta, S, Appl. Surf. Sci. 113/114, 480 (1997)
- [12] Hassan, Z., Lee, Y. C., Yam, F. K., Ibrahim, K., Kordesch, M. E., Halverson, W., Colter, P. C., Solid State Comm. 13, 283 (2005)
- [13] Hassan, Z., K, Ibrahim, Kordesh, M. E., Halverson, W., Colter., P. C., Intern. J. Modern Phys. B 16, 1086 (2002)
- [14] Ng, S. S., Hassan, Z., Hashim, M. R., Kordesch, M. E., Mater. Chem. Phys. 91, 404 (2005)
- [15] Ng, S. S., Hassan, Z., Hashim, M. R., Kordesch, M. E., Halverson, W., Colter, P. C., ICSE2002 Proc. p. 209 (2002)
- [16] Tauc, J., Amorphous and liquid semiconductors, Plenum Publishing Company Ltd.,1973, p. 159
- [17] Hassan, Z., Kordesch, M. E., Jadwisienzak, W. M., Lozykowski, H. J., Halverson, W., Colter, P. C., Mater. Res. Soc. Symp. Proc. 536, 245 (1999)
- [18] Chin, C. W., Hassan, Z., Yam, F. K., Ahmad, M. A., Thin Solid Films 544, 33 (2013)
- [19] Liu, L, Edgar, J. H., Mater. Sci. Eng. R37, 61(2002)
- [20] Roberts, J. C., Cook Jr., J. W., Rajagopal, P., Piner, E. L., Linthicum, K. J., Mater. Res. Soc. Symp. Proc. 1068, 1068-C06-0 (2008)
- [21] Chin, C. W., Yam, F. K., Beh, K. P., Hassan, Z., Ahmad, M. A., Yusof, Y., Mohd Bakhori, S. K., Thin Solid Films 520, 756 (2011)
- [22] Chuah, L. S., Hassan, Z., Ng, S. S., Abu Hassan, H., J. Mater. Res. 22, 2623 (2007)
- [23] Otto, A., in: B.O. Seraphin (Ed.), Optical Properties of Solids: New Developments, Norton-Holland, Amsterdam, 1976, p. 677
- [24] Ng, S. S., Hassan, Z., Abu Hassan, H., Solid State Comm. 145, 535 (2008)
- [25] Schubert, M., Tiwald, T. E., Herzinger, C. M. Phys. Rev. B. 61 (2000) 8187

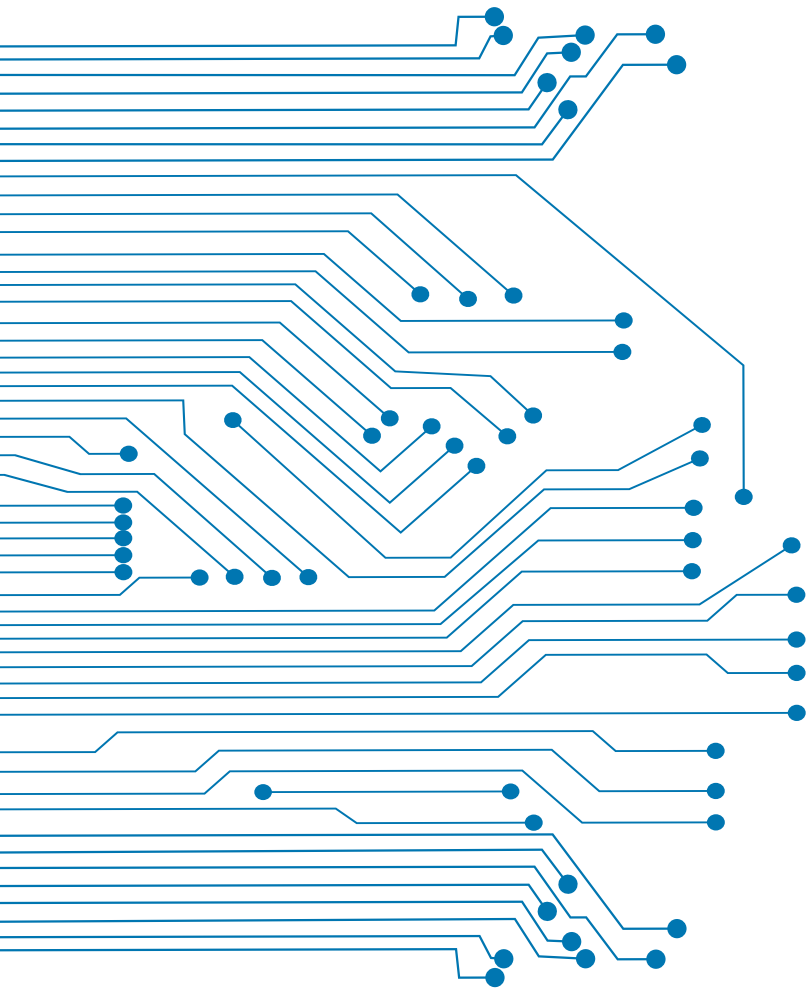
- [26] Nakamura, S., *IEEE J. Sel. Topics Quantum. Electron.* 3, 435 (1997)
- [27] Beh, K. P., Yam, F. K., Chin, C. W., Tneh, S. S., Hassan, Z., *J. Alloys Compd.* 506, 343 (2010)
- [28] Hussein, A. SH., Hassan, Z., Thahab, S. M., Abu Hassan, H., Abid, M. A., Chin, C. W., *Physica B: Condensed Matter* 406, 1267 (2011)
- [29] Hussein, A. SH., Thahab, S. M., Hassan, Z., Chin, C. W., Abu Hassan, H., Ng, S. S., *J. Alloys Compd.* 487, 24 (2009)
- [30] Hussein, A. SH., Ghazai, A. J., Salman, E. A., Hassan, Z., *Superlatt. Microstruc.* 63 141 (2013)
- [31] Hussein, A. S. H., Ghazai, A. J., Hassan, Z., *Optik - Intern. J. Light Electron Opt.* 124, 4257 (2013)
- [32] Hussein, A. SH., Hassan, Z., Thahab, S. M., Ng, S. S., Abu Hassan, H., Chin, C.W., *Appl. Surf. Sci.* 257, 4159 (2011)
- [33] Mohd Yusoff, M. Z., Hassan, Z., Abu Hassan, H., Abdullah, M. J., Rusop, M., Pakhuruddin, M. Z., *Mater. Sci. Semicond. Proc.* 34, 214 (2015)
- [34] Mohd Yusoff, M. Z., Baharin, A., Hassan, Z., Abu Hassan, H., Abdullah, M. J., *Superlatt. Microstruc.* 56, 35 (2013)
- [35] Hussein, A. Sh., Hassan, Z., Ng, S. S., Thahab, S. M., Chin, C. W., Abu Hassan, H., *Optoelectron. Adv. Mater. – Rapid Comm.* 4, 59 (2010)
- [36] Mohd Yusoff, M. Z., Hassan, Z., Chin, C. W., Abu Hassan, H. *Chin. J. Chem. Phys.* 23, 431 (2010)
- [37] Mohd Yusoff, M. Z., Hassan, Z., Ahmed, N. M., Abu Hassan, H., Abdullah, M. J., Rashid, M., *Mater. Sci. Semicond. Proc.* 16, 1859 (2013)
- [38] Abdullah, Q. N., Yam, F. K., Hassan, J. J., Chin, C. W., Hassan, Z., Bououdina, M., *Intern. J. Hydrogen Energy* 38, 14085 (2013)
- [39] Abdullah, Q. N., Yam, F. K., Hassan, Z., Bououdina, M., *J. Colloid Inter. Sci.* 460, 135 (2015)
- [40] Abdullah, Q. N., Yam, F. K., Hassan, Z., Bououdina, M., *Sens. Actuators B: Chem.* 204, 497 (2014)
- [41] Tan, L. K., Yam, F. K., Low, L. L., Beh, K. P., Hassan, Z., *Physica B: Condensed Matter* 434, 101 (2014)
- [42] Tan, L. K., Yam, F. K., Beh, K. P., Hassan, Z., *Superlatt. Microstruc.* 58, 38 (2013)
- [43] Abdullah, Q. N., Yam, F. K., Hassan, Z., Bououdina, M., *Superlatt. Microstruc.* 54, 215 (2013)
- [44] Muka`i, T., Yamada, M., Nakamura, S., *Japanese J. Appl. Phys.* 38, 3976 (1999)
- [45] Arakawa, Y., *IEEE Journal of Selected Topics in Quantum Electronics* 8, 823 (2002)
- [46] Kadir, A., Meissner, C., Schwaner, T., Pristovsek, M., Kneissl, M., *J. Cryst. Growth* 334, 40 (2011)
- [47] Ji, L. W., Su, Y. K., Chang, S. J., Wu, L. W., Fang, T. H., Chen, J. F., Tsai, T. Y., Xue, Q. K., Chen, S. C., *J. Cryst. Growth* 249, 144 (2003)
- [48] Butcher, K., Tansley, T., *Superlatt. Microstruc.* 38, 1 (2005)

- [49] Feng, Y., Aliberti, P., Veettil, B., Patterson, R., Shrestha, S., Green, M., *Appl. Phys. Lett.* 100, 053502 (2012)
- [50] Nguyen, H., Chang, Y., Shih, I., Mi, Z., *IEEE J Sel Top Quantum Electron.* 17,1062 (2011)
- [51] Lai, W.-J., Li, S.-S., Lin, C.-C., Kuo, C.-C., Chen, C.-W., Chen, K.-H., Chen, L.-C., *Scripta Materialia* 63, 653 (2010)
- [52] Miller, N., Ager, J., Smith, H., Mayer, M., Yu, K., Haller, E. E., Walukiewicz, W., Schaff, W. J., Gallinat, C., Koblmüller, G., Speck, J. S., *J. Appl. Phys.* 107,113712 (2010)
- [53] Chakraborty, P., Datta, G., Ghatak, K., *Physica B: Condensed Matter* 339, 198 (2003)
- [54] Davydov, V. Yu., Klochikhin, A. A., Emtsev, V. V., Kurdyukov, D. A., Ivanov, S. V., Vekshin, V. A., Bechstedt, F., Furthmüller, J., Aderhold, J., Graul, J., Mudryi, A.V., Harima, H., Hashimoto, A., Yamamoto, A., Haller, E. E., *Phys. Stat. Sol. B* 234, 787 (2002)
- [55] Butcher, K., Wintrebert-Fouquet, M., Chen, PPT., Tansley, T., Dou, H., Shrestha, S. K., Timmers, H., Kuball, M., Prince, K. E., Bradby, J. E., *J. Appl. Phys.* 95, 6124 (2004)
- [56] Amirhoseiny, M., Hassan, Z., Ng, S. S., Ahmad, M. A., *J. Nanomater.* 2011, Article ID 579427, 7 pages (2011)
- [57] Amirhoseiny, M., Hassan, Z., Ng, S. S., *Vacuum* 101, 217 (2014)
- [58] Amirhoseiny, M., Hassan, Z., Ng, S. S., Ahmad, M. A., *Adv. Mater. Res.* 545, 290 (2012)
- [59] Amirhoseiny, M., Hassan, Z., Ng, S. S., *Surf. Rev. Lett.* 20, 1350008 (2013)
- [60] Amirhoseiny, M., Hassan, Z., Ng, S. S., *Microelectron. Intern.* 30, 63 (2013)
- [61] Amirhoseiny, M., Hassan, Z., Ng, S. S., *Surf. Eng.* 29 (10), 772 (2013)
- [62] Amirhoseiny, M., Hassan, Z., Ng, S. S., *Intern. J. Modern Phys. B* 26, 1250137 (2012)
- [63] Alkis, S., Alevli, M., Burzhuev, S., Vural, H. A., Okyay, A. K., Ortac, B., *J Nanopart. Res.* 14, 1048 (2012)
- [64] Valdueza-Felip, S., Ibáñez, J., Monroy, E., González-Herráez, M., Artús, L., Naranjo, F.B., *Thin Solid Films* 520, 2805 (2012)
- [65] Murata, J., Sadakuni, S., *Electrochimica Acta* 171, 89 (2015)
- [66] Chen, D., Xiao, H.-D., Han, J., *J. Appl. Phys.* 112, 064303 (2012)
- [67] Cao, X. A., Cho, H., Pearton, S. J., Dang, G. T., Zhang, A. P., Ren, F., Shul, R. J., Zhang, L., Hickman, R., Hove, J. M. V., *Appl. Phys. Lett.* 75, 232 (1999)
- [68] Youtsey, C., Bulman, G., Adesida, I., *J. Electron. Mater.* 27, 282 (1998)
- [69] Geng, X., Duan, B. K., Grismer, D. A., Zhao, L., Bohn, P. W., *Semicond. Sci. Technol.* 28, 065001 (2013)
- [70] Díaz, D. J., Williamson, T. L., Adesida, I., Bohn, P. W., Molnar, R. J., *J. Appl. Phys.* 94, 7526 (2003)
- [71] Duan, B. K., Bohn, P. W., *Analyst* 135, 902 (2010)
- [72] Ramizy, A., Hassan, Z., Omar, K., *Mater. Lett.* 65, 61 (2011)
- [73] Mahmood. A., Hassan. Z., Yam. F. K., Chuah. L. S., *Optoelectron. Adv. Mater. – Rapid Comm.* 4, 1316 (2010)

- [74] Saleh H. Abud, Hassan. Z., Yam. F. K., *Int. J. Nanoelectron. Mater.* 8, 33 (2015)
- [75] Saleh H. Abud, Hassan. Z., Yam. F. K., *Mater. Chem. Phys.* 144, 86 (2014)
- [76] Saleh H. Abud, Hassan. Z., Yam. F. K., *Mater. Lett.* 107, 367 (2013)
- [77] Saleh H. Abud, Hassan. Z., Yam. F. K., Ghazai. A. J., *J. Solid State Chem.* 212, 242 (2014)
- [78] Lim, W. F., Quah, H. J., Hassan, Z., Radzali, R., Zainal, N., Yam, F. K., *J. Alloys Compd.* 649, 337 (2015)
- [79] Quah, H. J., Ahmed, N. M., Zainal, N., Yam, F. K., Hassan, Z., Lim, W. F., *Superlatt. Microstruc.* 95, 65 (2016)
- [80] Perumal, R., Hassan, Z. *Surf. Rev. Lett.* 23, 1550106-1 (2016)
- [81] Radzali, R., Hassan, Z., Zainal, N., Yam, F. K., *Microelectron. Eng.* 126, 107 (2014)
- [82] Radzali, R., Hassan, Z., Zainal, N., Yam, F. K., *Sens. Actuators B* 213, 276 (2015)
- [83] Yam, F. K., Hassan, Z., Ng, S. S., *Thin Solid Films* 515, 3469 (2007)
- [84] Cheah, S. F., Lee, S. C., Ng, S. S., Yam, F. K., Abu Hassan, H., Hassan, Z., *J. Luminescence* 159, 303 (2015)
- [85] Mahmood, A., Ahmed, N. M., Tiginyanu, I., Yusof, Y., Yam, F. K., Chuah, L. S., Hassan, Z., *J. Nanoelectron. Optoelectron.* 9, 287 (2014)
- [86] Mahmood, A., Ahmed, N. M., Tiginyanu, I., Yusof, Y., Yam, F. K., Chuah, L. S., Husnen, R. A., Hassan, Z., *Intern. J. Electrochem. Sci.* 8, 5801 (2013)
- [87] Quah, H. J., Ahmed, N. M., Hassan, Z., Lim, W. F., *J. Electrochem. Soc.* 163, H642 (2016)
- [88] Pophristic, M., Long, F. H., Schurman, M., Ramer, J., Ferguson, I. T. *Appl. Phys. Lett.* 74, 3519 (1999)
- [89] Wang, Y. D., Chua, S. J., Sander, M. S., Chen, P., Tripathy, S., Fonstad, C. G., *Appl. Phys. Lett.* 85, 816 (2004)
- [90] Al-Heuseen, K., Hashim, M. R., Ali, N. K., *Appl. Surf. Sci.* 257, 6197 (2011)
- [91] Vajpeyi, A., Tripathy, S., Chua, S., Fitzgerald, E., *Physica E* 28, 141 (2005)
- [92] Radzali, R., Hassan, Z., Zainal, N., Yam, F. K., *J. Alloys Compd.* 622, 565 (2015)
- [93] Quah, H. J., Lim, W. F., Hassan, Z., Yam, F. K., Zainal, N., *J. Alloys Compd.* 662, 32 (2016)
- [94] Wu, X. L., Siu, G. G., Yuan, X. Y., Li, N. S., Gu, Y., Bao, X. M., Jiang, S. S., Feng, D., *Appl. Phys. Lett.* 73, 1568 (1998)
- [95] Hassan, Z., Lee, Y. C., Yam, F. K., Abdullah, M. J., Ibrahim, K., Kordesch, M. E., *Mater. Chem. Phys.* 84, 369 (2004).
- [96] Abdullah, K. A., Abdullah, M. J., Yam, F. K., Hassan, Z., *Microelectron. Eng.* 81, 201 (2005)
- [97] Lee, Y. C., Hassan, Z., Yam, F. K., Abdullah, M. J., Ibrahim, K., Barmawi, M., Sugiato, Budiman, M., Arifin, P., *Appl. Surf. Sci.* 249, 91 (2005)
- [98] Michael, P., *Noncrystalline Semiconductors*, vol. 1, CRC Press, Inc., Boca Raton, FL, 1987, pp. 46.

- [99] Fritzsche, H., in: J. Tauc (Ed.), *Amorphous and Liquid Semiconductors*, Plenum Press, London, 1974, p. 253.
- [100] Rhoderick, E. H., Williams, R. H., *Metal–Semiconductor Contact*, 2nd ed. Oxford University Press, New York, 1998, pp. 230.
- [101] Schmitz, A. C., Ping, A. T., Asif Khan, M., Chen, Q., Yang, J. W., Adesida, I., *Semicond. Sci. Technol.* 11, 1464 (1996)
- [102] Hassan, Z., Kordesch, M. E., *Solid-State Sci. Technol.* 8, 100 (2000)
- [103] Guo, J. D., Pan, F. M., Feng, M. S., Guo, R. J., Chou, P. F., Chang, C. Y., *J. Appl. Phys.* 80, 1623 (1996)
- [104] Pearnton, S. J., Zolper, J. C., Shui, R. J., Ren, F., *J. Appl. Phys.* 86, 1 (1999)
- [105] Saleh, H. A., Hassan, Z., Yam, F. K., Chin, C. W., *Measurement* 50, 172 (2014)
- [106] Ghazai, A. J., Aziz, W. J., Abu Hassan, H., Hassan, Z., *Superlatt. Microstruc.* 51, 480 (2012)
- [107] Chiu, S.-Y., Huang, H.-W., Huang, T.-H., Liang, K.-C., Liu, K.-P., Tsai, J.-H., Lour, W.-S., *Int. J. Hydrogen Energy* 34, 5604 (2009)
- [108] Buttner, W. J., Matthew, B. P., Burgess, R., Rivkin, C. *Int. J. Hydrogen Energy* 36, 2462 (2011)
- [109] Baboian, R., *Corrosion Tests and Standards* 559 (1996)
- [110] Zhao, G. Y., Sutton, W., Pavlidis, D., Piner, E. L., Schwank, J., Hubbard, S., *IEICE Trans. Electron.* E86–C, 2027 (2003)
- [111] Chin, C. W., Hassan, Z., Yam, F. K., *J. Nonlinear Opt. Phys. Mater.* 17, 435 (2008)
- [112] Ramizy, A., Hassan, Z., Omar, K., *Sens. Actuators B: Chem.* 155, 699 (2011)
- [113] Abdulgafour, H. I., Hassan, Z., Yam, F. K., Chin, C. W., *Thin Solid Films* 540, 212 (2013)
- [114] Hassan, Z., Lee, Y. C., Ng, S. S., Yam, F. K., Liu, Y., Rang, Z., Kauser, M. Z., Ruden, P. P., Nathan, M. I., *Phys. Stat. Sol. (c)* 3, 2287 (2006)
- [115] Ali, A. H., Abu Bakar, A. S., Egawa, T., Hassan, Z. *Superlatt. Microstruc.* 60, 201 (2013)
- [116] Adivarahan, V., Lunev, A., Asif Khan, M., Yang, J., Simin, G., Shur, M. S., Gaska, R. *Appl. Phys. Lett.* 78, 2781 (2001)
- [117] Shen, T. C., Gao, G. B., Morkoc, H., *J. Vac Sci. Technol. B* 10, 2113 (1992)
- [118] Steigerwald, D. A., Bhat, J. C., Collins, D., Fletcher, R. M., Holcomb, M. O., Ludowise, M. J., Martin, P. S., Rudaz, S. L., *IEEE J. Select. Topics Quantum Electron.* 8, 310 (2002)
- [119] Hassan, Z., Lee, Y. C., Yam, F. K., Yap, Z. J., Zainal, N., Abu Hassan, H., Ibrahim, K. *Phys. Stat. Sol. (C)* 1, 2528 (2004)
- [120] Ali, A. H., Abu Bakar, A. S., Ahmad, M. A., *Adv. Mater. Res.* 1024, 75 (2014)
- [121] Ali, A. H., Abu Bakar, A. S., Hassan, Z. *Appl. Surf. Sci.* 288, 599 (2014)
- [122] Zhang, W., Zhu, G.-S., Zhi, L., Yang, H.-J., Yang, Z.-P., Yu, A.-B., Xu, H.-R. *Vacuum* 86, 1045 (2012)
- [123] Schlaf, R., Murata, H., Kafafi, Z. H. *J. Electron Spectroscopy and Related Phenomena* 120, 149 (2001)

- [124] Meng, L.-J., Santos, M. P. D., *Thin Solid Films* 322, 56 (1998)
- [125] Wan, N., Wang, T., Sun, H., Chen, G., Geng, L., Gan, X., Guo, S., Xu, J., Xu, L., Chen, K., *J. Non-Cryst. Solids* 356, 911 (2010)
- [126] Zhu, F., Huan, C. H. A., Zhang, K., Wee, A. T. S., *Thin Solid Films* 359, 244 (2000)
- [127] Adurodija, F. O., Izumi, H., Ishihara, T., Yoshioka, H., Matsui, H., Motoyama, M., *Vacuum* 59, 641 (2000)
- [128] Nam, E., Kang, Y. -H., Son, D. -J., Jung, D., Hong, S. -J., Kim, Y. S., *Surf. Coat. Technol.* 205, S129 (2010)
- [129] Gupta, N., Sasikala, S., Mahadik, D. B., Rao, A. V., Barshilia, H. C., *Appl. Surf. Sci.* 258, 9723 (2012)
- [130] Hassan, J. J., Mahdi, M. A., Yusof, Y., Abu Hassan, H., Hassan, Z., Al-Attar, H. A., Monkman, A.P., *Opt. Mater.* 35, 1035 (2013)
- [131] Hassan, Z., Ahmed, N. M., Sabah, M. Direct Heat Substrate-Modified Chemical Bath Deposition System for Growth of Ultra Long Zinc Oxide (ZnO) Nanorods and Process for Fabrication of a Nano-Size Junction LED, patent filed (2016)
- [132] Huang, S. C., Wu, J.K., Hsu, W. J., *Intern. J. Appl. Ceram. Technol.* 6, 465 (2009)
- [133] Wei, N. A., Lu, T. C., Li, F., Zhang, W., Ma, B. Y., Lu, Z. W., Qi, J. Q., *Appl. Phys. Lett.* 101, 061902 (2012)
- [134] Sheu, J.-K., Chang, S.-J. Kuo, C. H., Su, Y.-K., Wu, L. W., Lin, Y. C., Lai, W. C., Tsai, J. M., Chi, G.-C., Wu, R. K., *IEEE Photonics Technol. Lett.* 15, 18 (2003)
- [135] Zainal, N., Hassan, Z., Abu Hassan, H., Hashim, M. R., *Optoelectron. Adv. Mater. - Rapid Comm.* 1, 404 (2007)
- [136] Chang, J.-Y., Kuo, Y.-K., *Proc. SPIE* 4913, 115 (2002)
- [137] Chang, J.-Y., Kuo, Y.-K., *J. Appl. Phys.* 93, 4992 (2003)
- [138] Kuo, Y.-K., Yi-An Chang, *IEEE Journal Quantum Electronics* 40, 437 (2004)
- [139] Alahyarizadeh, Gh., Amirhoseiny, M., Hassan, Z., *Opt. Laser Technol.* 76, 106 (2016)
- [140] Alahyarizadeh, Gh., Hassan, Z., Thahab, S. M., Yam, F. K., *Optik - Intern. J. Light Electron Opt.* 125, 4911 (2014)
- [141] Goharrizi, A. Z., Alahyarizadeh, Gh., Hassan, Z., Ghazai, A. J., Abu Hassan, H., *Optik - Intern. J. Light Electron Opt.* 126, 1377 (2015)



Academy of Sciences Malaysia
Level 20, West Wing, Matrade Tower,
Jalan Sultan Ismail Haji Ahmad Shah,
off Jalan Tuanku Abdul Halim,
50480 Kuala Lumpur, Malaysia

Phone : +6 (03) 6203 0633
Fax : +6 (03) 6203 0634

